

The Application of Laser Diagnostics
to the Measurement of Concentration and Temperature
in Practical Methane-Air Flames

by
Quang-Viet Nguyen

M.S. (University of California at Irvine) 1990

B.S. (University of California at Irvine) 1989

A dissertation submitted in partial satisfaction of the
requirements for the degree of
Doctor of Philosophy
in
Engineering – Mechanical Engineering
in the
GRADUATE DIVISION
of the
UNIVERSITY of CALIFORNIA at BERKELEY

Committee in charge:

Professor Robert W. Dibble, Chair

Professor J. Y. Chen, Co-Chair

Professor Daniel M. Neumark

1995

The dissertation of Quang-Viet Nguyen is approved:

Chair

Date

Co-Chair

Date

Date

University of California at Berkeley

1995

This dissertation is dedicated to my best friend, Vananh.

Contents

Title Page	i
Approval Page	ii
Dedication	iii
Contents	iv
List of Figures	vii
List of Tables	x
Acknowledgments	xi
Chapter 1: Scope of Thesis	1
1.1 Motivation	1
1.2 Organization of Chapters	2
Chapter 2: Tomographic Measurements of Carbon Monoxide	5
Temperature and Concentration in Bunsen Flames	
Using Diode Laser Absorption	
2.0 Chapter Overview	5
2.1 Introduction	7
2.2 Theory	9
2.3 Experimental	16
2.4 Results	26

Chapter 3:	An Experimental and Numerical Comparison of Extractive and In-Situ Laser Measurements of Non-Equilibrium Carbon Monoxide in Lean-Premixed Natural Gas Combustion	36
3.0	Chapter Overview	36
3.1	Introduction	37
3.2	Experimental Apparatus	40
3.3	Modeling of Chemical Kinetics	49
3.4	Results	51
3.5	Conclusions	57
Chapter 4:	Laser Measurements of Temperature, The Major Species, OH and NO in a Methane-Air Bunsen Flame	58
4.0	Chapter Overview	58
4.1	Introduction	60
4.2	Experimental Approach and Apparatus	63
4.3	Results	77
4.4	Conclusions	88
Chapter 5:	Two-Photon Laser Induced Fluorescence Measurements of CO in Bunsen Flames	90
5.0	Chapter Overview	90
5.1	Introduction	91
5.2	Experimental Approach	93

5.3 Experimental	99
5.4 Results	101
5.5 Conclusions	104
References	106
Appendix A: CO Linestrength and Position, Voigt and Galatry Profile Codes	116
Appendix B: Tomographic Reconstruction Codes	125
Appendix C: Modulation Spectroscopy Simulation Codes, Non-Linear Least Squares 2f Spectrum Fitting Code	132
Appendix D: Raman Data Reduction Procedure	142
Appendix E: OH and NO LIF Data Reduction Codes	147
Appendix F: High Resolution Oxygen Absorption Spectrum Obtained Using and External-Cavity Continuously Tunable Diode Laser	172
Last Page	179

List of Figures

Figure 2.1: The projection of $P(r, \theta)$ of a property field $F(x, y)$ along ds at angle θ .	14
Figure 2.2: Schematic of optical layout for direct absorption measurements	17
Figure 2.3: Schematic of the electronics and instrumentation.	19
Figure 2.4: Schematic of the Bunsen burner, the laser measurement zone and the associated flow system.	22
Figure 2.5: Comparison of line-center, measured pathlength integrated transmission data with CT reconstructed backprojections for the P(20) and P(27) transitions.	27
Figure 2.6: Reconstructed temperature (curve with triangles) and concentration (curve with circles) profiles.	29
Figure 2.7: The $2f$ spectrum of the P(38) ($v = 1 \leftarrow 0$) transition of the hot combustion gases above a methane-air flat-flame operating at an equivalence ratio of $\phi = 0.85$ (solid curve) showing the spectral shift.	31
Figure 2.8: The spectral shift of the P(38) ($v = 1 \leftarrow 0$) transition as a function of equivalence ratio for a methane-air flat-flame burner.	32
Figure 2.9: The spectral shift of the P(38) CO transition as a function of perturbers CO and H ₂ .	35
Figure 3.1: Schematic of the LPC reactor and probe sampling system.	40
Figure 3.2: Schematic of the optical arrangement of the TDL absorption spectroscopy system.	43
Figure 3.3: Comparison of TDL and probe measured CO values with model and equilibrium predicted values for the 5 cm PFR with an approximate residence time of 2 ms.	50
Figure 3.4: Comparison of TDL and probe measured CO values	52

with model and equilibrium predicted values for the 15 cm PFR with an approximate residence time of 6 ms.

Figure 3.5: Comparison of TDL and probe measured CO values with model and equilibrium predicted values for the 45 cm PFR with an approximate residence time of 20 ms.	53
Figure 3.6: The temperature profiles used to model the reactor and sampling probes as a PFR for the equivalence ratio of 0.85.	55
Figure 3.7: The probe sampling error defined as $[\text{CO}]_{\text{act}}/[\text{CO}]_{\text{probe}}$ as a function of inlet gas temperature calculated using the PFR model with the temperature profile shown in Fig. 3.6.	56
Figure 4.1: Schematic of Bunsen burner. The coflow air is homogenized by glass beads prior to entering the honeycomb flow straightener. The measurement planes for the radial traverses of flame A are shown.	65
Figure 4.2: Schematic of the Raman-Rayleigh-LIF apparatus.	68
Figure 4.3: Comparison of Raman-Rayleigh-LIF measurements (data points) with adiabatic equilibrium calculations (lines) for methane-air calibration flames.	76
Figure 4.4: Radial profiles for flame A at the Z_1 axial location (see Fig. 4.1).	78
Figure 4.5: Radial profiles for flame A at the Z_2 axial location, approximately 10 mm above the inner flame cone tip.	81
Figure 4.6: Radial profiles for flame A at the Z_3 axial location, approximately 20 mm below the outer visible flame tip.	83
Figure 4.7: Axial profiles along the centerline of flame A. NO measurements using a quartz suction probe and chemiluminescent NO_x analyzer are also shown for comparison.	85
Figure 4.8: Axial profiles along the centerline of flame B.	86
Figure 4.9: Axial profiles along the centerline of flame C.	87

Figure 5.1: Schematic of electronic states of CO showing the different energy transfer paths.	94
Figure 5.2: Excitation scans of the <i>B-X</i> band at ambient and flame temperatures. The fluorescence from the <i>B-A</i> (0,1) band at 483.5-nm is plotted versus the laser excitation wavelength .	97
Figure 5.3: Linearity test of the CO TPLIF signal for cold CO and CO at flame temperatures.	100
Figure 5.4: Radial profile of Bunsen flame B (see Table 4.1) at an axial location of 21 mm.	103

List of Tables

Table 2.1: Burner operating conditions.	21
Table 4.1: Premixed methane-air Bunsen flame operating conditions.	67
Table D.1: Raman calibration constants (k_{ij}).	144

Acknowledgments

Throughout my four years at Berkeley, Professor Robert Dibble has been my inspiration to academic, and sometimes non-academic endeavours. Besides his tremendous built in cache of numerous anecdotes (all of which are funny most of the time), I would like to thank him for his remarkable experimental insight which has saved my hide on numerous occasions, and his ability to light fires, both literally and figuratively. Most of all I want to thank him for being both an advisor and a friend.

I thank Professor J.Y. Chen, for giving me the knowledge and tools which permitted me to truly appreciate the power of CHEMKIN modeling. I would also like to thank him for his encouragement and laboratory equipment ‘gifts’, many of which permitted the experiments described herein to proceed without delay. Finally, I also would like to thank him for being my qualifying exam committee chair and thesis committee co-chair.

I thank Professor Daniel Neumark, who I credit for providing me the knowledge and understanding of laser spectroscopy that has been essential to the research described in this thesis. I would also like to thank him for being on my thesis and qualifying exam committee.

I would like to thank Dr. Anil Gulati of General Electric R&D, who provided the motivation, assistance, materials and funding which made Chapters 2 and 3 a reality.

I thank Dr. Robert Barlow for providing me the unique opportunity to use his laboratory during my two-month visit to Sandia National Laboratories which provided the invaluable data which made Chapters 4 and 5 possible. I thank him mostly for showing me how a careful and thoughtful experiment is really done. During my stay at Sandia, Dr. Cambell Carter and Dr. Greg

Fiechtner were instrumental to the success of the experiments. I would especially like to thank Dr. Carter for his constructive comments on the drafts of Chapter 4.

I thank the following friends and colleagues for both their assistance with the experiments and for making my experience at Berkeley a whole lot of fun: Mr. Bradley Edgar, Dr. Lance Smith, Mr. Marc Rumminger, Ms. Tami Bond, Mr. Jeff Muss, Mr. Brian Higgins, Dr. Stefan Kampmann, Mr. Daniel Hoffman, and Dr. Timothy Day of New Focus, Inc.

Finally, I would like to thank my parents for their encouragement and guidance over the past 26 years.

The research described in this thesis was supported in part by: The California Institute for Energy Efficiency, General Electric Corporate Research and Development, and The United States Department of Energy, Office of Basic Energy Sciences, Division of Chemical Sciences.

Chapter 1

Scope of Thesis

1.1 Motivation

The majority of natural gas, composed primarily of methane (CH_4), is consumed by practical devices that include: Bunsen burners (used for industrial process heating and residential use), and lean-premixed combustors (used for utility power generation and gas turbines). The accurate numerical modeling of these practical combustion devices frequently requires the non-intrusive measurements of various species and temperatures in flames for comparison and validation. The measurement of carbon monoxide (CO) and nitric oxide (NO), however, is at the forefront of interest due to their nature as regulated pollutants.

Thus, the concentration and temperature of various species (CO, NO, OH, H_2 , CO_2 , H_2O , O_2 , N_2 , CH_4) as they exist in Bunsen flames and lean-premixed combustors burning mixtures of CH_4 and natural gas with air were measured using the following non-intrusive techniques: line-of-sight (l-o-s) diode laser absorption, laser Raman and Rayleigh scattering, and laser induced fluorescence (LIF).

1.2 Organization of Chapters

Each of the following chapters describes a different experiment, with the common thread being the application of laser diagnostics to the measurement of species concentration and temperature in methane-air flames. The chapters were originally written as individual papers, and appear essentially in chronological order, but each chapter is self-sufficient and can be read out of order. Due to their self-sufficient nature, some of material in each chapter is repeated.

Chapter 2 examines the diode laser direct absorption technique used in conjunction with a computer tomographic (CT) reconstruction method to yield spatially resolved measurements of CO in Bunsen flames. The direct absorption technique permitted detection sensitivities of percent mole fraction levels over pathlengths of several mm. In an attempt to increase detection sensitivity, modulation techniques were employed to measure high rotational level CO transitions ($J=38$) which are populated only at high temperatures. High resolution absorption measurements of the P(38) transition revealed that spectral shifts on the order of $+0.009\text{ cm}^{-1}$ (line-center) exist and are a function of the flame equivalence ratio.

Chapter 3 describes the measurement of sub-percent levels of CO at the exit of a lean-premixed natural gas combustor using modulation techniques in conjunction with I-O-S absorption. The use of modulation spectroscopy permitted detection sensitivities of 40 ppm of CO at flame temperatures over a pathlength of 4 cm. The diode laser absorption measurements were compared to: (1) measurements obtained using extractive probe sampling, and (2) with the results of a numerical chemical kinetic model of the combustion process. These comparisons revealed that the use of extractive probes to measure part-per-million levels of CO at temperatures above 1000 K can give values of CO concentration that are less the true amount by

up to a factor of 10. Without success, several designs of so-called aerodynamic quench probes were investigated to determine if probe sampling of hot CO was possible.

Chapter 4 examines the application of simultaneous Laser Raman-Rayleigh scattering and LIF to measure the major species, temperature, and OH and NO in a CH₄-air Bunsen flame with spatial resolution. The Raman measurements provide the simultaneous measurement of all the major species at percent mole fraction detection sensitivities. LIF was employed for its high detection sensitivity; the minimum detectable amounts of NO were about 4 ppm at flame temperatures. In addition to providing a detailed mapping of Bunsen flames for comparisons with numerical models, the measurements revealed that the majority of NO (about 80 ppm) formed along the centerline of the Bunsen flame resulted from the prompt mechanism. The amount of NO formed was also found to decrease with increasing equivalence ratios. We also find that as the equivalence ratio of a Bunsen flame is increased, the length of the unburnt fuel-air core region also increases; this also increases the amount of convective and radiative preheating that the unburnt fuel-air mixture experiences as it travels up the core region. Consequently, the peak flame temperatures (about 2000 K) along the centerline of a Bunsen flame were found to be insensitive to changes in the equivalence ratio. Thus a simple reduction in the amount of premixed air in Bunsen flames (increasing the equivalence ratio) can significantly reduce the peak levels of NO along the flame centerline without sacrificing efficiency.

Chapter 5 describes a study of the two-photon LIF (TPLIF) technique as applied to CO. TPLIF is an inherently nonlinear diagnostic technique, thus simultaneous Raman and Rayleigh measurements were used to access the extent of the nonlinear nature of the TPLIF technique. We

found that using high laser irradiances permitted TPLIF to behave *linearly* with laser power. We attribute the linear behavior to the increased rates of photo-ionization that occur at high laser irradiances. An additional benefit of the photo-ionization is the insensitivity of the CO TPLIF signal to collisional electronic quenching, this is very advantageous for quantitative measurements. However, the high rates of photo-ionization also reduce the detection sensitivity relative to single-photon LIF techniques as applied to NO, for example. We obtained single-shot detection sensitivities of about 0.1% mole fraction at flame temperatures.

Chapter 2

Tomographic Measurements of Carbon Monoxide

Temperature and Concentration In a Bunsen Flame

Using Diode Laser Absorption

2.0 Chapter Overview

The temperature and concentration profiles of carbon monoxide (CO) in a laminar, axisymmetric, premixed methane-air Bunsen flame are measured using line-of-sight diode laser absorption spectroscopy conjunction with computer tomographic (CT) reconstruction. The absorption spectra for the P(20) ($\nu = 2 \leftarrow 1$) and P(27) ($\nu = 1 \leftarrow 0$) rovibrational transitions of CO were measured at 21 evenly spaced positions over a 1.33 cm span for a 1.3 cm radius flame. The CT reconstruction algorithm was based on the Fourier convolution technique. The tomographically reconstructed normalized transmission profiles derived from the absorption spectra, in conjunction with a quantum mechanical model for the rovibrational behavior of CO,

yielded both the temperature and concentration profiles. The Bunsen flame has 3 distinct zones: (1) an inner rich-premixed flame zone, (2) an outer non-premixed flame zone and (3) an unburnt core region. The reconstructed temperature profile showed that the core region temperature was close to ambient and rapidly increased to the adiabatic flame temperature in the inner flame zone. The temperature was then observed to reach a local minima of approximately 200 K less than the adiabatic flame temperature. At the outer flame zone, the temperature again increased to the adiabatic flame temperature. The reconstructed concentration profile was reasonable, low in the core region, with a maximum at the approximate location of the inner flame zone and subsequently decreased to a low level towards the outer flame zone where the CO concentration goes towards zero as expected for a non-premixed flame zone. The determination of absolute concentrations using tomographic techniques has the advantage of not requiring the knowledge of the actual pathlength through the probed flame, an important consideration for flames in free-space.

In an attempt to measure the low concentrations of CO at the edges of the Bunsen flame, we switched from direct absorption to a wavelength modulation technique. With this improved sensitivity, we have discovered a large spectral shift of the CO P(38) ($\nu = 1 \leftarrow 0$) transition depending on whether the post-flame combustion products were fuel-lean (blue shift $+0.009 \text{ cm}^{-1}$), or fuel-rich (no shift).

2.1 Introduction

2.1.1 Motivation

The role of carbon monoxide (CO) as a primary combustion intermediate in hydrocarbon fuels has generated considerable research efforts towards the measurement and modeling of CO in a wide array of practical combustion systems. The measurement of CO in flames using laser-spectroscopic methods is attractive due to the relatively strong transition dipole moment and well understood quantum mechanical behavior of CO. Previous work using diode laser absorption spectroscopy to measure CO in flames include Varghese and Hanson (1980, 1981), Schoenung and Hanson (1981) and Miller *et al.* (1991). These earlier studies of CO have primarily addressed the measurement of the spectroscopic parameters of CO in a flat flame (where spatial resolution was not a major requirement) or have verified the accuracy of the measurements using tunable diode lasers with other techniques such as extractive probe sampling. The field of computer tomography (CT) has also been extensively researched and is a relatively mature technology. Previous work on computer tomography in combustion include: Emmermann *et al.* (1980), Santorro *et al.* (1980), Hughey and Santavicca (1982), Beiting (1990), and Dasch (1992). Much of the work on tomography focused on the numerical algorithm aspects of tomography or on the proof of principle measurements of non-combustion related species.

The present paper combines the two relatively mature technologies of diode laser spectroscopy and computer tomography. We present the simultaneous measurement of the concentration and temperature profiles of CO in an axisymmetric, laminar, premixed methane-air Bunsen flame using diode laser absorption spectroscopy of multiple transitions in conjunction with tomographic reconstruction techniques. An axisymmetric, laminar, methane-air flame was chosen to simplify both the tomographic reconstruction process and the boundary conditions for

the verification of numerical simulations of a steady, two-dimensional laminar flames with finite rate chemistry currently in use (Smooke, 1992).

2.1.2 Interest in CO

In addition to the interest in CO as a primary combustion intermediate, increasing concerns of CO as a pollutant have also been voiced due to the increasing demand for low NO_x combustion. Low NO_x combustion, with few exceptions, relies on reducing the temperature of combustion to prevent the formation of thermal NO_x. This low temperature is achieved either by diluting and quenching the combustion gases with cool air or by inserting a radiative body or matrix-insert into the flame zone. The reduction of NO_x by decreasing the combustion temperature is often accompanied by an increase in CO concentration. Thus, the ability to measure the distribution of CO generated by low NO_x combustion is of interest. Advances in non-linear optical diagnostic techniques such as degenerate four wave mixing (DFWM) have demonstrated the ability to measure CO in flames (Rakestraw *et al.*, 1991). The application of DFWM would be enhanced by a calibration source to quantify the nature of a signal from a non-linear process. The development of such advanced techniques would be aided by a reliable and quantitative line-of-sight diode laser measurement of CO in a flame.

2.2 Theory

2.2.1 Absorption spectroscopy

The absorption of a light source of frequency ν and intensity $I_0(\nu)$ by an absorbing medium with an absorption coefficient α is given by the Lambert-Beer law:

$$\ln \frac{I(\nu)}{I_0(\nu)} = - \int_0^L \alpha dl , \quad (2.1)$$

where $I(\nu)$ is the transmitted intensity, dl is the infinitesimal pathlength of absorption and L is the pathlength of absorption. To relate this equation to quantitative values, we define α by

$$\alpha = S_0 S(T, V, J, Br) G(T, P_{TOT}, \nu, J, Br) P_{CO} , \quad (2.2)$$

where S_0 is the fundamental bandstrength of absorption which is a function of the transition dipole moment for CO and has units of $[\text{cm}^{-2} \text{ atm}^{-1}]$. $S(T, V, J, Br)$ is the fractional linestrength of the fundamental bandstrength and is a function of the temperature T , the initial vibrational level V , the initial rotational level J and the rotational branch of transition Br (either a P or R for CO). $G(T, \nu, J, Br)$ is the lineshape function, and P_{CO} is the partial pressure of CO in atm. $S(T, V, J, Br)$ is calculated using the partition functions for a diatomic molecule with anharmonicity, centrifugal distortion and vibration-rotation coupling included. Details of these calculations can be found in Varghese and Hanson (1980) and their implementations in FORTRAN are in Appendix A.

2.2.2 Calculation of the lineshape function

The lineshape function $G(T, \nu, J, Br)$, strictly speaking is also a function of the collisional partners. For the conditions encountered in an atmospheric flame where collisional and Doppler broadening are important, a Voigt profile is assumed for the lineshape function. For the purposes of simplifying the calculations, we will assume $G(T, \nu, J, Br)$ to be the Voigt profile calculated using an average collisional width $\Delta\nu_C$ based on the collisional widths of CO in a methane-air

flame measured by Varghese and Hanson (1981). Varghese and Hanson (1981), report the collisional width $\Delta\nu_C$ to vary linearly with the rotational quantum number and to vary with $T^{-1/2}$ at the high temperatures encountered in a flame. The Voigt function is given by

$$V(x, a) = \frac{a}{\pi} \int_{-\infty}^{\infty} \frac{e^{-y^2} dy}{a^2 + (x - y)^2} , \quad (2.3)$$

where $x = 2\sqrt{\ln 2}(\nu - \nu_0) / \Delta\nu_D(T)$, ν_0 is the line center frequency of absorption, and a is the Voigt parameter defined by

$$a(T, P_{TOT}, Q, \nu) = \frac{\sqrt{\ln 2} \Delta\nu_C(T, P_{TOT}, Q)}{\Delta\nu_D(T)} . \quad (2.4)$$

$\Delta\nu_D(T)$ is the Doppler width which is equal to $7.162 \times 10^{-7} \nu_0 \sqrt{T / MW}$, where MW is the molecular weight of the molecule, Q represents the quantum mechanical parameters V, J and Br . The Voigt function $V(x, a(T, Q))$ can be readily computed using a numerical routine given by Drayson (1975). The lineshape function using the Voigt profile $G(T, \nu, J, Br)$ is calculated using

$$G(T, P_{TOT}, Q, \nu) = \frac{2\sqrt{\ln 2} / \pi V(x, a(T, P_{TOT}, Q))}{\Delta\nu_D(T)} . \quad (2.5)$$

2.2.3 The measurement of temperature from the light absorption measurements of multiple transitions

The measurement of the transmission $I(\nu_0)/I_0(\nu_0)$ at the absorption frequency ν_0 for two different transitions can be used to calculate the temperature by relating the temperature to the ratio R (given by the ratio of Eq. (2.1) for two different transitions denoted by subscripts 1 and

2.) If the pathlength dl is sufficiently small, all properties can then be assumed to be constant over dl , allowing the removal of the integral in Eq. (2.1). Thus the ratio can be simplified to give

$$R(T, Q_1, Q_2) = \frac{S(T, Q_1) \Delta v_{D_2}(T, Q_2) V(0, a(T, P_{TOT}, Q_1))}{S(T, Q_2) \Delta v_{D_1}(T, Q_1) V(0, a(T, P_{TOT}, Q_2))} . \quad (2.6)$$

Once a tomographic reconstruction of the transmission field $I / I_0(v, x, y)$ for each point in the (x, y) domain is computed, a value of $R(T(x, y), Q_1, Q_2)$ for each point is obtained by dividing point-by-point the log of the transmission fields. Although T is not an explicit function of R , the temperature $T(x, y)$ can then be obtained via a table-lookup scheme using the CT reconstructed ratio $R(T(x, y), Q_1, Q_2)$ and finding the corresponding temperature from a table of calculated $R(T, Q_1, Q_2)$ versus T .

2.2.4 The measurement of concentration from reconstructed temperature and transmission profiles

Once the temperature field is computed, the concentration field $P_{CO}(x, y)$ can be calculated by backsubstituting the temperature field $T(x, y)$ into one of the tomographically reconstructed transmission fields and solving for P_{CO} using Eq. (2.1) and Eq. (2.2), with the infinitesimal pathlength of absorption dl equated to the small but finite tomographic sampling spacing Δs . Thus the concentration field $P_{CO}(x, y)$ is given by

$$P_{CO}(x, y) = \frac{\ln(I / I_0(v_0, x, y))}{-S_0 S(T(x, y), Q) G(T(x, y), P_{TOT}, Q, 0) \Delta s} . \quad (2.7)$$

Note that the calculation of the concentration requires an accurately measured pathlength. The pathlength in a non-tomographic absorption measurement is often difficult to obtain unambiguously because of the nature of a flame in free space. Using tomographic reconstruction however, only one pathlength between successive sampling points Δs is required. The sampling spacing can be measured very accurately with a micrometer translation stage. This is an important advantage of the tomographic technique when quantitative measurements of the concentration are desired.

2.2.5 Tomographic reconstruction technique

The use of line-of-sight absorption measurements for CT reconstruction generally requires the measurement of M equally spaced beams along N different angles (Santorro *et al.*, 1980). From this $M \times N$ data set, the spatially resolved reconstruction of the property field F can be calculated. However, with the assumption of axisymmetry, only an $M \times 1$ data set is required. Let the property field F to be reconstructed be given by the absorption coefficient α , previously defined by Eq. (2.2). Recall that the transmission of a beam through an absorbing media is given by the Lambert-Beer Law, given by Eq. (2.1) which can be expressed in a pathlength integrated form as

$$-\ln \frac{I(\nu, r, \theta)}{I_0(\nu, r, \theta)} = P(r, \theta) = \int_{-s}^s \alpha^F(x, y) ds, \quad (2.8)$$

where $I(\nu, r, \theta)/I_0(\nu, r, \theta)$ is the normalized transmission of the absorbing species at frequency ν , radius r and angle θ . $P(r, \theta)$ is defined as the projection of the

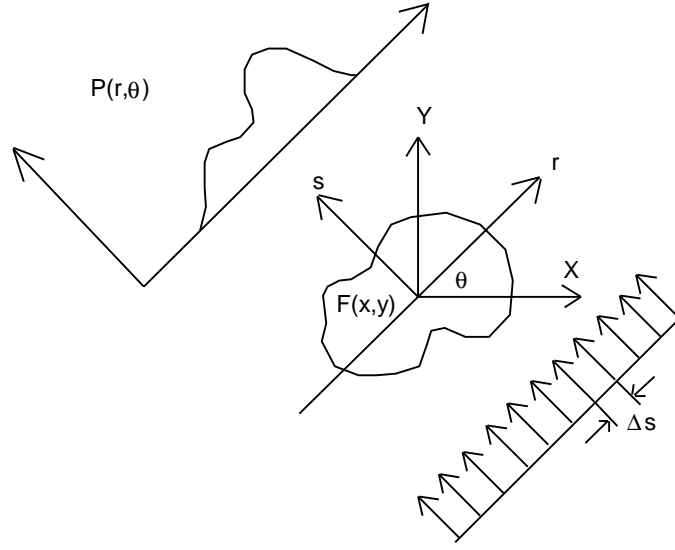


Figure 2.1: The projection of $P(r, \theta)$ of a property field $F(x, y)$ along ds at angle θ .

property $F(x, y)$ at angle θ and ds is the infinitesimal pathlength of integration. The relation between the property field and the projection along an angle θ can be seen in Fig. 2.1. The projection $P(r, \theta)$ is in polar coordinates and can be related to rectangular coordinates in (x, y) using $r = x \cos \theta + y \sin \theta$ and $s = -x \sin \theta + y \cos \theta$. Thus the measured normalized transmission $I(v, r, \theta)/I_0(v, r, \theta)$ determines the projection $P(r, \theta)$ and the solution of Eq. (2.8) will result in the property field $F(x, y)$ of the scanned area.

2.2.6 CT reconstruction algorithm

The tomographic reconstruction algorithm used in this paper is adapted from the Fourier convolution technique used by Santorro *et al.* (1980). The solution of Eq. (2.8) using the Fourier convolution integral technique can be expressed as

$$F(x, y) = \frac{1}{2\pi} \int_0^\pi \int_{-\infty}^\infty P(r, \theta) \phi(x \cos \theta + y \sin \theta - r) dr d\theta. \quad (2.9)$$

This equation can be approximated by a discrete summation over all N projection angles and M sampling positions along r and is given by

$$F(x, y) = \frac{\Delta s}{2N} \sum_{j=1}^N \sum_{k=1}^M P(r_k, \theta_j) \phi(x \cos \theta_j + y \sin \theta_j - r_k), \quad (2.10)$$

where $\phi(r)$ is a filter function, $\theta_j = (j-1)\pi / N$, $r_k = k \Delta s$, and Δs is the spacing between uniform samples. In order to accurately reconstruct $F(x, y)$, the filter function $\phi(r)$, has to be chosen so that its bandwidth retains all the essential features of the data yet rejects the high frequency components of the data (Kwoh *et al.*, 1977). The filter used in this paper was the Shepp-Logan filter originally used for X-ray CT reconstructions of the human head (Shepp and Logan, 1974). The Shepp-Logan filter is given by

$$\phi(r_k) = \frac{-4}{\pi \Delta s^2 (4k^2 - 1)}. \quad (2.11)$$

In addition to using the correct filter function, the number of angles for summation N has to be sufficiently large to minimize aliasing (Hughey and Santavicca, 1982). The implementation of this algorithm in FORTRAN can be found in Appendix B.

2.2.7 Determination of the number of sampling intervals

The number of sampling intervals M required for the accurate reconstruction of the original property field is given by the Nyquist sampling frequency, which for an axisymmetric flow field is (Steiglitz, 1974)

$$M = \frac{R \omega_{MAX}}{\pi} , \quad (2.12)$$

where R is the outer radius of the flow field (in cm) and ω_{MAX} is the maximum spatial frequency (in cm^{-1}) of the field. The maximum spatial frequency is the inverse of the smallest length scale found in the property field; the smallest length scales are normally found at locations of steep scalar gradients.

2.3 Experimental

2.3.1 Optical configuration

Figure 2.2 shows a schematic of the optical arrangement of the experiment. The single-mode infrared emission from a lead-salt (Pb-salt) diode laser (Laser Analytics, model LL5621), mounted in a liquid nitrogen (LN2) cooled dewar (Laser Analytics, model L5736) operating at about $4.8 \mu\text{m}$ wavelength is collimated using a gold coated off-axis parabolic mirror (Janos Technologies, model A8037-256). The collimated laser light is then directed through a chopper

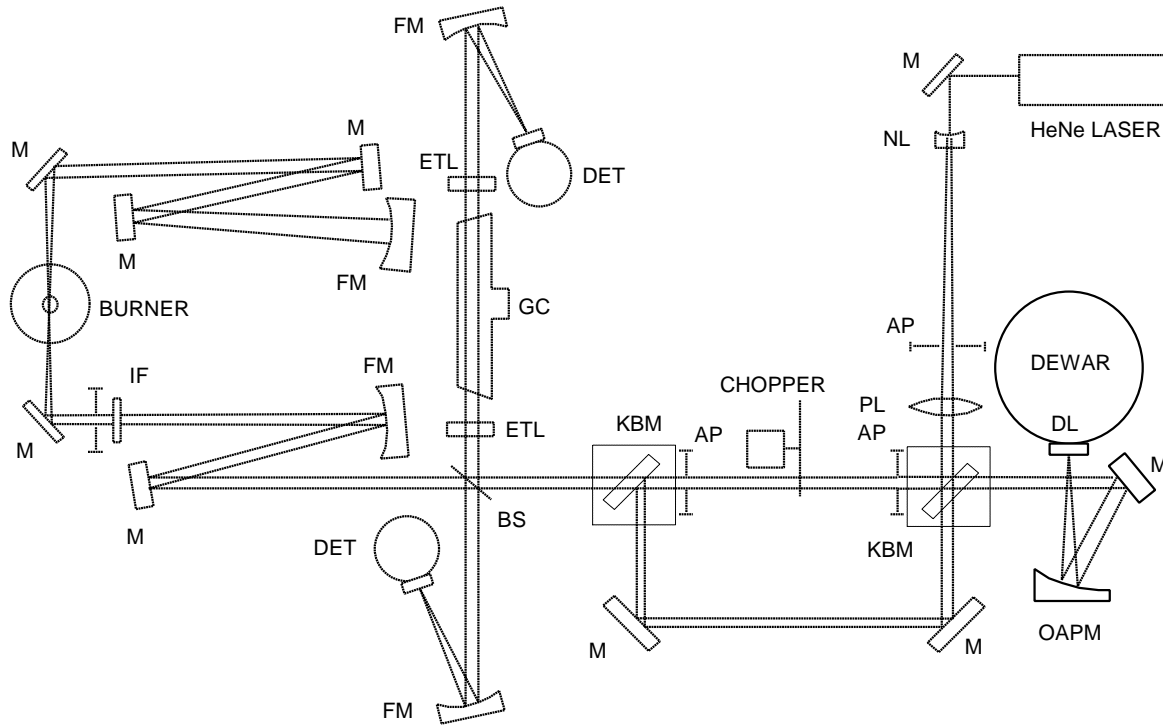


Figure 2.2: Schematic of optical layout for direct absorption measurements. Legend: DL = diode laser, OAPM = off-axis parabolic mirror, M = flat mirror, KBM = kinematic base mirror, AP = aperture, BS = beamsplitter, FM = focusing mirror, IF = interference filter, ETL = etalon, GC = gas cell, DET = InSb detector-preamplifier, NL = negative lens, PL = positive lens.

wheel operating at 1 kHz, a pellicle beamsplitter splits off a fraction of the chopper modulated beam which is then focused onto a LN₂ cooled InSb detector-preamplifier (Cincinnati Electronics, model SDD-1963-S1) to monitor the non- absorbed signal intensity. A mirror with a focal length $f = 76.2$ cm focuses the remaining light transmitted by the pellicle beamsplitter to a measurement zone above the burner. The diode laser beam passes through the measurement zone with an approximate diameter of 200 μm . After passing through the measurement zone the beam is then refocused by another mirror with focal length f , situated at a distance equal to the mirror's radius of curvature ($2f$) and the beam is redirected along the same path back through the measurement zone through an aperture and a long-wavelength pass filter with a cutoff wavelength of 4.5 μm . The filter in conjunction

with the sapphire window on the InSb detector form a bandpass filter which admits light within the wavelength range of 4.5 to 5.5 μm – effectively reducing the background infrared radiation from the flame. A fraction of the light passing through the longpass filter is split off from the returning beam by the other side of the pellicle beamsplitter and is then focused onto a second InSb detector-preamplifier that measures the transmitted signal intensity. The first InSb detector is also used to monitor the relative variation of laser frequency during the scan across a spectral feature by the use of a low finesse air spaced Fabry-Perot etalon ($\text{FSR} = 0.0172 \text{ cm}^{-1}$) formed by two ZnSe windows mounted on removable kinematic bases. A 22-cm pathlength calibration absorption cell with sapphire windows, also on a removable kinematic base, is in the laser light path of the first detector. This cell is used in conjunction with bottled gases: carbonyl sulfide (OCS) and CO for the spectral characterization of the laser frequency. The signal from the first detector can be used to normalize the transmitted laser intensity reaching the second detector once the etalon and gas cell are removed from the light path. The alignment of the invisible infrared laser light is accomplished by superimposing a visible HeNe laser beam onto the infrared beam by means of a mirror system mounted on removable kinematic bases (Silver and Stanton, 1991).

Our optical arrangement has several benefits. The variation in the transmitted laser intensity due to thermally induced beamsteering is significantly reduced by sending the beam back through the same path in the flame (accomplished by placing the backreflecting spherical mirror at $2f$ of the initial focal point (Born and Wolf, 1975). This technique is adapted from a similar method previously used by Dibble (1975) for shock tube studies. The reduction in variations of the signal due to beamsteering substantiate the absorptions as being caused by the species of interest and not by the inadvertent movement of the beam off the detector element. The second benefit is an increase in the absorption pathlength due to the backpropagating beam, effectively doubling the detection sensitivity.

2.3.2 Electronics and instrumentation configuration

Figure 2.3 shows the instrumentation and electronics used in this experiment. A battery powered, ultra low-noise precision current source (ILX Lightwave, model LDX-3620) provides

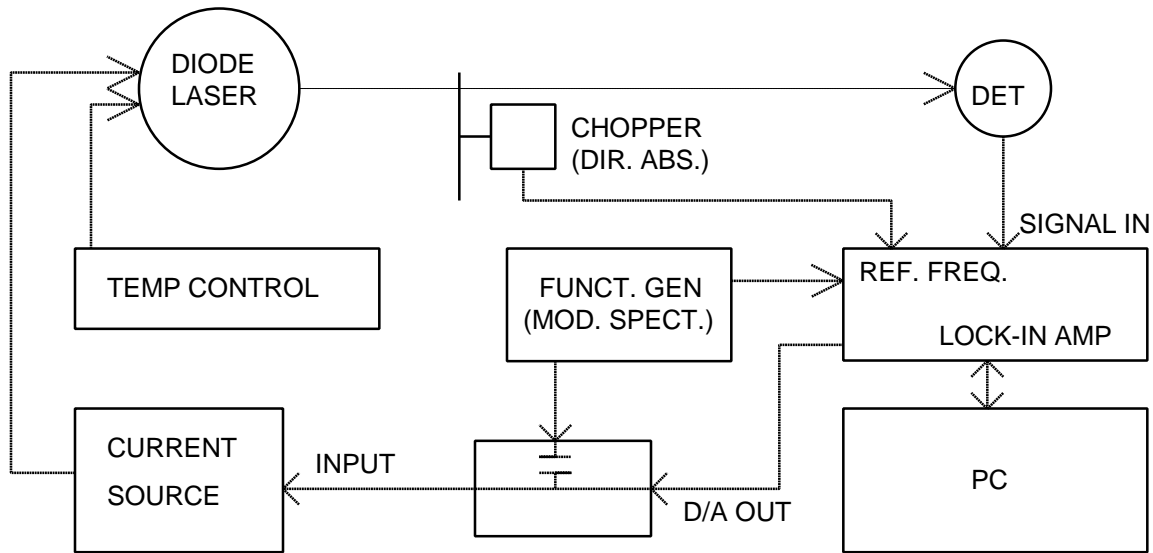


Figure 2.3: Schematic of the electronics and instrumentation used for these measurements. For the spectral shift measurements using modulation techniques, a second lock-in amplifier was used with a second detector (both not shown).

the injection current for the diode laser. The current source is controlled by the programmable digital to analog (D/A) output from the lock-in amplifier (Stanford Research, model SRS 530) which removes the background noise from the detector signals. An ultra low-noise cryogenic temperature controller (Lakeshore Cryotronics DRC-91CA) regulates the temperature of the diode laser to within 5 mK at 100 K. A PC records the transmission signal from the detectors after being processed by the lock-in amplifier. Batteries provide low noise power to the indium-antimonide (InSb) detector-preamplifiers. For the direct absorption measurements, the lock-in amplifier was referenced to an optical chopper operating at 1.2 kHz. For the modulation spectroscopy measurements, the lock-in amplifier was referenced to a function generator operating at about 10 kHz. The sine-wave output from the function generator was capacitively coupled to the D/A output from the lock-in amplifier providing a modulated input for the current source.

2.3.3 Burner-Flow arrangement

Figure 2.4 shows the details of the burner and the associated flow system. A pressure regulated supply of methane is metered using a rotameter and mixes with dry-house air after passing through a series of check valves and flashback suppressors. The house air for both the premix and coflow are metered with rotameters. The methane-air mixture is introduced to the burner, which is constructed from an 82 cm long, 17 mm ID, 19 mm OD stainless steel tube surrounded by a 70 mm diameter aluminum coflow matrix. After flowing through a fine wire mesh screen located at the inlet of the burner (intended to mix the methane-air mixture and to provide flashback protection), the mixture

developed a laminar velocity profile upon exiting. The requirement of a predictable laminar velocity profile is important in numerical modeling aspects. Small glass beads (2.5 mm dia.) in conjunction with an aluminum honeycomb matrix provide a uniform stream of coflow air which stabilizes the rich premixed flame from flickering. For the rich flame conditions encountered (see Table 2.1), the flame had the well known double-cone Bunsen-type structure characterized by an inner rich-premixed flame zone and an outer non-premixed flame zone. The laser probe volume was located 21 mm above the burner exit --- a location chosen to coincide with the middle of the double-cone flame zone. Although significant thermal gradients exist at this location, the optical arrangement provides adequate beamsteering correction. A translation stage with 25 μm resolution translates the burner radially with respect to the laser probe volume.

Table 2.1: Burner operating conditions.

Equivalence Ratio:	1.56
Methane Flowrate:	1.06 liters/minute
Air Flowrate:	6.50 liters/minute
Coflow Rate:	70.8 liters/minute
Outer/Inner Flame Height:	95/42 mm

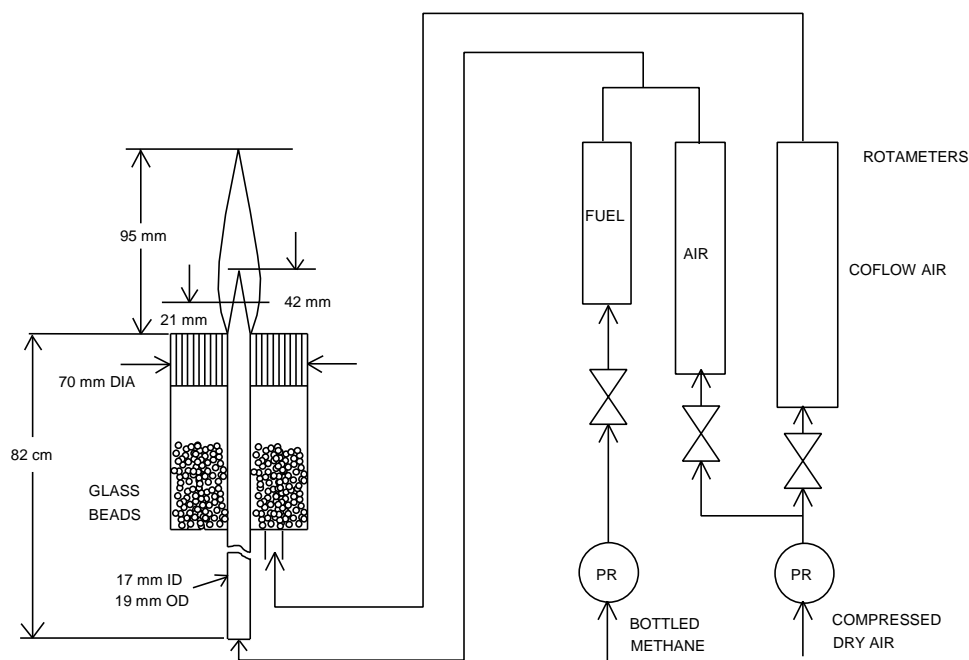


Figure 2.4: Schematic of the Bunsen burner, the laser measurement zone, and the associated flow system. The coflow arrangement helped to provide an extremely stable and flicker free flame. PR = pressure regulator.

2.3.4 Experimental procedure

2.3.4.1 Adjusting the laser frequency to access a transition

The laser frequency is adjusted to a rovibrational transition of interest by varying the laser temperature and current. The laser frequency is verified using spectral scans across low-pressure, Doppler broadened absorption lines of OCS gas in the calibration cell. The absorption scan spectrum is compared with a high resolution spectral map of OCS (Hunt *et al.*, 1984) and the laser frequency is thus assigned unambiguously. The laser is operated near the threshold lasing current to ensure single-mode operation. Once the desired laser frequency is achieved, a second check is made by performing the same frequency scan across pure CO at approximately 5 torr. With the second detector connected to the input of the lock-in amplifier, the laser is scanned without the flame to establish a non-absorbed spectrum $I_0(\nu)$.

2.3.4.2 Determination of the minimum number of sampling points

After establishing the flame conditions shown in Table 2.1. The flame was observed to have a luminescent radius of approximately 1.3 cm at the axial location of the laser probe volume, thus a total traverse of 1.33 cm in the radial direction was chosen in order to span the measurement zone. Data points outside of the non-premixed flame zone were unnecessary since the concentration of CO past the outer flame contributed an insignificant amount of laser light absorption. The number of sampling points along the radius of the flow field was determined with the help of Eq. (2.12). For a finite sampling spacing of 0.635 mm (approximately 3 probe volume diameters) and with a measurement radius of 1.33 cm, the number of sampling points is 21. From Eq. (2.12) the maximum resolvable spatial frequency is approximately 50 cm^{-1} .

2.3.4.3 Collection of absorption data in the flame

The position of the laser probe volume with respect to the flame was noted and the laser frequency was scanned across the absorption transition. The transmission data is stored by computer. The burner is moved by an increment of 0.635 mm to the next scan position. 21 scans are performed for each CO transition of interest, covering the width of the measurement zone. Another scan is made with the flame extinguished to verify that the laser intensity did not vary significantly during the time interval of the 21 scans. A change in the laser intensity at the initial scan frequency was observed to be typically less than 2% for the duration of the scans (approximately 20 minutes). The first detector is then reconnected to the lock-in amplifier and a final scan is then performed with the ZnSe etalon in place to establish the frequency tuning

characteristics of the laser as a function of laser current and was found to be extremely linear over the typical scan window of 0.5 cm^{-1} .

2.3.5 Modulation spectroscopy

On the lean side of the Bunsen flame, the CO concentration drops rapidly to the ppm level. With our present direct absorption technique, we are unable to see this small amount of CO. In direct absorption, the detection of a small attenuation of ΔI out of a large non-zero background I is required, this limits the detection sensitivity to an absorption of about 10^{-3} . We therefore implemented modulation spectroscopy to increase the detection sensitivity (Reid and Labrie, 1981) to resolve the lower concentrations of CO in the lean regions of the flame. Modulation spectroscopy involves slowly sweeping the laser wavelength, say at 1 Hz, through the absorption feature while rapidly modulating, at a frequency f , say 10 kHz, the wavelength of the laser at an amplitude that is small compared to the sweep amplitude. For the highest sensitivity, the optimal modulation amplitude is nearly equal to the line width of the absorption feature (Arndt, 1965). The interaction of the modulated laser probe with the absorption feature generates a signal at higher harmonics of f , for example, $2f$, $3f$, etc. Any of these harmonics can be used, however, Silver (1991) argues that the optimal signals are generated at the second harmonic or $2f$. The improved sensitivity of the $2f$ technique results in part from the generation of a signal at the second harmonic where there is otherwise a zero baseline.

In practice, modulation spectroscopy involves superimposing a small sinusoidal current (μA) onto the diode laser injection current (mA) while the injection current is steadily increased. As the current is increased the diode laser wavelength changes towards the blue (shorter

wavelengths), concurrently the laser power also increases. In this way, the wavelength of the laser is scanned across an absorption feature, such as the CO infrared transition. The $2f$ signal is detected using a lock-in amplifier. The $2f$ signal closely approximates the second derivative of the absorption lineshape for small modulation amplitudes. Because of the derivative nature of the signal, the sloping power background of the laser is removed and the baseline signal in the absence of absorption is zero.

We characterized the detection sensitivity of our laser diode system in the $2f$ mode by probing CO in the hot post flame region of a metal matrix flat flame burner (rectangular 13-cm by 18-cm), supplied with premixed methane-air. Our initial measurements showed that the detection of ppm levels of CO in a flame were limited by the absorption of the laser beam by the ambient levels of CO in the laboratory (approximately 0.5 ppm). To avoid this, we chose the P(38) transition as it was reasonably populated at flame temperatures while being unpopulated at room temperatures.

2.4 Results

2.4.1 Measurement of CO spectra in the flames

The P(20) ($\nu = 2 \leftarrow 1$, $\nu_0 = 2034.135 \text{ cm}^{-1}$) and the P(27) ($\nu = 1 \leftarrow 0$, $\nu_0 = 2027.649 \text{ cm}^{-1}$) rovibrational transitions of CO were measured. The transitions were chosen primarily to avoid interference from nearby water rovibrational transitions. The temperature dependence of the transitions was also a factor in the selection process. Using the quantum mechanical model for CO described earlier (Varghese and Hanson, 1980), the Boltzmann populational dependence of the transitions were observed as a function of temperature. The vibrationally excited or ‘hot’

P(20) transition is very temperature dependent (good for thermometry), whereas the P(27) transition was chosen for its relative temperature independence (good for concentration measurements). The data was typically collected over a 20 second scan interval. The data was correlated to actual frequency units of cm^{-1} (for future spectral width analysis) using an air spaced ZnSe Fabry-Perot etalon ($\text{FSR}=0.0172 \text{ cm}^{-1}$) to provide the diode laser tuning characteristics as a function of injection current.

2.4.2 Results of CT reconstruction

2.4.2.1 Verification of CT reconstruction of the flame data

Figure 2.5 shows the pathlength integrated line-center normalized transmittance measurements through the flame as a function of radius for the P(20) and P(27) lines. R_{max} is the maximum radius of the scan (1.33 cm), corresponding approximately to the maximum flame diameter at the axial plane of measurement. The CT reconstructed backprojection is also shown to verify the accuracy of the reconstruction. The reconstruction was performed on a total data set of 29 points, with 8 buffer points at the edge which are not shown, all

subsequent reconstructions used 30 projection angles N . The agreement in the middle of the flame is good, but small deviations appear towards the edge of the flame.

2.4.3 Calculation of the temperature profile

From Eq. (2.6), the flame temperature was calculated using the ratio $R(P(20)/P(27))$. The correlation of the ratio $R(T, Q_1, Q_2)$ and the temperature T was calculated for 50 different temperatures from 300 K to 2800 K using the quantum mechanical model of CO (Varghese and Hanson, 1980). Since the temperature cannot be explicitly expressed as R , the reconstructed temperature profile was calculated by linear interpolation of T given R as the input. Figure 2.6 shows the reconstructed temperature profile of the flame based on the ratio obtained from the log

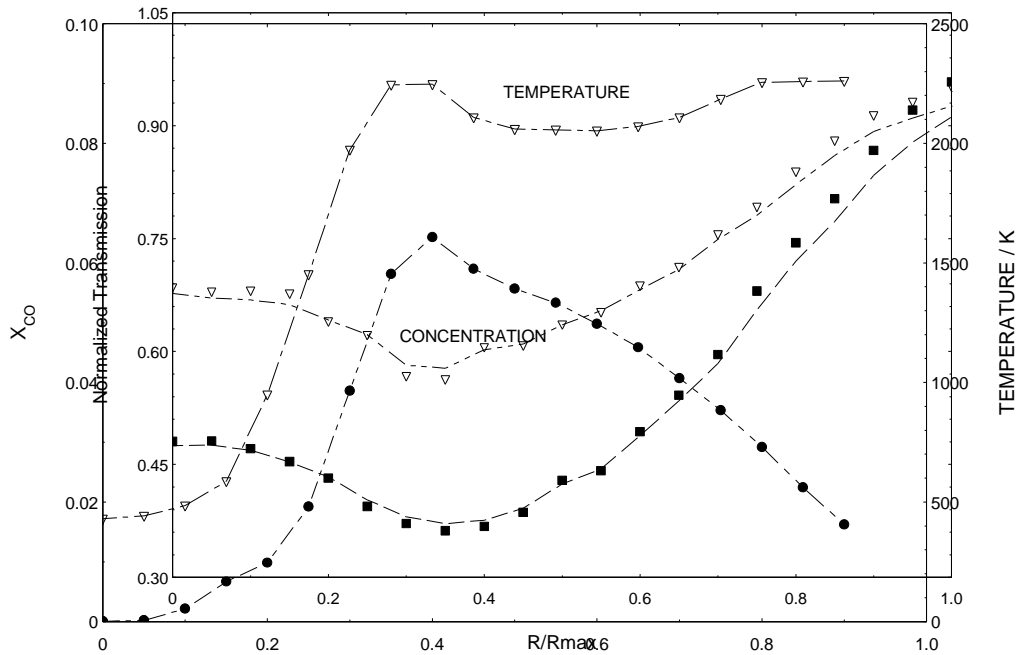


Figure 2.5: Comparison of line-center, measured pathlength integrated transmission data with CT reconstructed backprojections for the P(20) and P(27) transitions. The points represent the P(20) (triangles) and the P(27) (squares) measured data. The curves represent the CT reconstructed backprojection for the P(20) (right dashes) and the P(27) (left dashes) backprojection.

of the transmittance for the P(20) and P(27) transitions. The temperature is low in the center of the flame and rapidly increases approximately to the adiabatic flame temperature for a methane-air flame (2226 K). The temperature then decreases by about 200 K and later increases to the adiabatic flame temperature again at the outer non-premixed flame region. Beyond the non-premixed flame region there is significantly less CO, this contributes to an increased uncertainty in the measured transmission signal. The high temperature at the inner-flame zone is probably the result of an overshoot and ringing effect in the CT reconstruction process referred to as Gibb's phenomena (Bracewell, 1978). Gibb's phenomena is typically caused by steep scalar gradients (such as the inner-flame temperature gradient). The extent of the distortion of the temperature profile due to this effect prompts further investigation using an alternative diagnostic technique. Other possible sources of error in the measurements could also arise from the low absorption signals at the outer edges of the flame contribute to noisy derivations of the temperature due to the sensitivity of the division process to small numbers. The temperature was observed to be quite sensitive to errors in the reconstruction process, an observation also noted by Hughey and Santavicca (1982) in their simulated data CT reconstructions.

2.4.4 Calculation of the CO concentration profile

Figure 2.6 also shows the mole fraction of CO calculated by backsubstituting the temperature and the transmission per unit pixel calculated from Fig. 2.5 into Eq. (2.7) and solving for P_{CO} . Since the beam travels through the measurement zone twice, Δs has to be doubled to account for the increase in the pathlength. The concentration profile yields reasonable values for CO. The maximum concentration occurring at approximately the inner flame region, agrees well with equilibrium calculations for the given equivalence ratio. The concentration is zero at the center of the flame, this is expected since the premixed gases are still unburned. The concentration peaks near the location of the inner flame interface (based on the peak in the temperature profile) and gradually decreases to zero again towards the outer non-premixed flame.

2.4.5 Results of low level detection of CO using $2f$ spectroscopy

2.4.5.1 Measurements of spectral shifts in gas cells and flat flames

Figure 2.7 shows the $2f$ spectrum of the P(38) ($\nu = 1 \leftarrow 0$, $\nu_0 = 1973.8916 \text{ cm}^{-1}$) transition of CO in hot combustion gases recorded simultaneously using 7 torr of pure CO at 299 K in a 22-m pathlength reference cell. The measurement of the hot CO was performed above a methane-air ($\phi = 0.85$), metal matrix burner mentioned previously. The dashed curve represents the spectrum of the reference

cell while the solid curve is the measurement above the burner. An obvious shift of the line-center of the flame spectrum to the blue (shorter wavelengths) can be seen. This shift was observed to decrease with increasing equivalence ratio. Figure 2.8 shows that the variation of shift of the P(38) transition with equivalence ratio. As can be seen, the blue shift in lean flames is about $+0.009 \text{ cm}^{-1}$. An artificial blue shift in the peak can also be caused by a distortion of the $2f$ spectrum as a result of the modulation spectroscopy technique (imposed by finite laser wavelength modulation amplitudes and a sloping laser power background). We have examined this artificial shift using a numerical model of the $2f$ modulation technique similar to the model reported by Reid and Labrie (1981) and Philippe and Hanson (1992), and find it to be less than 0.001 cm^{-1} . Thus the shifts are indeed real and are not a result of the instrumental function

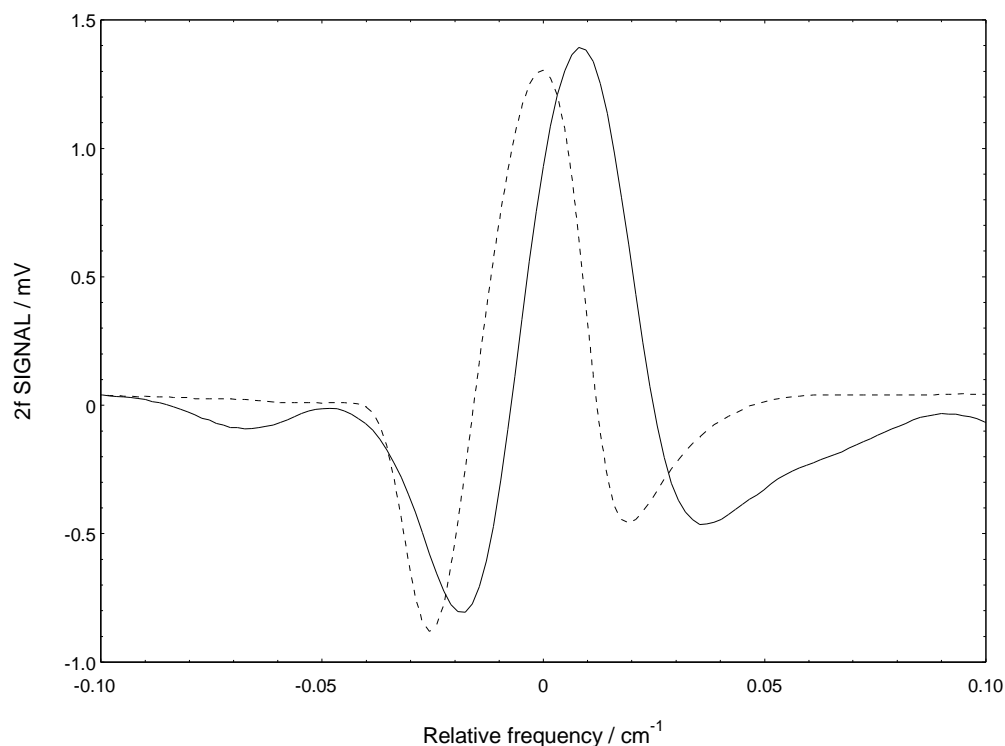


Figure 2.7: The $2f$ spectrum of the P(38) ($v = 1 \leftarrow 0$) transition of the hot combustion gases above a methane-air flat-flame operating at an equivalence ratio of $\phi = 0.85$ (solid curve) and the simultaneously measured unshifted reference spectrum of pure CO at ambient temperature and a pressure of 7 torr.

(Appendix C contains the FORTRAN codes used to model these modulation shifts). The presence of an asymmetry suggests that the lineshape function could be modeled more accurately with a Galatry profile (Ouyang and Varghese, 1989; Galatry, 1962), which accounts for both a shift and asymmetry of the lineshape. A Voigt profile however has been adequate for our present purposes.

2.4.5.2 Earlier observations of spectral shifts in CO

Spectral shifts due to collisions with neighboring molecules are discussed by Mitchell and Zemansky (1971), much of the previous work relates to atomic species in emission (Ch'en and Takeo, 1957; Thorne, 1988). Philippe and Hanson (1992) report a red shift in O_2 with increased temperature and number density. Line center shifts of the first overtone band of CO ($v = 2 \leftarrow 0$),

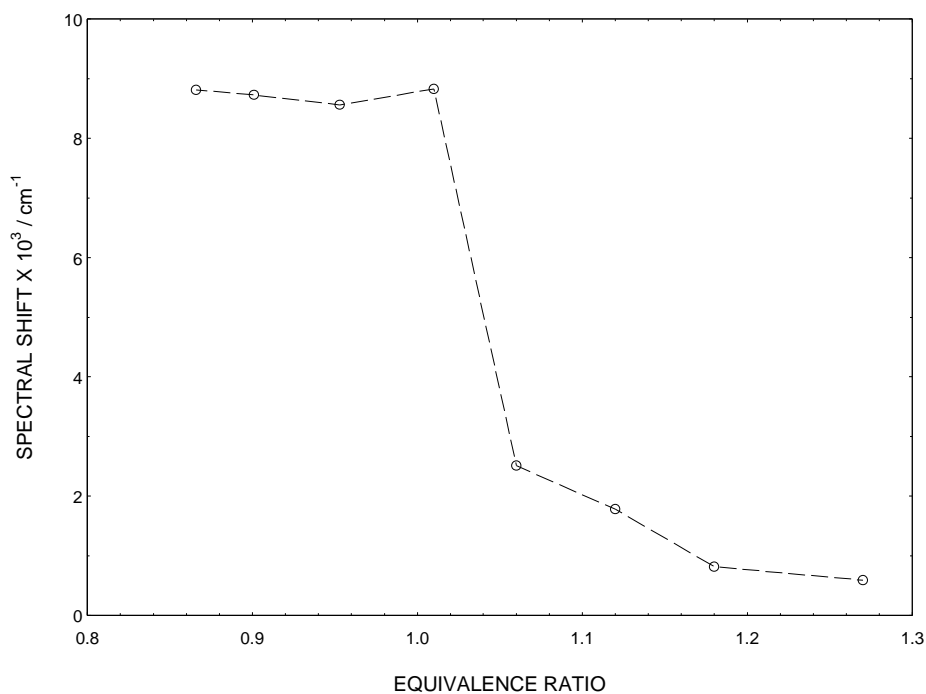


Figure 2.8: The spectral shift of the P(38) ($v = 1 \leftarrow 0$) transition as a function of equivalence ratio for a methane-air flat-flame burner. The shifts are referenced to a Doppler broadened pure CO cell at 7 torr at ambient temperature with a pathlength of 22-m.

broadened by other molecules as well as by CO itself were reported by Bouanich and Brodbeck (1973). Their measurements were performed at ambient temperatures and showed spectral shifts to the red only. The maximum shifts reported by Bouanich and Brodbeck (1973) were approximately $-0.005 \text{ cm}^{-1} \text{ atm}^{-1}$ for a rotational level of $J = 20$ with the trend increasing approximately linearly in J . These shifts are comparable to what we have observed at room temperature. Blue shifts are usually associated with Helium colliders, the argument being that He has a low polarizability, hence a low well depth, ϵ for the attractive part of the intermolecular potential (Thorne, 1988). At room temperatures the kT/ϵ term for He is relatively larger than other molecules found in combustion products. The He collisions thus primarily interact with the ‘hard sphere’ part of the intermolecular potential (the C_{12} term in the Lennard-Jones potential) (Sobelman *et al.*, 1981). In the lean flame, the high temperatures reduce the density and thus the effect of induced dipoles between molecules is less pronounced. Furthermore, the high temperatures of the flame increases the collisional speed between molecules which results in the colliders behaving more like He, thus the repulsive ‘hard sphere’ part of the intermolecular potential increasingly dominates the collision – with the observable consequence that CO in lean flames is shifted to the blue.

2.4.5.3 The effect of the perturbers H_2 and CO on blue spectral shifts

In the fuel rich flames, the blue shift of CO ($J = 38$) is compensated by something such that there is basically no shift, although a slight asymmetry in the $2f$ profile is observed with respect to the reference $2f$ spectrum. The major change between fuel lean products and fuel rich products is the appearance of H_2 and CO in the 1 to 8 percent levels while O_2 is now absent. We have explored the effect of CO ($J = 38$) collisions with H_2 and with CO in a room temperature

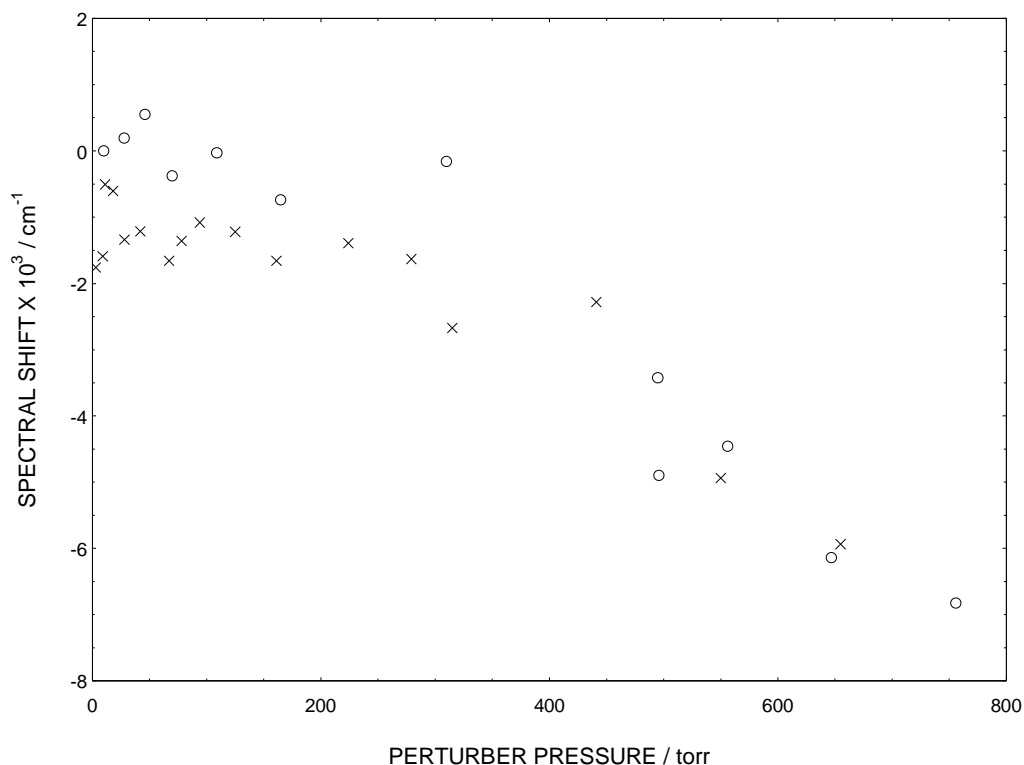


Figure 2.9: The spectral shift of the P(38) CO transition as a function of perturbors: CO (circles) and H_2 (crosses) at varying perturber pressures.

cell. As Fig. 2.9 shows, increased number density of either CO or H_2 produces a red shift in the CO absorption center frequency. However, the shifts at room temperature are not large enough, by themselves, to account for the change observed at flame temperatures seen in Fig. 2.8. We *speculate* that the higher temperatures of the flame created a wider distribution in the states of the colliders, and that such molecules have, on average, higher levels of rovibrational thermal excitation. As such, an increasingly larger fraction of the CO collider molecules will have J levels that approach that of the CO ($J = 38$) molecule. In particular, CO resonance effects will be more pronounced (Yardley, 1980). Further research into the physical explanation of this phenomena is in order. For the present purposes, the shift in the CO P(38) is large enough that the tomographic reconstruction of the

flame in the lean zones will require inclusion of this effect of line center shifts. Alternatively, one can use a lower rotational level, such as P(8) ($v = 1 \leftarrow 0$, $\nu_0 = 2111.5435 \text{ cm}^{-1}$), where line center shifts are less pronounced and can be neglected in the tomographic reconstruction. However, the absorption of the laser beam due the ambient levels of CO in room air will have to be dealt with.

Chapter 3

An Experimental and Numerical Comparison of Extractive and In-situ Laser Measurements of Non-Equilibrium Carbon Monoxide in Lean-Premixed Natural Gas Combustion

3.0 Chapter Overview

Measurements of carbon monoxide (CO) in the high temperature combustion product stream of an atmospheric pressure, lean-premixed combustion, natural gas reactor were obtained using line-of-sight tunable diode laser absorption and extractive probe sampling in conjunction with non-dispersive infrared analyzers over various equivalence ratios and flow residence times. The measurements are compared to (1), a numerical model using comprehensive chemical kinetics for methane combustion in conjunction with perfectly-stirred reactor (PSR) and plug-flow reactor (PFR) modeling approaches, and (2), chemical equilibrium at the measured temperature. The temperatures ranging from 1500 to 2000 K were measured using a radiation corrected

thermocouple and also by a diode laser thermometry technique. The laser based in-situ measurements of CO concentration ranged from 50 to 5000 ppm depending on the equivalence ratio and flow residence time.

Results of the numerical model were consistent with the laser based measurements. The extractive probe measurements were found to be as much as 10 times less than the laser based measurements. However, laser and probe measurements for fuel-rich equivalence ratios agreed. In an effort to improve the performance of extractive sampling probes, we tested several aerodynamic quench probe designs. We were unable to achieve an aerodynamic quench of the CO in a high temperature combustion product stream. A model of the sampling probe as a PFR indicates that extractive sampling of [CO] is increasingly inaccurate as gas temperatures increase above 1000K.

3.1 Introduction

Most low-NO_x combustion techniques rely on lowering the temperature of combustion to avoid the formation of thermal NO_x. Operation at fuel-lean equivalence ratios usually achieves the desired low temperature characteristics. Consequently, lean-premixed combustion (LPC) is being developed and implemented as a means of meeting the strict source emissions standards of NO_x imposed on stationary gas-turbine power generation systems. In addition to flame stability issues at lean equivalence ratios, the emission of carbon monoxide (CO) and unburned hydrocarbons ultimately limits fuel-lean operation in LPC systems (Correa, 1992; Lovett and Abuaf, 1992). The primary channel of CO oxidation is through the reaction $\text{CO} + \text{OH} = \text{CO}_2 + \text{H}$ (Howard *et al.*, 1973; Baulch and Drysdale, 1974; Westbrook and Dryer, 1984). At lower equivalence ratios, the lower temperatures reduce the levels of OH. The lack of OH limits the

rate which CO can be converted to CO₂ and, thus exacerbates the problem of CO emissions for lean operation. Correa (1992) has pointed out that in order to predict CO emissions in 3-dimensional, turbulent flames, a critical need exists for the development and measurement of [CO] (braces denote concentration) in high-temperature, non-equilibrium.

The measurement of [CO] has traditionally been performed using extractive probes in conjunction with non-dispersive infrared (NDIR) analyzers. Extractive sampling techniques are well suited for lower temperature applications where the [OH] is very low. It is well known that suction probe sampling of hot CO in flames can be potentially erroneous; one goal of this research is to determine the extent of this discrepancy. Previous research related to this study include the work by Malte and Kramlich (1980), showed that probe measured [CO] was a function of sampling pressure. Schoenung and Hanson (1981), reported that discrepancies exist between extractive sampling and in-situ diode laser [CO] measurements above a flat flame burner. A goal of our research is to determine the extent of this discrepancy in the hot, reactive combustion gases of an LPC system. We extend the direct absorption technique used by Schoenung and Hanson (1981) by employing modulation spectroscopy to increase the detection sensitivity of [CO]. Since LPC systems typically operate at equivalence ratios well below 0.85, the corresponding levels of CO emission are typically in the tens to hundreds of ppm's.

In this study, measurements of [CO] at various equivalence ratios and residence times in the reacting flow of a LPC reactor fueled by natural gas and air are obtained using (1), tunable diode laser spectroscopy, and (2), by extractive probe sampling using cooled aerodynamic and non-aerodynamic quench probes in conjunction with non-dispersive infrared (NDIR) analyzers. The experimentally measured values will be compared with values obtained from a numerical model

using detailed chemical kinetics in conjunction with various simplified fluid mechanical models and by equilibrium at the measured temperature. The paper is organized as follows: (1) a description of the combustor geometry, experimental apparatus and technique, including a short background on tunable diode laser spectroscopy, (2) a description of the approach used to model the LPC reactor using simple fluid mechanical models in conjunction with the chemical kinetics and, (3), the results of the measurements and modeling will be presented and the significance of the findings compared and discussed.

3.2 Experimental Apparatus

3.2.1 Combustor -- Flow System

The design of the combustor was guided by: (1) the flame stability issues at a variety of lean equivalence ratios, and (2) the requirement that the measurement zone properties such as CO concentration and temperature profiles be homogeneous to simplify both the numerical modeling and the extractive probe and in-situ measurements using a line-of-sight technique. Figure 3.1 shows a schematic of the combustor and the extractive probe sampling system. The natural gas and house air were both metered using non-sonic knife-edged orifice flow meters calibrated with

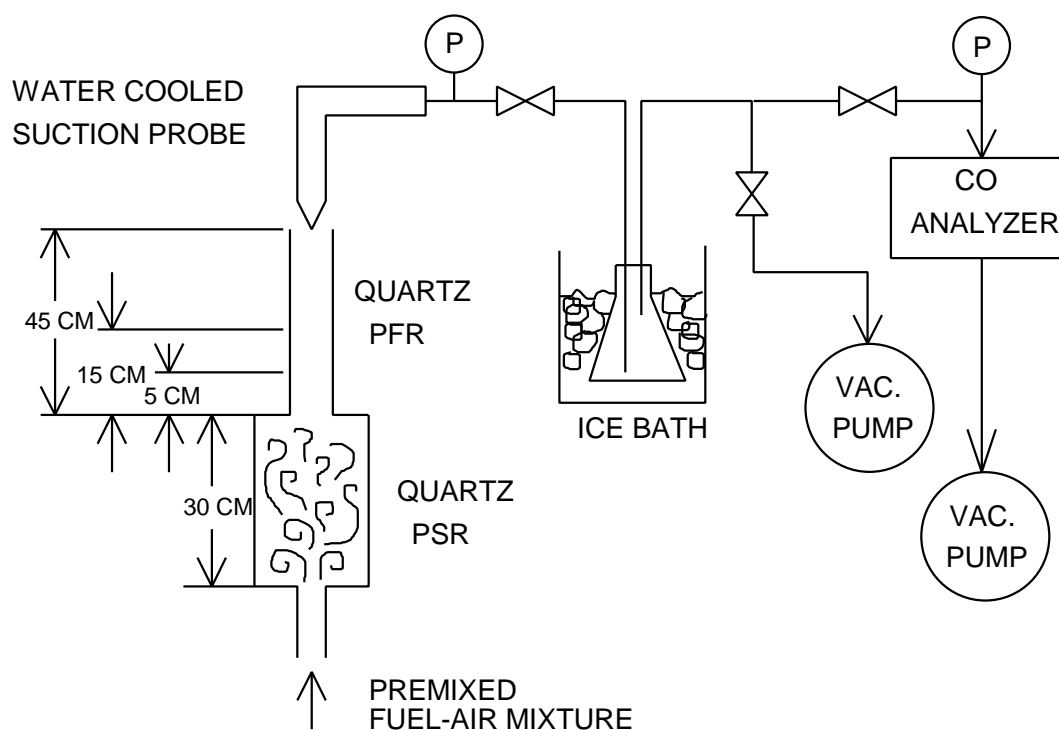


Figure 3.1: Schematic of the LPC reactor and probe sampling system. The 65 mm diameter quartz tube serves as the PSR, and the 40 mm quartz tube serves as the PFR. The measurement zone is located 2 mm downstream of the PFR exit plane and the pathlength is defined by the PFR diameter. The probe system uses multiple valves and vacuum pumps to maintain the NDIR sample pressure constant while allowing the probe pressure to vary. Three different water cooled probes were used with this flow sampling arrangement.

a Roots type volume displacement meter. Electronic digital manometers measure the pressure drop across the orifice plates. Pressure regulators control the flow rates upstream of the orifice plates. The typical operational flowrates were approximately 300 to 600 SLM of air and 25 to 50 SLM of natural gas. The equivalence ratio was calculated using the composition of the natural gas provided by the local gas company. The premixed natural gas-air mixture was introduced to the combustor reaction chamber through a perforated metal plate flame arrestor. Two ceramic plates with holes formed the upper and lower boundaries of the 65 mm ID quartz tube chamber. The flame was stabilized inside the chamber by the recirculation induced by the sudden expansion of the pipe diameter from 20 mm to 65 mm. The 300 mm length of the quartz reactor was modeled as a perfectly stirred reactor (PSR) and provides approximately a 30 ms residence time. The hot combustion products exiting from the 65 mm diameter quartz tube reactor was directed into various lengths (5, 15, and 45 cm) of 40 mm ID quartz tubing, modeled as a plug flow reactor (PFR) to allow for additional reaction at known flow residence times. The temperature uniformity of the measurement plane was verified by traversing a thermocouple across the exit plane of the PFR. The laser probe volume was situated 2 mm immediately after the exit of the PFR – defining the absorption pathlength.

3.2.2 Extractive Probe Sampling System

The probe measurements were performed using a 4 mm ID copper tube surrounded by a stainless steel coannular water cooling jacket. The sample is then drawn through an ice-cooled water trap and into a CO NDIR analyzer utilizing gas filter correlation technique. The sampling flowrate was maintained at approximately 1 SLM and the sample pressure was maintained constant near ambient. The instrument was calibrated using bottled gases. Efforts at improving

the performance of extractive probes required the use of second extractive sampling system. Figure 3.1 shows the arrangement of the aerodynamic quench extractive probe system. Two aerodynamic quench probe designs were tested. One was similar to the one reported by Schoenung and Hanson (1984), the second one was similar to the aerodynamic quench probe described by Colket *et al.* (1982). A series of valves and vacuum pumps allows the probe suction pressure to vary while maintaining the sample pressure constant at 50 torr. A fraction of the sampled gas passes through an ice-cooled water trap and then to a NDIR analyzer. An electronic pressure transducer monitors the probe pressure, while a precision bourdon vacuum gage monitors the sample pressure in the NDIR analyzer.

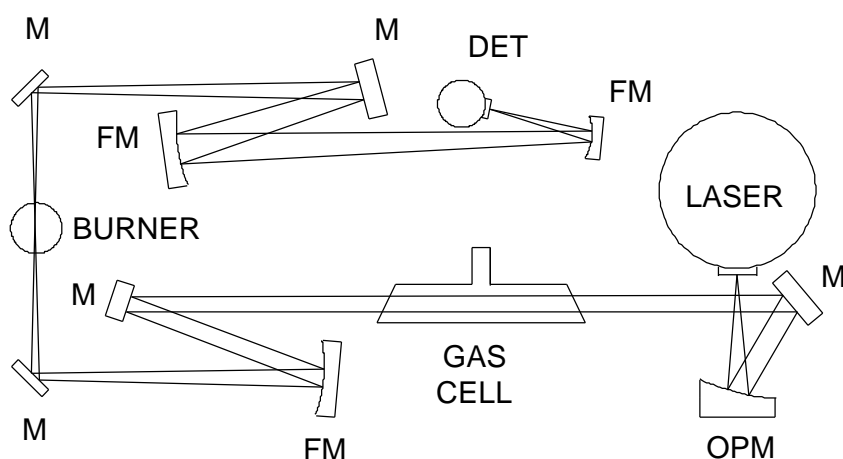


Figure 3.2: Schematic of the optical arrangement of the TDL absorption spectroscopy system. Symbol definitions: M = Mirror, OPM = Off-axis Parabolic Mirror, FM = Focusing Mirror. An optical chopper (not shown) is placed in the beam path before the gas cell for direct absorption measurements. Additional mirrors and a HeNe laser used for alignment of the IR beam are also not shown for simplicity.

3.2.3 Optics and Instrumentation Arrangement

Figure 3.2 shows the optical layout of the in-situ CO diagnostic system. Details of the optical arrangement can be found in Chapter 2 (Nguyen *et al.*, 1993). Single-mode laser emission at about 4.8 μm from the liquid nitrogen cooled Pb-Salt diode laser is collimated using an off-axis parabolic mirror. A cryogenic temperature controller regulates the diode laser temperature to within ± 1 mK. The collimated light is directed and focused through the measurement zone using mirrors. A liquid nitrogen cooled InSb detector-preamplifier fitted with a 4.5 to 5.5 μm bandpass interference filter detects the transmitted beam. The detector signal is processed using 2 lock-in amplifiers allowing the detection of both the $1f$ and $2f$ harmonics simultaneously. A PC controls the lock-in amplifiers and stores the data collected through a serial interface with the lock-in amplifiers. A low-noise precision current source provides the diode laser injection current and is controlled by the analog output of the lock-in amplifier which provides a linear

ramp to scan the laser wavelength across the absorption transitions. A function generator operating at 5 kHz is capacitively coupled into the modulation input of the current source, and sinusoidally modulates the laser current for modulation spectroscopy. A second function generator imposes a secondary low frequency (400 Hz) sinusoidal modulation to average out interference fringes caused by inadvertent reflections from the optical components (Sirota *et al.*, 1993). An optical chopper operating at 1.2 kHz with the lock-in amplifier set to a direct absorption mode characterizes the laser emission wavelength by comparison of the direct absorption signal of carbonyl sulfide gas (OCS) with a high resolution spectral map (Hunt *et al.*, 1984).

3.2.4 Experimental Technique

3.2.4.1 Modulation Spectroscopy

The use of tunable diode laser (TDL) absorption spectroscopy as a non-intrusive, in-situ diagnostic technique is attractive due to the inherent quantitiveness and high sensitivity of the technique. Varghese and Hanson (1980, 1981) have provided accurate spectroscopic linestrength and linewidth data for CO in CH₄-Air flames. Schoenung and Hanson (1981) showed that TDL [CO] measurements above a laminar CH₄-Air flat-flame differed from extractive probe measurements. Miller *et al.* (1991) showed that CO concentration and temperature could both be simultaneously measured using TDL spectroscopy in CH₄-Air diffusion flames. Nguyen *et al.* (1993) used TDL spectroscopy to measure the CO temperature and concentration in a Bunsen flame using computer tomographic reconstruction. A brief description of the technique will be given, since the use of TDL spectroscopy is mature, details can be found in the above references.

TDL absorption spectroscopy is a line-of-sight technique, where the laser emission intensity transmitted through an absorption sample (a flame or a gas cell) is monitored as a function of wavelength. The absorption spectrum is a function of: (1) the concentration of absorbing molecules, (2) the temperature, (3) the pressure, (4) the collider molecules (a weak function), and (5) the pathlength. Using Beer's law, the concentration is determined from knowledge of the remaining parameters.

The detection of ppm levels of CO using absorption spectroscopy is aided by use of modulation spectroscopy to increase the detection sensitivity, allowing the detection of absorbances as small as 10^{-6} over pathlengths of tens of meters (Silver, 1992). The minimum detectable absorbances in this study however, were of the order 10^{-3} . Modulation spectroscopy involves modulating the mean laser wavelength (at amplitudes on the order of the absorption feature width) at a frequency f . As the mean wavelength is tuned across the absorption feature, harmonics of the absorption feature appear at $1f$, $2f$, $3f$, etc. Each harmonic approximates the derivative of the absorption lineshape, hence it is often referenced to as derivative spectroscopy (Reid and Labrie, 1981). Any harmonic can be used for detection, however, Silver (1992) argues that optimal signals are generated at $2f$.

3.2.4.2 Laser Calibration Technique

A disadvantage of modulation spectroscopy is that the generated harmonic signals are proportional to the incident laser power on the detector. This power can change as a function of background radiation, thermally induced beam steering, dust in the beam path, etc. A way to overcome the dependency of the signal to the incident power is to normalize the $2f$ signal with

other harmonics as suggested by Cassidy and Reid (1982). By dividing the $2f$ signal by the $1f$ signal, the $2f$ response is directly calibrated using a known concentration of CO at a reference pathlength, pressure, and temperature. The CO concentration in the measurement zone is calculated by scaling the calibration sample $2f$ response with the vibrational-rotational populations of CO at different temperatures, and also by accounting for the change in the absorption lineshape as a function of pressure and temperature. The calibration at ambient temperatures was provided by flowing $100 \text{ ppm} \pm 10 \text{ ppm}$ CO in N_2 calibration gas through the reactor and measuring the [CO] at the exit plane of the PFR. The dependence of CO vibrational-rotational populations as a function of temperature is readily predicted following Varghese and Hanson (1980). The lineshape and linewidth of CO in hot CH_4 combustion products are calculated using a Voigt profile to account for Doppler and collisional broadening based on the collisional width measurements provided by Varghese and Hanson (1981). A Gallatry profile was unnecessary.

3.2.4.3 Selection of Transitions

The P(19) and P(21) $\nu = 1 \leftarrow 0$ transitions were selected for measurement due to: (1) their insensitivity to temperature in the 1500 to 2000 K range, (2) the lack of interference by H_2O transitions, and (3), their accessibility with the current laser. The P(19) transition at 2064.397 cm^{-1} (4.844 mm) and P(21) transition at 2055.401 cm^{-1} (4.865 mm) were verified in a gas cell using 100 ppm CO at ambient temperature. A third transition, the vibrationally excited P(13) $\nu = 2 \leftarrow 1$ at 2064.584 cm^{-1} was used in conjunction with the P(19) for two-line thermometry. Due to the monolithic nature of Pb-salt diode lasers, they are extremely prone to discontinuous jumps in the emission frequency (modehops) which prevent most transitions from being accessed. A

large amount of experimental time involves carefully tuning the laser to the desired transition without encountering a modehop. Diode laser designs that incorporate an external-cavity have been shown to be continuously tunable over broad spectral without modehops. Appendix F describes the measurement of O₂ in an absorption cell using an external-cavity near-IR diode laser. Currently, however, external cavity Pb-salt diode lasers are not available. The $2f$ absorption spectra were typically obtained over 20 second scans spanning an approximate 0.3 cm⁻¹ spectral window. The integration time of the lock-in amplifier was set at 300 ms to average out the millisecond (kHz) fluctuations due to turbulence.

3.2.4.4 Temperature Measurements

The temperature was measured using two ways: a laser based spectroscopic technique, and also using an uncoated Pt/Pt-13%Rh, 0.25 mm bead diameter thermocouple. The temperature corrections for the radiative losses on the thermocouple were calculated using a heat balance for a sphere in a radiative and convective environment similar to a technique used by Hayhurst and Kittelson (1977). The corrections ranged from 40 to 97 K depending on the temperature and flowrates. The temperature of the thermocouple was verified by comparison with the temperature obtained using CO line-pair thermometry as demonstrated by Nguyen *et al.* (1993). The vibrationally excited P(13) $\nu = 2 \leftarrow 1$ and the P(19) $\nu = 1 \leftarrow 0$ transitions were used to determine the Boltzmann vibration-rotation temperature based on the ratio of the populations of the two transitions. The populations are proportional to the $2f$ spectrum peak values normalized by the corresponding $1f$ signal. The temperatures obtained using the 2-line thermometry agreed well with the radiation corrected thermocouple temperatures. The uncertainty in the temperature measurements was calculated to be approximately ± 34 K. The uncertainty stems mainly from

laser/detector and instrumentation signal to noise considerations and the uncertainties associated with the calculated lineshape function.

3.3 Modeling of Chemical Kinetics

Modeling of the reactor is performed using computer codes based on the CHEMKIN formalism developed by Kee *et al.* (1992). A detailed reaction mechanism described by Miller and Bowman (1989) consisting of 55 species, and 256 reactions is used. The model uses highly simplified fluid mechanics using perfectly-stirred reactor and plug-flow reactor modeling approaches. Such models have been used successfully in a variety of other applications by Lutz (1992), and Nicol *et al.* (1992).

Because of the turbulent and recirculative nature of the flow, the sudden expansion stabilized flame in the 65 mm chamber is modeled as a steady-state perfectly stirred reactor, (PSR), with the volume, flowrate, and exit temperature dictating the residence time (Nicol *et al.*, 1992). Values for the PSR residence time vary from 22 to 30 ms, depending on equivalence ratio. A heat loss parameter is adjusted until the chamber exit temperature agrees with the measured exit temperature. With no further adjustments, the [CO] output of the PSR predicted by the model agrees with the laser measurement. The exit temperature and species concentrations from the PSR model are then used as inputs to the PFR model.

The flow in the 40 mm diameter quartz tube is modeled as a plug flow reactor (PFR). The plug flow assumption is supported by the fact that a flow velocity of approximately 22 m/s at 1800 K yields Reynolds numbers near 3000. This suggests that the flow properties are radially homogeneous due to turbulent mixing, and neglects axial diffusion of species. Furthermore,

measurements of the temperature in the tube as a function of radius show a uniform ‘top hat’ profile. The PFR axial temperature profile in the model is dictated by measurements.

3.4 Results

3.4.1 TDL Measurements and Modeling at Various Residence Times

Figures 3.3 through 3.5 show in detail the TDL and probe measurements for each PFR length.

Figure 3.3 shows the CO concentration measured at the exit of the 5 cm PFR (approximate residence time of 2 ms) using both the TDL apparatus and the extractive probe. The CO predicted by the model and by equilibrium calculations as well as the corresponding temperatures at different equivalence ratios are also shown. The uncertainty in the temperature measurements

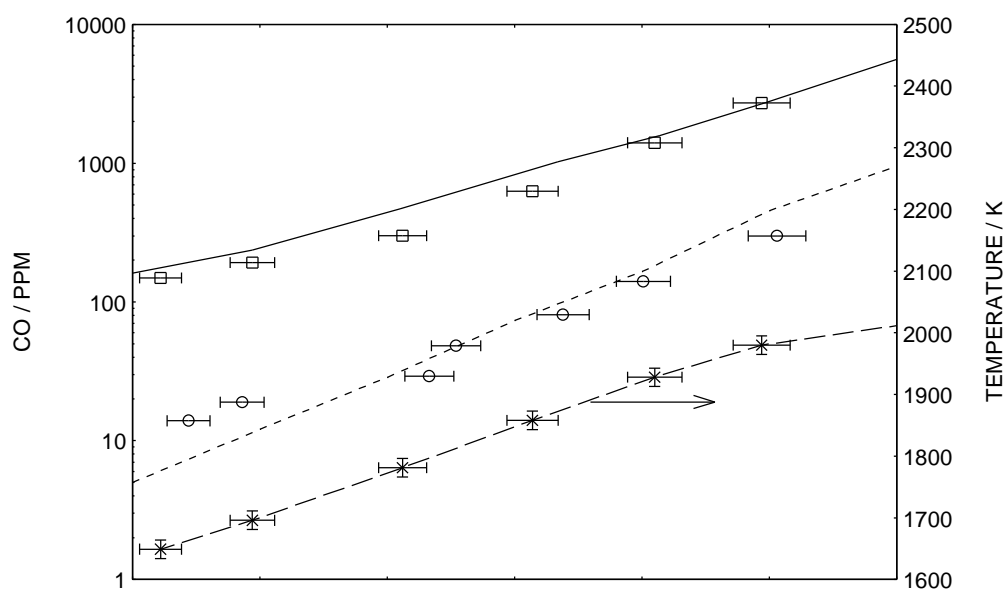


Figure 3.3: Comparison of TDL and probe measured CO values with model and equilibrium predicted values for the 5 cm PFR with an approximate residence time of 2 ms. The solid curve represents the model, the squares represent the TDL measurements, the circles represent the probe measurements and the dotted curve represent the equilibrium values. The dashed curve with the crosses represent the measured temperatures.

has two components: errors inherent in the thermocouple and the laser based two-line thermometry, and errors in knowing the corresponding equivalence ratios. The error bars in the [CO] measurements are primarily caused by the uncertainty in the flow rates (2.5%) which translate to an uncertainty in the equivalence ratio, hence the error bars are horizontal. The error introduced by the uncertainty in the calibration gas (10%) and signal-to-noise considerations are virtually imperceptible on the log scale, thus the vertical error bars are omitted. Figure 3.3 also indicates that the probe measurements of [CO] are about 10 times less than the TDL measurements. The agreement between the equilibrium and probe values are fortuitous at this point, as we will see that at other PFR positions that there is disagreement. The discrepancy between the TDL and probe measured values, we believe, results from the conversion of CO to CO₂ inside the probe through the elementary reaction, $\text{CO} + \text{OH} = \text{CO}_2 + \text{H}$, as suggested by Malte and Kramlich (1980). Lyon *et al.* (1985) also suggest that the above reaction is dominant in the oxidation of CO at ppm concentrations based on sensitivity analysis calculations. Calculations using a PFR with the measured temperature profile, operating at 1 atm pressure with an equivalence ratio of 0.85 indicate a characteristic [CO] relaxation time of approximately 30 ms. With this in mind, we expect a smaller discrepancy for the longer PFR residence times.

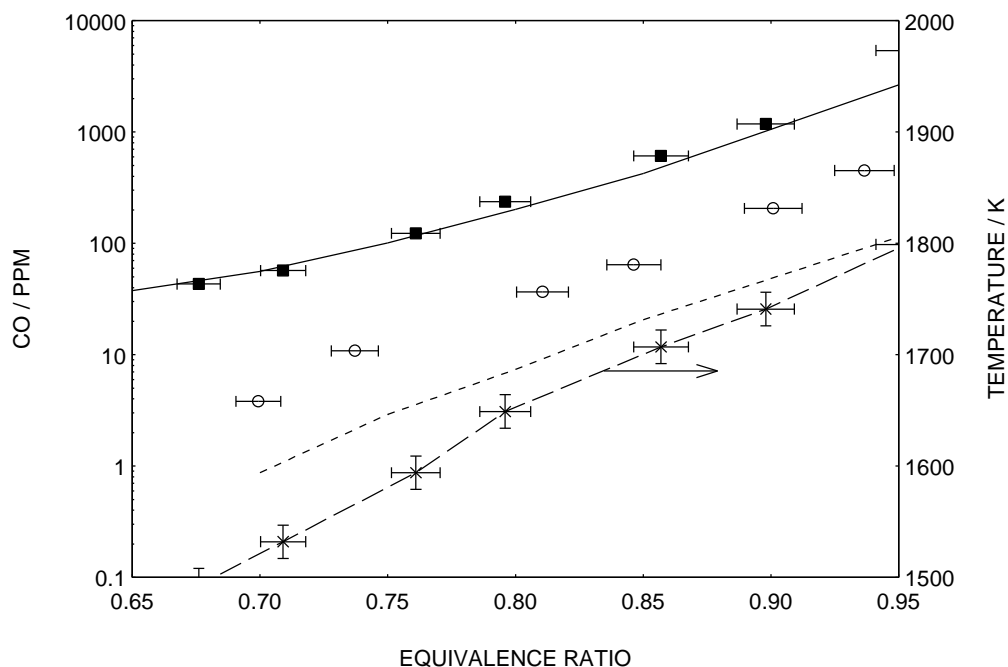


Figure 3.4: Comparison of TDL and probe measured CO values with model and equilibrium predicted values for the 15 cm PFR with an approximate residence time of 6 ms. The corresponding measured temperatures are also shown. The symbols from Fig. 3.3 are maintained for consistency.

Figure 3.4 uses the same symbols as Fig. 3.3, but shows the [CO] at the exit of the 15 cm PFR (approximate residence time of 6 ms). The discrepancy between the probe and TDL measurements is less than at the 5 cm PFR. The equilibrium predicted [CO] does not agree with either the probe or the TDL values. Figure 3.5 also uses the above symbols, but shows the [CO] at the exit of the 45 cm PFR (approximate residence time of 19 ms). For the 45 cm long PFR case, the TDL measurements were limited by the minimum [CO] detectability of approximately 40 ppm. The discrepancy between probe and TDL measurements continues to decrease and come much closer to agreement than the previous two cases. Again, equilibrium fails to agree with either probe or TDL measurements. Probe and TDL based measurements of [CO] for a fuel-rich equivalence ratio of 1.08 agree with a value of 30,000 ppm. As suggested by Malte and

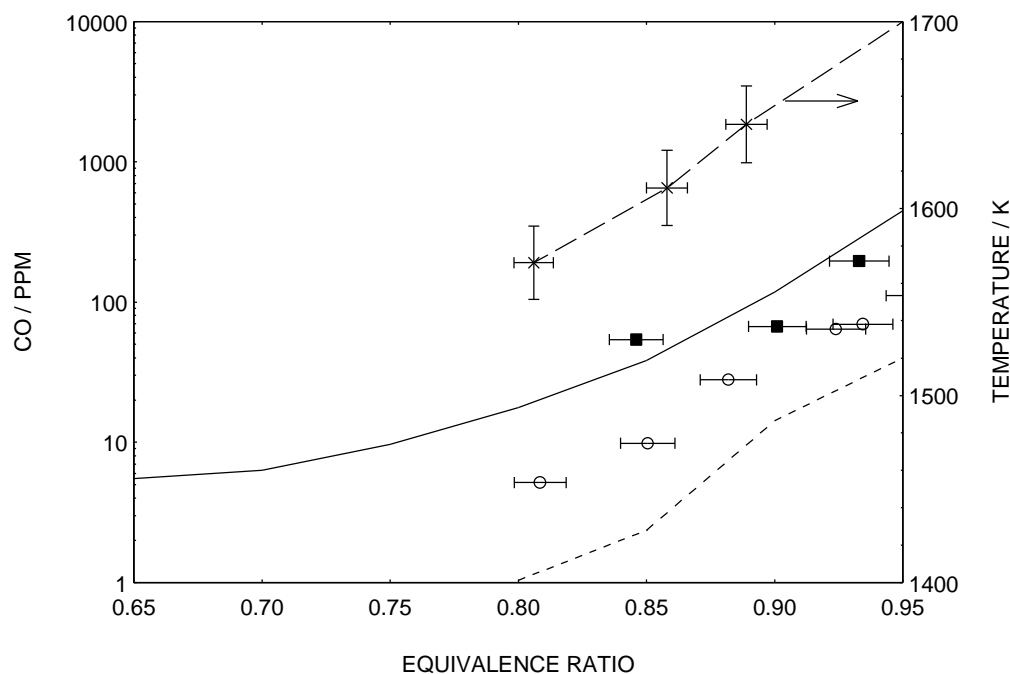


Figure 3.5: Comparison of TDL and probe measured CO values with model and equilibrium predicted values for the 45 cm PFR with an approximate residence time of 20 ms. The corresponding measured temperatures are also shown. The symbols from Fig. 3.3 are maintained for consistency.

Kramlich (1980) and by Yetter and Dryer (1992), at fuel-rich equivalence ratios, the relative abundance of unburned HC's consumes the available OH pool, and consequently inhibits the conversion of CO to CO₂.

3.4.2 Aerodynamic Quench Probe Measurements

In an effort to improve the performance of the suction probes, measurements were performed at various increased suction back pressures using several aerodynamic quench probe designs. Colket *et al.* (1982) calculated that using an aerodynamic quench probe may reduce the amount of CO to CO₂ conversion occurring in the probe. We measured [CO] using various probes at the exit of the 5 cm PFR at an equivalence ratio of 0.85 for various suction back pressures ranging from 70 torr (0.092 atm) to 750 torr (0.987 atm). Three different probes were used, the first was the water cooled straight 4 mm ID copper tube probe used in the previous measurements. The second probe was similar to the one used by Schoenung and Hanson (1981), and the third was similar to the aerodynamic quench probe described by Colket *et al.* (1982). We did not see an appreciable change in [CO] as a function of suction back pressure. The [CO] values were all close to 310 ppm and appear to be independent of suction pressure. The fact that all three probes give about the same result independent of suction pressure implies that we were unable to obtain an aerodynamic quench of CO using the present designs. Furthermore, we interpret this to mean that the cooling rates of all three probes are approximately equal. Calculations using the PFR model with a cooling rate of 10^8 K/s showed that CO could indeed be frozen or quenched as suggested by Colket *et al.* (1982). Whereas rates on the order of 10^5 K/s had a minor effect on quenching the hot super-equilibrium CO.

3.4.3 Extractive Probe Model

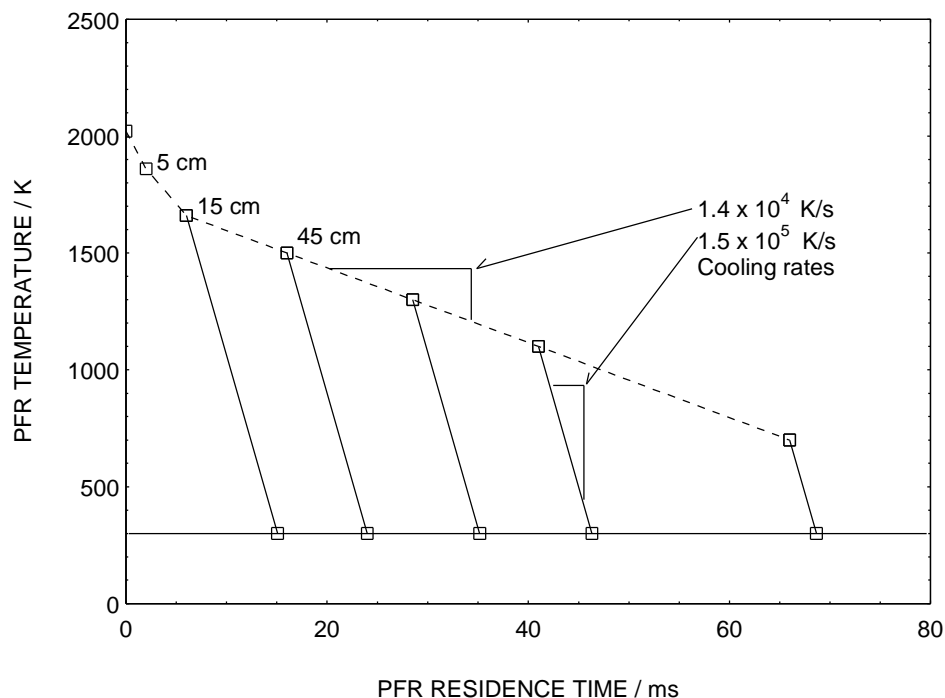


Figure 3.6: The temperature profiles used to model the reactor and sampling probes as a PFR for the equivalence ratio of 0.85. Solid lines represent probe temperatures and dotted lines represent the reactor temperatures.

We are interested in estimating the conditions at which the probe sampling of hot CO is valid.

The sampling of hot CO using an extractive probe is here modeled as a PFR with a prescribed cooling rate. The cooling rate is determined by

adjustment until agreement was reached between the probe and TDL [CO] values for the 15 cm PFR at an equivalence ratio of 0.85. This rate was found to be 1.5×10^5 K/s and assumed to remain constant for subsequent calculations based on the fact that measurements using all three probes produced the same [CO] values. Figure 3.6 shows the temperature profiles used in modeling the quartz tube and probe as a single PFR. The steep temperature ramps indicate the probe sampling temperature profiles for the various axial PFR locations. Since the maximum PFR length used was 45 cm, the temperatures at longer PFR locations are modeled using the cooling rate of 1.6×10^4 K/s based on the measured temperatures at the 15 cm and 45 cm PFR

locations. The modeled probe inlet temperatures range from 1660 K (at 6 ms) to 700 K (at 73 ms). Figure 3.7 shows the calculated amount of CO reacted in the probe as a function of the probe inlet temperature shown as an error factor defined as: $[\text{CO}]_{\text{actual}}/[\text{CO}]_{\text{probe}}$. As Fig. 3.7 indicates, probe sampling of [CO] is increasingly inaccurate at temperatures greater than 1000 K.

3.5 Conclusions

We have performed a systematic measurement of [CO] in hot combustion products using laser based and extractive probe methods. We conclude the following:

- (1) Extractive sampling probes underestimate the [CO] by as much as a factor of 10.

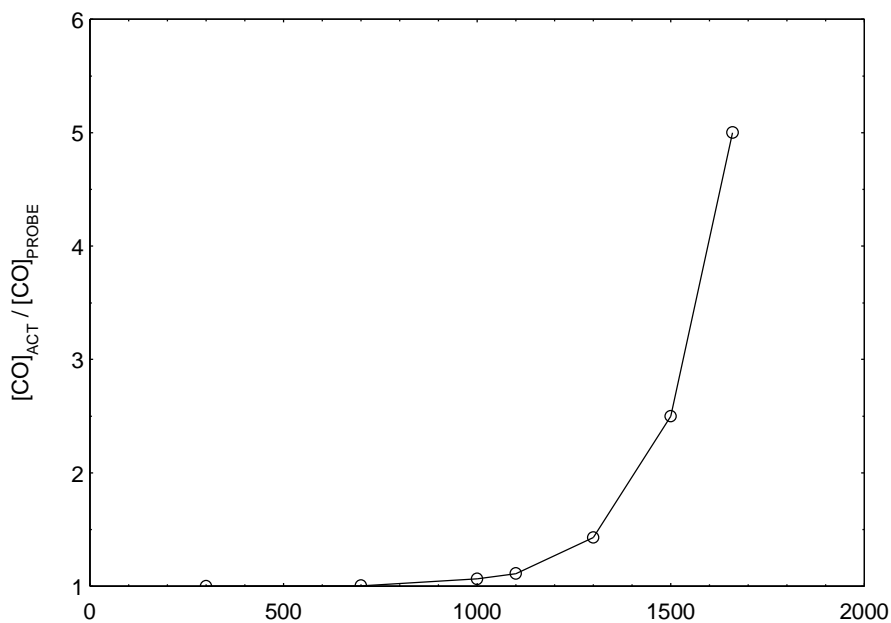


Figure 3.7: The probe sampling error defined as $[\text{CO}]_{\text{act}}/[\text{CO}]_{\text{probe}}$ as a function of inlet gas temperature calculated using the PFR model with the temperature profile shown in Fig. 3.6.

- (2) In an effort to improve the performance of extractive sampling probes, we investigated 3 different types and found no improvement.
- (3) A numerical model of the combustion using PSR and PFR approaches predicts [CO] values in satisfactory agreement with the laser based measurements.
- (4) An extension of the PFR model to the probe indicates that extractive probe sampling of [CO] is increasingly inaccurate at temperatures above 1000 K.

Chapter 4

Laser Measurements of Temperature,

The Major Species,

OH, and NO in a Methane-Air Bunsen Flame

4.0 Chapter Overview

We have obtained non-intrusive measurements of the temperature and major species (N_2 , O_2 , H_2 , H_2O , CO_2 , CO , CH_4), OH, and NO in an atmospheric pressure, laminar methane-air Bunsen flame using a combination of Raman-Rayleigh scattering, and laser induced fluorescence. Three radial profiles were measured at three axial locations for an equivalence ratio of 1.38. Three axial profile measurements along the centerline of the flame, for three equivalence ratios of 1.38, 1.52, and 1.70 were also obtained. The measurements indicate that the inner unburnt fuel-air mixture experiences significant amounts of preheating as it travels up into the conical flame zone surrounding it. Consequently, the centerline axial temperatures were

typically 100 K to 150 K higher than predicted by adiabatic equilibrium for reactants at an initial temperature of 300 K. Because the amount of preheating increases with the equivalence ratio (due to the increased inner flame height), the maximum temperatures (2000 K) in a Bunsen flame were rather insensitive to the stoichiometry. In addition to providing a detailed temperature and species map of the Bunsen flame for comparison with numerical models, our measurements show that the prompt NO mechanism was responsible for the majority of the NO formed in Bunsen flames. We observed a 20% reduction of the maximum NO concentrations (80 ppm) in a Bunsen flame by increasing the equivalence ratio from 1.38 to 1.70. The reduction of the overall NO concentration corresponded essentially to a decrease in the amount of prompt NO formed at the inner fuel-rich flame zone. We also find that a using 1-dimensional premixed laminar flame model incorporating finite-rate chemistry, satisfactorily predicts properties such as the temperature, CO, OH and NO concentrations at the inner flame-zone interface. From a practical standpoint, a simple reduction in the amount of the premixed air in existing Bunsen-type burners, significantly lowers the amount of NO produced without sacrificing efficiency.

4.1 Introduction

4.1.1 Motivation

Natural gas, predominantly composed of methane, is an abundant and relatively clean-burning fossil fuel. Its increasing use as the fuel of choice for power generation, industrial process heating, and residential use has been prompted by recently imposed, low-pollutant emissions standards (Correa, 1992). A large portion of the natural gas consumed in the United States is burned in an atmospheric Bunsen flame, which is characterized by an inner rich premixed flame zone, followed by an outer zone of non-premixed combustion. The Bunsen flame, invented in 1855, is referred to as an ‘atmospheric shot burner’ by the gas appliance industry and is used in a predominant number of burner designs for its inherent stability and passively reliable operation, important considerations for residential and commercial gas appliances.

The goal of developing cleaner and more efficient burners is most effectively realized with the aid of a numerical model of the combustion process, allowing manufacturers of natural gas burners to answer explorative ‘*what if?*’ questions on a computer. This approach reduces the reliance of the cut-and-try technique, which is becoming increasingly expensive and time consuming. The development of accurate numerical models of combustion, however, require a high-degree of understanding of the interaction between the complex, finite-rate chemistry and multi-dimensional fluid dynamics. The extent of this understanding is best verified through a direct comparison of the model results with experimental measurements of properties such as temperature and species concentrations. A recent example of this type of comparison that was reported by Norton *et al.* (1993) for a rectangular non-premixed methane-air flame. A goal of

this paper is to provide an accurate database for comparisons with comprehensive numerical models of laminar premixed methane-air Bunsen flames.

4.1.2 The Need for Non-Intrusive Measurements

Measurements using traditional techniques such as gas-sampling probes and thermocouples, while useful for certain applications, are limited by their intrusiveness when used in flames. Thermocouples, in reality, measure their own temperature, not the gas temperature; thus they often require corrections for radiative losses. In addition, gas sampling probes cannot measure highly reactive combustion intermediates such as the hydroxyl radical (OH), a participant in the reaction



This is one of the most important reactions in the oxidation mechanism of hydrocarbon fuels (Baulch and Drysdale, 1974; Westbrook and Dryer, 1984). In lean-premixed natural gas combustion, sampling probes can also introduce errors to the measurement of carbon monoxide (CO) in flames as previously shown by Nguyen *et al.* (1994).

4.1.3 Interest in Nitric Oxide Formation

In addition to the measurement of CO and OH, the accurate measurement of nitric oxide (NO) is of interest due to its toxicity and role in air pollutant formation (Bowman, 1992). The primary mechanisms of NO formation in natural gas combustion are the *thermal mechanism* (Zeldovich, 1946), and the *prompt mechanism* suggested by Fenimore (1972). Strictly speaking, the formation of NO from the attack of N₂ by CH-radicals present in fuel-rich hydrocarbon flames

(Miller and Bowman, 1989) should be called the *Fenimore-prompt* NO mechanism. Prompt NO can be defined more generally as the NO that is formed at a rate faster than that predicted by an equilibrium formulation of the thermal NO mechanism (Bowman, 1992). This definition of prompt NO includes: (1) the NO formed from super-equilibrium concentrations of O-atom and OH-radicals (through the reactions describing the thermal NO mechanism) (Drake *et al.*, 1990), (2) the Fenimore-prompt NO mechanism, and, (3) the NO formed via the nitrous oxide (N₂O) mechanism (Miller and Bowman, 1989).

The relative importance of these mechanisms in premixed hydrocarbon fuel flames has been investigated by Bachmeier *et al.* (1971) using probe-sampling techniques. More recent non-intrusive studies of NO in flames include work of Thorne *et al.* (1986), who examined HC-NO interactions, Drake *et al.*, (1990) who examined high-pressure lean premixed flames, Heard *et al.* (1992), who examined the radicals important in the formation of prompt-NO, and Reisel and Laurendeau (1994), who examined the NO production in high-pressure C₂H₆-N₂-O₂ flames. Non-intrusive and quantitative measurements of NO in atmospheric pressure fuel-rich Bunsen flames, however, have not been reported. In general, the prompt mechanism accounts for about 50% of the NO generated in fuel-rich premixed hydrocarbon flames (Bowman, 1992), this is also supported by the findings of Reisel and Laurendeau (1994). Thus, one question that requires address such that accurate models of NO emissions from Bunsen flames are possible is the following: what are the relative contributions of NO from the thermal and the prompt mechanism in a Bunsen flame?

4.2 Experimental Approach and Apparatus

4.2.1 Experimental Approach

Non-intrusive, optical measurements of temperature and concentration were obtained using laser Raman and Rayleigh scattering, and laser induced fluorescence (LIF). Raman and Rayleigh scattering have been previously applied with success to spatially and temporally resolved measurements of temperature and mixture fraction in turbulent non-premixed methane-air flames (Dibble *et al.*, 1987). LIF is a sensitive technique for detecting trace species such as OH and NO in the parts per million (ppm) range. Recently, Barlow and Carter (1994) have demonstrated simultaneous measurements of OH and NO in turbulent non-premixed hydrogen-air jet flames. The recent success of LIF as a quantitative technique, can be largely accredited to the continued efforts of Crosley (1989), Heard *et al.* (1991), Thoman *et al.* (1992), Drake and Ratcliffe (1993), and Paul *et al.* (1994) for measuring the electronic quenching cross-sections of OH and NO by numerous colliders. Although a recently demonstrated technique allows a direct mapping of the 2-dimensional collisional quenching of OH in low-pressure (0.5 atm) Bunsen flames (Hirano *et al.*, 1993), application of this technique for atmospheric pressure flames is difficult due to the shorter fluorescence decay times. We have applied the technique used by Carter and Barlow (1994), for the measurement of the temperature, and concentrations of the major species, OH, and NO, in a laminar, premixed, methane-air, Bunsen flame.

In particular, we have measured the temperature and concentrations of N_2 , O_2 , H_2O , CO_2 , CO , H_2 , and CH_4 using a combination of Raman and Rayleigh scattering. The use of Rayleigh scattering in conjunction with Raman scattering provides a more accurate measurement of the

temperature than Raman scattering alone. Rayleigh scattering is typically about three orders of magnitude greater than Raman scattering, providing larger signal levels for the measurement of the number density. Rayleigh scattering, however, is also a function of the different Rayleigh cross-sections of the molecules that comprise the mixture of the gases in the probe volume. Thus, the Raman measurements are needed to provide an overall Rayleigh scattering cross-section, required for determining the total number density of the gases in the probe volume. The temperature is then calculated through the perfect gas law. The measurements of the major species and temperature also serve a second purpose, they provide the necessary information for the determination of an overall collisional electronic quench rate, required for determining the absolute concentrations of OH and NO from measurements of their LIF signal.

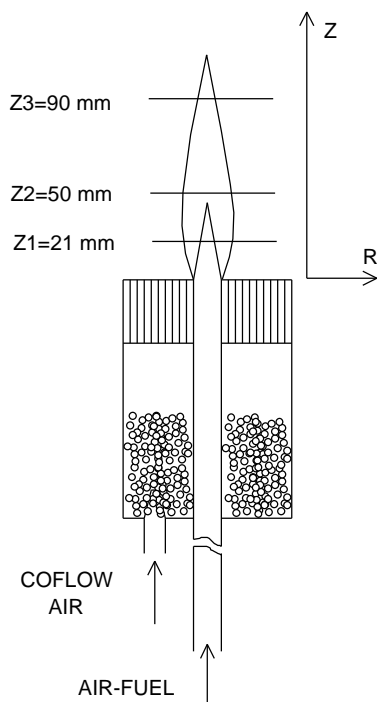


Figure 4.1: Schematic of Bunsen burner. The coflow air is homogenized by glass beads prior to entering the honeycomb flow straightener. The measurement planes for the radial traverses of flame A are shown.

The experiments were performed using the Raman-LIF apparatus in the Turbulent Diffusion Flame laboratory within the Combustion Research Facility at Sandia National Laboratory. The details of this apparatus are covered in detail by Dibble *et al.* (1987), Barlow *et al.* (1990), and Barlow and Carter (1994). Modifications and improvements to this apparatus, however, are detailed in this paper.

4.2.2 Experimental Apparatus

4.2.2.1 Burner and Flow Conditions

Figure 4.1 shows a schematic of the Bunsen burner used in the experiment and the axial locations of the measurement zones. The burner is similar to the one described by Nguyen *et al.* (1993) and consists of an 82-cm long, 17-mm diameter stainless steel tube surrounded by a 70-mm diameter honeycomb coflow matrix, which stabilizes the flame from the effects of natural buoyancy. The long length of the tube assures a condition of fully developed laminar pipe flow at the exit, defining the velocity field for numerical simulations. Pressure regulators control the flows of fuel (bottled CH_4) and dry-air through calibrated orifice plate meters, which are fitted with precision digital manometers. A static mixer then homogenizes the fuel and air flows, providing a steady premixed fuel-to-air ratio. Table 4.1 shows the experimental operating conditions of the burner.

Table 4.1: Premixed methane-air Bunsen flame operating conditions.

Flame	Traverse	Equivalence Ratio	CH ₄ (slm)	Air (slm)	Coflow (slm)	Inner Flame Height (mm)
A	Radial, Axial	1.38	0.97	6.69	82	42
B	Axial	1.52	1.05	6.63	82	55
C	Axial	1.70	1.17	6.57	82	78

4.2.2.2 Raman and Rayleigh Diagnostics

Figure 4.2 shows a schematic of the Raman-LIF apparatus. The Bunsen burner is mounted in a vertical wind tunnel, providing filtered air to minimize laser light scattered by dust particles. Stepper motors translate the wind tunnel for spatial profile measurements. For the Raman and Rayleigh scattering measurements, light from a frequency-doubled Nd:YAG laser (532-nm, 10 ns, 700 mJ) was temporally ‘stretched’ to a series of lower energy pulses with an approximate overall width of 100 ns. The longer pulse width reduces the peak laser power, eliminating the dielectric breakdown of the gases in the measurement probe volume. The pulse stretcher consists of ten mirrors and two beamsplitter-combiners. The beamsplitters divert fractions of the laser pulse to an optical delay line and subsequently recombine the multiple delayed pulses to a single, longer pulse. Using a 2-m focal length spherical lens, the light emerging from the pulse stretcher is focused to a 750- μ m beam waist at the probe volume. A small fraction of light reflected from the lens anti-reflection coating is directed to a photodiode detector for an energy measurement. The beam, after passing through the probe volume, is then reflected back into the probe volume using a collimating lens and a 90° prism; this effectively doubles the laser energy in the probe volume. The probe volume dimensions (750- μ m dia. x 750- μ m length) were defined by the beam waist diameter and the field-stop slit widths of the collection optics.

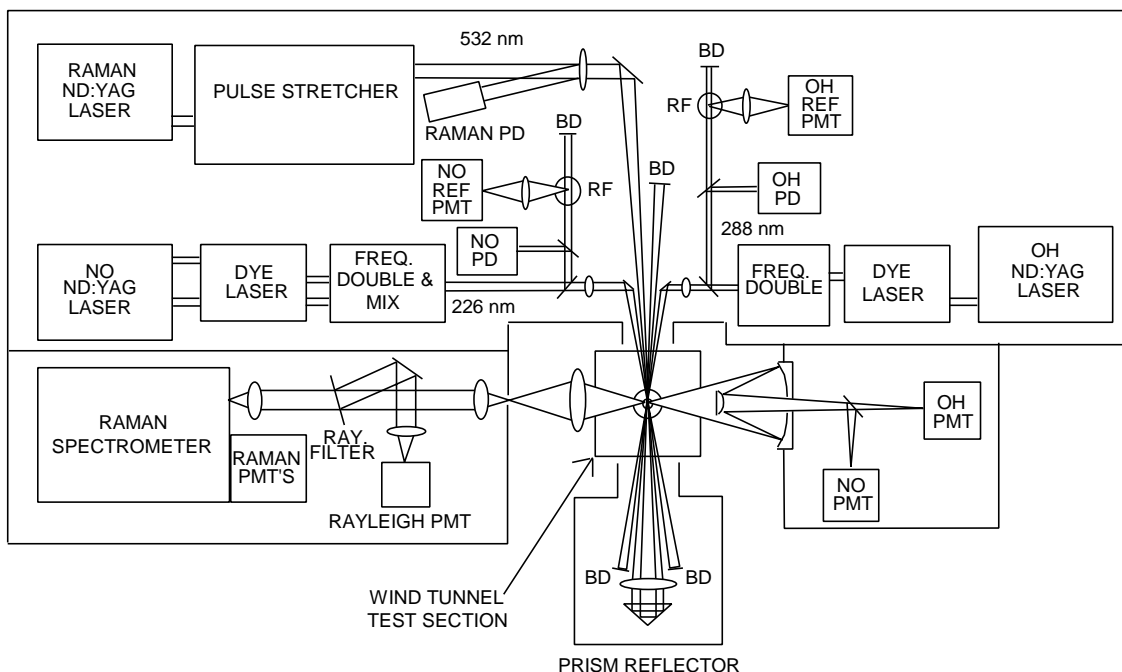


Figure 4.2: Schematic of the Raman-Rayleigh-LIF apparatus. To reduce the background scattered radiation, the laser systems are isolated from the collection systems using light-tight sheet metal enclosures. Legends: BD = beam dump, RF = reference flame, PD = photodiode, PMT = photomultiplier tube.

4.2.2.3 Raman-Rayleigh Collection Optics

The Raman and Rayleigh light scattered from the probe volume is collected with a specially designed low f-number lens (Dibble *et al.*, 1987) and is then collimated with an achromatic camera lens. After collimation, a holographic Raman edge filter reflects the Rayleigh scattered light, while transmitting the Raman scattered light. The Rayleigh scattering is then focused onto a slit placed before a photomultiplier tube (PMT). A lens images the collimated Raman beam onto the slits of a 3/4-m spectrometer fitted with an 1800 line/mm holographic grating. An achromatic 1/2-l ($420 < \lambda < 675 \text{ nm}$) waveplate mounted behind the slits of the spectrometer rotates the vertically polarized Raman beam to a horizontal plane, in effect, doubling the grating efficiency. Small mirrors direct the specific vibrational Raman bands of the major species (N_2 , O_2 , H_2 , H_2O , CO_2 , CO , and CH_4) onto seven PMTs mounted at the exit plane of the

spectrometer. A 16 channel gated charge integrator measures and digitizes with 12-bit resolution, the photocurrents from the PMTs and photodiode.

The possible Raman interferences arising from laser induced fluorescence were monitored using three additional PMTs positioned at approximately the 590-, 615-, and 640-nm exit plane positions. These spectral regions are known to have laser induced fluorescence effects from the 532-nm excitation; in particular, fluorescence emissions from the C_2 Swan bands (Faust *et al.*, 1981) onto the CO channel can give anomalously high CO measurements at certain fuel-rich locations, if not properly accounted for. This is especially important for the inner-cone flame region of a Bunsen flame, which is known to have high levels of C_2 , evident from the green-color emission from the fuel-rich inner flame zone caused by C_2 chemiluminescence (Glassman, 1987).

4.2.2.4 Laser Induced Fluorescence Diagnostics

Figure 4.2 also shows the two frequency-doubled, Nd:YAG-pumped dye laser systems used to generate the ultraviolet (UV) wavelengths required for OH and NO excitation. The UV beams were overlapped onto the Raman probe volume at a small crossing angle. The measurement probe volume was defined by a kinematically removable, 800- μm pinhole located at the waist of the Raman-Rayleigh probe volume. By adjusting the 532-nm Raman and UV laser beams through the pinhole prior to each experiment, the proper alignment of the probe volumes with respect to the collection optics was consistently obtained. Telescopes were used to adjust the beam waists such that about 90% of the UV energy passes through the 800- μm pinhole; this approach maximizes the linear fluorescence range for the desired spatial resolution ($\sim 750\text{-}\mu\text{m}$).

Digital delay pulse generators time the proper firing sequence of the three lasers. The Raman and LIF lasers are each fired 150 ns apart, eliminating the interference between the Raman and two LIF channels. Time-resolved data on the order of a fraction of a microsecond were collected at the laser pulse repetition frequency of 10 Hz, though the steady-state laminar nature of the Bunsen flame permitted averaging the single-shot data over a period of 20 seconds or 200 shots, thereby increasing the signal-to-noise ratio (SNR).

For the OH excitation, we tuned the frequency-doubled dye laser output to the $O_{12}(8)$ transition of the $A^2\Sigma^+ \rightarrow X^2\Pi(1,0)$ band of OH ($\lambda = 287.9\text{-nm}$). This transition reduces the absorption of the laser beam propagating through the flame since the $v' = 1$ band is only negligibly populated at flame temperatures. The OH and NO transitions were easily saturated with the available laser energies. Consequently, we attenuated the UV beam for the OH excitation to approximately $40\text{ }\mu\text{J/pulse}$ using neutral density filters, ensuring a linear-fluorescence regime.

For the NO excitation, we tuned the second dye-laser to the $Q_1(18)$ transition of the $A^2\Sigma^+ \rightarrow X^2\Pi(0,0)$ band of NO ($\lambda = 225.9\text{-nm}$). This wavelength was generated by frequency doubling the output of the second dye laser ($\lambda = 286.8\text{-nm}$) and mixing it with the residual 1064-nm radiation from the Nd:YAG pump laser. This transition was selected because it is well populated at flame temperatures (as well as ambient temperatures) and avoids a significant amount of interference from the nearby vibrationally hot oxygen transitions in the $B^3\Sigma^+ \rightarrow X^3\Sigma^-(2,4)$ and $(5,5)$ bands. To ensure a linear-fluorescence regime, the laser energy used for the NO excitation was attenuated to approximately $10\text{ }\mu\text{J/pulse}$.

4.2.2.5 LIF Collection Optics

The LIF signal from the probe volume was collected using a specially designed low f-number Cassegrain mirror-lens system. The reflective design eliminates the chromatic aberration present in transmissive lenses, permitting easy alignment and focusing of the different fluorescence wavelengths. A dichroic mirror separates the OH and NO fluorescence components, which are subsequently imaged onto the slits of two different PMTs fitted with color glass filters. For the detection of the OH fluorescence, we used Schott WG-295 and Hoya U-340 color glass filters, which reject the scattered radiation and collect the fluorescence from the dominant (1,1) and (0,0) bands ($295 < \lambda < 340 \text{ nm}$). The fluorescence from the (0,0) band results from the vibrational energy transfer (VET) from the $\nu' = 1$ to $\nu' = 0$ states (Smith and Crosley, 1983). For NO detection, we used Schott UG-5 color glass filters and a solarblind PMT; this combination effectively reduces scattered background radiation and permits broad band detection of the fluorescence from the NO, $\nu' = 0$ and $\nu'' = 1 - 5$ bands ($230 < \lambda < 300 \text{ nm}$). Again, the slits in front of the PMTs define the probe volume dimensions along the beam propagation axis, and are adjusted to match those of the Raman-Rayleigh system.

Beamsplitters direct portions of the OH and NO laser beams to photodiodes for energy measurements. These secondary beams were also used in recording the LIF from two reference flames burning near-stoichiometric mixtures of CH_4 and air. The fluorescence signals from the reference flames permit the monitoring of the dye laser wavelength throughout the experiment to ensure that they remain constant.

4.2.2.6 Raman Signal Calibration

In principle, Raman scattering provides a signal proportional to the number density of all the species being probed; however, the signals are also slightly modified by the following: (1) the temperature, manifested as a broadening and shift of the vibrational bands; and (2) the ‘crosstalk’ between various vibrational and rotational bands of the different species. The crosstalk arises from species with spectrally broad Raman features. The most notable case is that of H_2 ; its rotational Raman lines overlap with the vibrational Raman bands of CO_2 , O_2 , and CO . The temperature and crosstalk effects were accounted for through the calibration procedure. This involved recording the Raman signals over a wide range of known temperatures, mixtures, and concentrations. Appendix D contains details of the Raman calibration procedure.

The calibrations include cold gases, lean and rich mixtures of H_2 -air, H_2 -CO-air, and CH_4 -air flames burned above a non-premixed calibration burner. The non-premixed calibration burner (a so-called Hencken burner) was constructed from a bundle of small-diameter stainless-steel air and fuel tubes arranged in an alternating matrix; the separate fuel and air flows then burn as an array of small non-premixed flames. This burner design prevents the flashback problems associated with premixed H_2 -air flames (Dibble *et al.*, 1987) and at locations sufficiently far downstream, most of the species (with the exception of NO) are in local thermodynamic equilibrium. Thus, this burner provides a means of calculating the species concentration and temperature from the fuel-air flow rates (Barlow *et al.*, 1990).

4.2.2.7 Fluorescence Signal Calibration

For the OH and NO LIF measurements, the temperature and species

concentrations measured by the Raman and Rayleigh scattering provide the necessary information for calculating the electronic quenching corrections. We employ the methodology described by Carter and Barlow (1992) for calculating the temperature and mixture dependent quenching corrections for OH and NO (Paul, 1994; Paul *et al.*, 1994).

The conversion of fluorescence signal to number densities, in general, requires: (1) the cross sections describing electronic quenching for all excited vibrational levels with specific colliders, and (2) the cross sections for the VET between the different excited vibrational levels. Currently, however, insufficient data exists for completely describing both the electronic quenching of the $\nu' = 1$ excited state and the VET between the $\nu' = 1$ and $\nu' = 0$ states. Thus, we approximate the temperature dependence of the net collisional de-excitation rate using the quenching rates for the $\nu' = 0$ state (Paul, 1994). The effect of these assumptions on the uncertainty of the OH concentration are addressed in Section 4.3.

For the linear-fluorescence regime, the number density N (cm^{-3}) of NO and OH is related to the fluorescence signal S_f through the relation

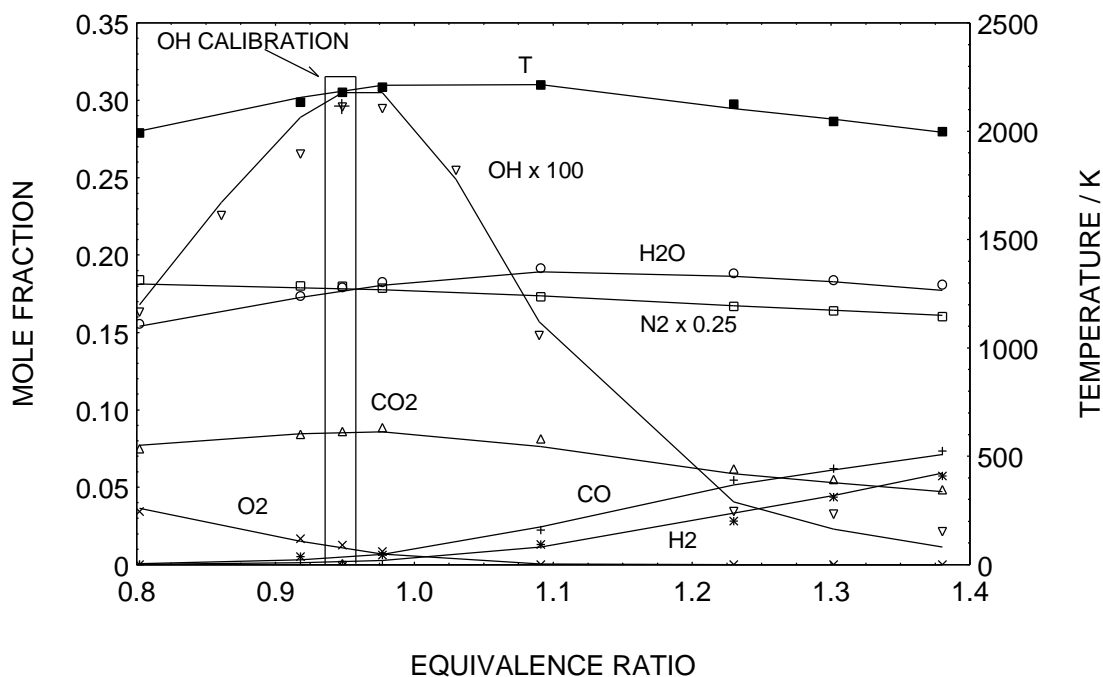
$$N = \left[\frac{N}{S_f} \right]_{\text{CAL}} \left(\frac{[F_B]_{\text{CAL}}}{F_B} \right) \left(\frac{[E_L / Q]_{\text{CAL}}}{[E_L / Q]} \right) \left\{ \frac{[g(\mathbf{n}_0)]_{\text{CAL}}}{g(\mathbf{n}_0)} \right\} S_f, \quad (4.2)$$

where F_B is the Boltzmann fractional population, E_L is the laser energy, Q is the overall collisional quench rate (s^{-1}), ν_0 is the transition frequency, $g(\nu_0)$ is the spectral overlap between the laser and the transition, and the subscript *CAL* refers to the calibration values (Carter and Barlow, 1994). The spectral overlap $g(\nu_0)$ was modeled using a Gaussian profile for the laser and a Voigt profile for absorption lineshape. The variation of the spectral overlap with

temperature, however, was found to be minimal in these measurements. Appendix E contains the FORTRAN codes that perform the LIF quenching corrections for OH and NO.

The OH LIF calibration factor (N/S_f), was obtained in a fuel-lean CH_4 -air flame ($\phi = 0.94$) using the calibration burner in a premixed mode. The equilibrium OH number density was calculated using the Raman-Rayleigh measured temperature, which was typically only 10 to 30 K less than the adiabatic equilibrium value.

For the NO calibrations, equilibrium calculations could not be used since NO is typically far below equilibrium at reasonable distances above the burner. Additionally, the concentrations encountered in the calibration flame were too small for measurement using absorption. Consequently, we obtained the calibration factor (N/S_f)_{CAL} using two fuel-lean ($\phi = 0.72$) CH_4 -



Figure

4.3: Comparison of Raman-Rayleigh-LIF measurements (data points) with adiabatic equilibrium calculations (lines) for methane-air calibration flames. The non-adiabatic equilibrium calibration points for the OH are also shown. Note that the OH scale is magnified, and the N_2 scale is reduced.

O₂-N₂ flames burned above a water cooled, sintered-bronze, flat-flame holder: one flame contains a known amount of NO that is substituted for a portion of the total N₂. The two flames are otherwise identical; the Raman-Rayleigh measurements in the flames showed that the temperatures and concentrations differ by less than a percent between the two flames. By subtracting the NO LIF signal from the two cases, a background-free calibration is obtained.

4.3 Results

4.3.1 Calibration Measurements

A series of CH₄-air flames in the calibration burner operating with equivalence ratios ranging from 0.80 to 1.38 were used to check the measurement accuracy of the Raman-Rayleigh and OH LIF calibrations. Figure 4.3 shows the experimentally measured and adiabatic equilibrium values of the temperature, N₂, O₂, H₂, H₂O, CO₂, CO, and OH concentration. Based on comparisons of the measured temperatures with those predicted by adiabatic equilibrium, and a Rayleigh scattering signal root-mean-square (RMS) variance of about 1% (resulting from uncertainties in the laser energy normalization and fluctuations in the flame itself), we estimate the uncertainty of the time-averaged temperature measurements to be ± 20 K at a temperature of 2000 K. For single-shot Raman measurements, photon shot noise is the dominant source of uncertainty (Dibble *et al.* 1987). By time averaging over 200 shots, however, this uncertainty is significantly reduced, increasing the detection limit and accuracy of the major species measured. From Fig. 4.3, all of the major species measured agreed well with the adiabatic equilibrium values over the range of equivalence ratios of 0.80 to 1.38, we estimate the time-averaged uncertainty of the major species measurements to be $\pm 3\%$ of full-scale for the different species. For the OH calibration, we used the measured temperature ($T_{MEAS} = 2180$ K, $T_{ADIA} = 2187$ K) to calculate the equilibrium OH value. With this single point calibration, the measured OH at the other equivalence ratios differs with the adiabatic equilibrium values by no more than 7% (for $\phi < 1.25$). This agreement is excellent considering the simplified treatment of the overall quenching corrections.

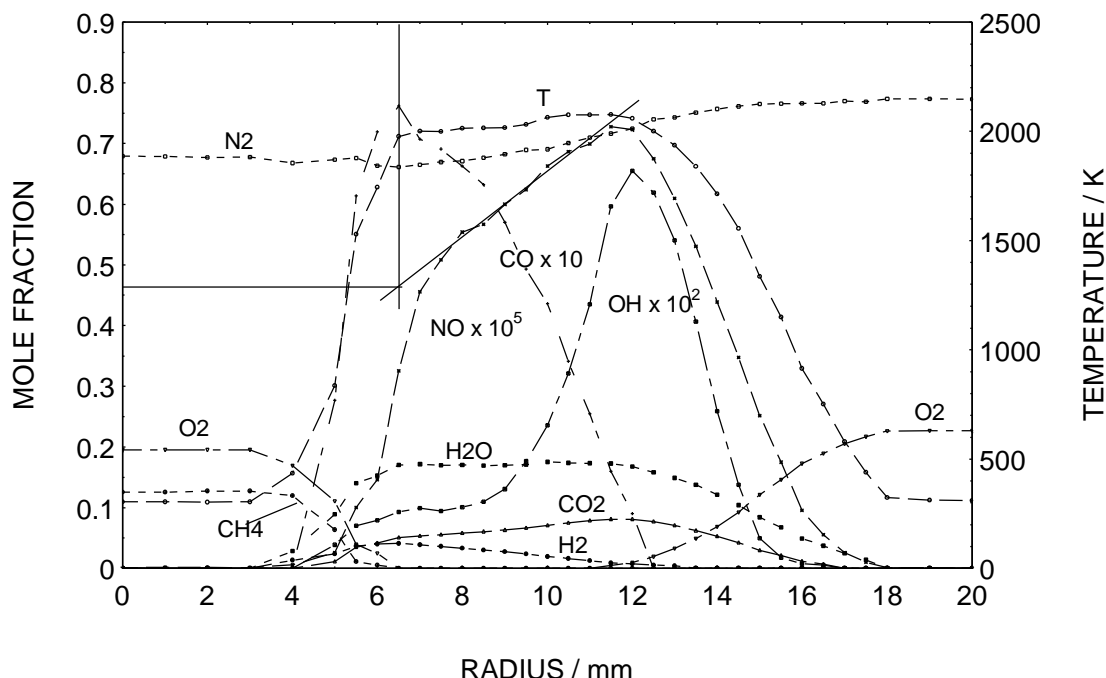


Figure 4.4: Radial profiles for flame A at the Z_1 axial location (see Fig. 4.1). The CO, OH and NO scales are magnified for clarity. For reference, a mole fraction of 1.0 on the left axis corresponds to a NO concentration of 100 ppm. The intersection of the linear NO slope with the location of the inner flame zone gives an estimate of the prompt NO.

4.3.2 Bunsen Flame Measurements

4.3.2.1 Radial Profile Measurements of Flame A

Figures 4.4 through 4.6 show the radial profiles of the Bunsen flame at different axial locations for flame A (see Table 4.1). Figure 4.4 details the radial profile across the ‘double-cone’ Bunsen flame at the Z_1 axial location (Fig. 4.1). Figure 4.4

shows that the temperature rapidly rises from the cool unburnt core to approximately 1980 K, where it plateaus between the inner and outer flame zones. As expected, the temperature reaches a maximum at the outer, stoichiometric flame zone (2077 K). The CO concentration (magnified by 10) peaks at the inner flame zone, coinciding with the oxidation of CH_4 and appearance of H_2 .

At this axial location, the measured inner-cone flame temperature is a little lower than predicted by the adiabatic equilibrium calculations ($T = 1996$ K) due to some radiative losses, but the measured CO concentration ($X_{\text{CO}} = 0.075$) is slightly higher than that predicted by equilibrium ($X_{\text{CO}} = 0.071$). The OH (magnified by 100) peaks near the stoichiometric contour defined by the intersection of the H_2 and the O_2 concentration profiles. Figure 4.4 also shows the radial NO profiles for flame A. The maximum NO concentration (72 ppm) at this axial position coincides with the location of maximum temperature. This results from the thermal NO mechanism which is important at temperatures above 2000 K (Heard *et al.*, 1992). The NO forms almost immediately beyond the inner flame zone (hence the term *prompt*), and increases linearly with radius.

4.3.2.2 Comparisons with a 1-Dimensional Flame Code

In order to estimate the contribution of NO at the fuel-rich inner flame zone to the various prompt mechanisms defined earlier in Section 4.1.3, we calculated profiles of the species of interest using an adiabatic premixed 1-dimensional free methane-air flame model with full chemical kinetics using the PREMIX and CHEMKIN codes, both developed by Kee *et al.* (1985, 1986, 1989). Williams and Fleming (1994) have successfully used this approach for the prediction of radicals in NO-doped $\text{CH}_4\text{-O}_2\text{-N}_2\text{-Ar}$ low-pressure flat-flames. For flame A, our comparisons using this code with the measured temperature, CO, and OH concentration profiles showed excellent agreement (T within 2%, OH within 5%) over the thin inner flame zone. Of particular interest is the agreement of the super-equilibrium CO peak discussed earlier: the model agrees within 1% with our measured value of $X_{\text{CO}} = 0.075$. Our calculations also show

that at the inner flame zone, there is a peak of super-equilibrium O-atom concentration and CH-radicals, located just upstream of where the temperature reaches a maximum.

4.3.2.3 Estimates of Prompt NO

Using the more general definition of the prompt NO, we estimate its contribution to the overall NO by extrapolating the linear portion of the NO curve to the inner flame front location, defined as the location where the temperature profile reaches a relatively constant value. The intersection of these lines (as shown in Fig. 4.4 and subsequent figures) gives an estimate of the prompt NO of 46 ppm. This value of prompt NO is similar to a value previously measured in propane-air flat-flames (50 ppm) operating at a similar equivalence ratio and temperature (Eberius and Just, 1973). Our 1-dimensional flame model calculation, however, over-predicts the prompt NO by 15 ppm. Drake and Blint (1991) reported that the predicted amount of NO is very sensitive to the rate constant of the reaction



considered the rate controlling step in the prompt NO pathway (Miller and Bowman, 1989). The uncertainty in this rate constant is probably the cause of the discrepancy between prediction and measurement in fuel-rich flames. The measurements and numerical predictions reported by Reisel *et al.* (1994) for laminar 1-dimensional flat $\text{C}_2\text{H}_6\text{-O}_2\text{-N}_2$ flames, also show a tendency to overpredict the NO in fuel-rich flames.

Figure 4.5 shows the radial profile for flame A at the Z_2 axial location. This location is approximately 8 mm above the tip of the inner flame cone. The levels of NO are generally increasing, and reach a maximum value of about 82 ppm with a local minimum at the centerline. The temperature profile is relatively flat in the central portion of the flame and decreases rapidly past the outer flame zone defined by the peak OH location. Also note that the maximum value of

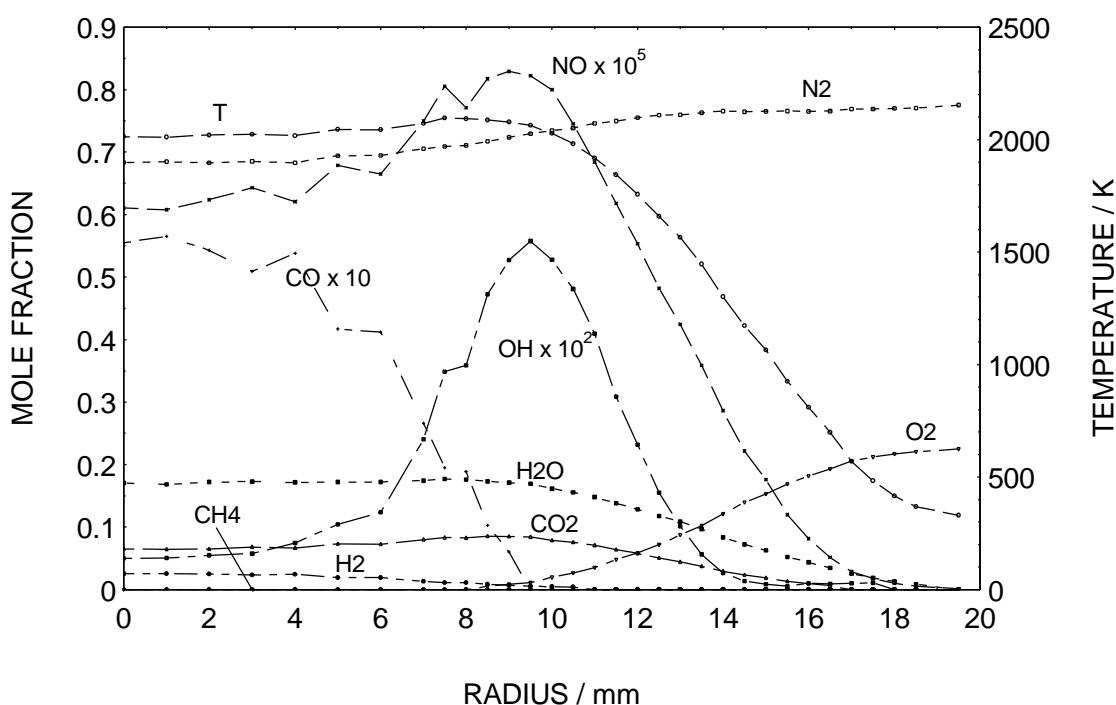


Figure 4.5: Radial profiles for flame A at the Z_2 axial location, approximately 10 mm above the inner flame cone tip. Note that the small oscillations in the concentrations are due to disturbances to the flame from air currents in the laboratory.

the temperature is almost the same as the Z_1 axial location. The CO is now greatest at the flame centerline and decreases monotonically outwards. We can also see that most of the H_2 and essentially all of the CH_4 has been consumed by this point.

Figure 4.6 shows the radial profile for flame A at the Z_3 axial location, this location is approximately 20 mm below the visible tip of the outer flame cone. The peak temperature at this axial location has decreased slightly to about 2000 K. The centerline NO value has increased from 60 ppm to about 80 ppm. Note that the centerline OH values have also steadily increased with increasing axial distance. The amount of CO at this point was barely detectable using Raman scattering.

4.3.2.4 Axial Profile Measurements of Flame A, B, and C

Figures 4.7 through 4.9 show the axial profiles along the centerline of the flames A, B, and C with varying equivalence ratio. Figure 4.7 shows the data for flame A and reveals in detail the trends observed in Figs. 4.5 and 4.6. We find that the temperature peaks just beyond the inner-cone flame tip at 2050 K and stays relatively constant at about 2000 K all the way to the visible outer cone flame tip (located at approximately 110 mm). Throughout this region, NO is steadily formed via the thermal mechanism and reaches a peak value of approximately 80 ppm at the tip of the outer cone. Beyond the flame tip, the generation of NO through the thermal mechanism stops, thus the overall NO levels decrease as a result of dilution.

Figure 4.7 also includes measurements of NO from a quartz microprobe (3 mm dia. tapered to a 0.5 mm orifice dia.) and chemiluminescent NO_x analyzer; the probe measurements were of dry NO (a water trap was used), thus we corrected the plotted NO concentration for water content using the Raman measurements. The adjusted, wet NO probe measurements agree well (within 3 ppm) with the LIF measurements. The good agreement between the two techniques reflects the accuracy of the quenching cross-sections and the calibration procedure. Although the high SNR of the NO measurements provide a single shot precision of 2% for the 80 ppm range, the fluctuations in the flame caused by ambient air currents limit the uncertainty of the time-averaged NO values to ± 4 ppm. We were able to use a suction probe for comparison in this instance due to the slow reactivity of NO with other combustion products (Bowman and Seery, 1972).

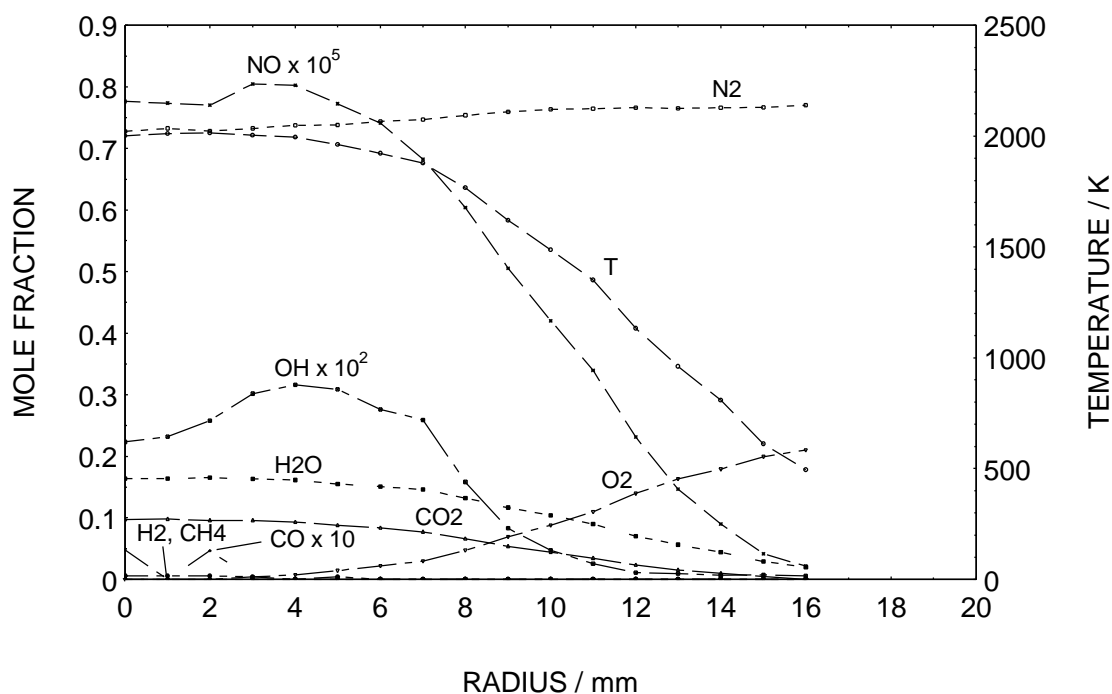


Figure 4.6: Radial profiles for flame A at the Z_3 axial location, approximately 20 mm below the outer visible flame tip. At this axial location, the methane is completely consumed and the CO is barely detectable.

Moreover, at this location, the intrusive effects of the probe on the flame properties are minimized because of the 1-dimensional nature of the flame at the centerline. The probe, however, could not be used for sampling the radial profiles shown in Figs. 4.4 through 4.6, since the flame zones were visually perturbed by the probe tip due to the steep scalar gradients found in these 2-dimensional flame regions. Access to the chemiluminescent NO_x analyzer required performing the probe measurements with the burner mounted outside of the wind tunnel, and this necessitated the use of a 300-mm long, 70-mm diameter quartz duct to isolate the flame from air currents in the laboratory. Consequently, the last few probe values diverge from the NO fluorescence data points due to the different entrainment and dilution effects existing at far-downstream axial locations. From Fig. 4.7, we extrapolate the linear portion of the NO generation curve (from 50-mm to 100-mm axial position) to the location of the inner-cone flame front; we thus estimate that the NO from prompt sources is 56 ppm. Subtracting the prompt NO from the maximum NO for flame A gives a thermal NO contribution of 23 ppm.

Figure 4.8 shows the axial profiles for flame B. Performing the same analysis on the NO profile, we find the prompt NO contribution to be about 44 ppm. The maximum NO concentration has decreased to about 68 ppm due to the slightly lower temperature. Subtracting the prompt NO from the maximum NO gives a thermal NO contribution of about 24 ppm, a value similar to that from flame A. The peak temperature for this equivalence ratio is about 1990 K, which is 100 K higher than predicted by adiabatic equilibrium. The super-adiabatic temperature is the result of the preheating (through conduction and radiation) of the unburned air-fuel mixture by the coaxial outer flame zones. Adiabatic equilibrium calculations that include the amount of measured preheating (150 K to 250 K) above 300 K result in temperatures similar to the measured temperatures. As the equivalence ratio increases, the height of the inner flame cone also increases, and the unburnt fuel-air mixture has more time for preheating. Thus

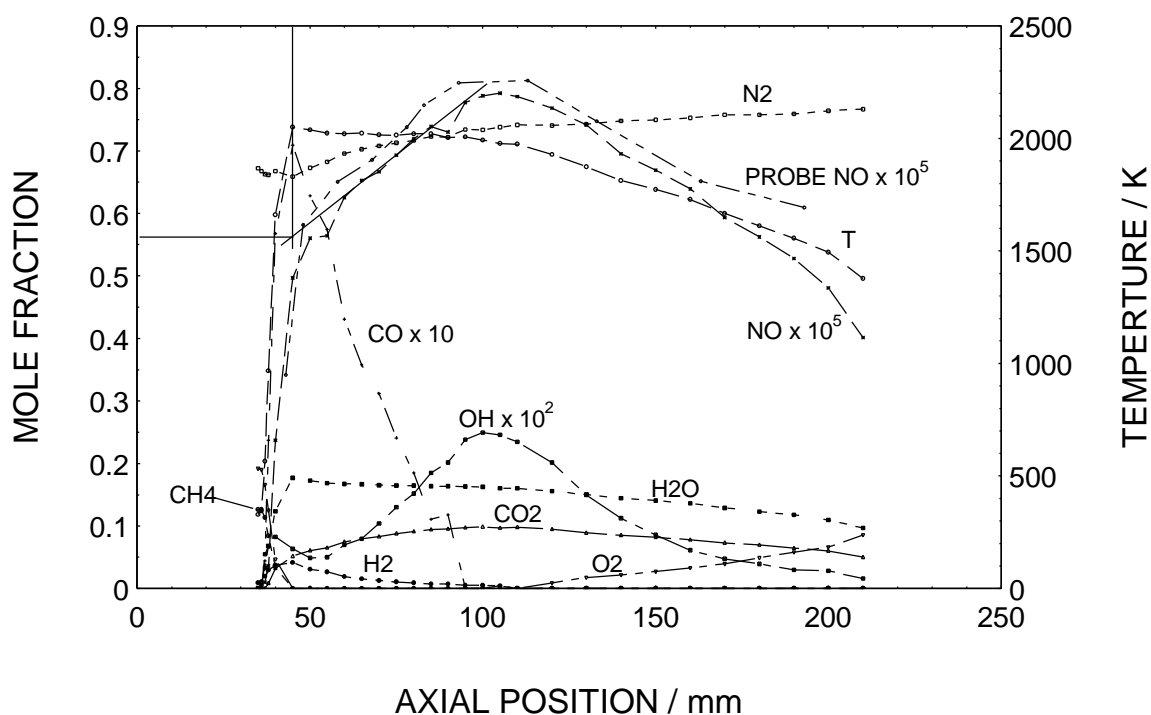


Figure 4.7: Axial profiles along the centerline of flame A. NO measurements using a quartz suction probe and chemiluminescent NO_x analyzer are also shown for comparison. The intersection of the linear NO slope with inner flame zone gives an estimate of the prompt NO at 56 ppm.

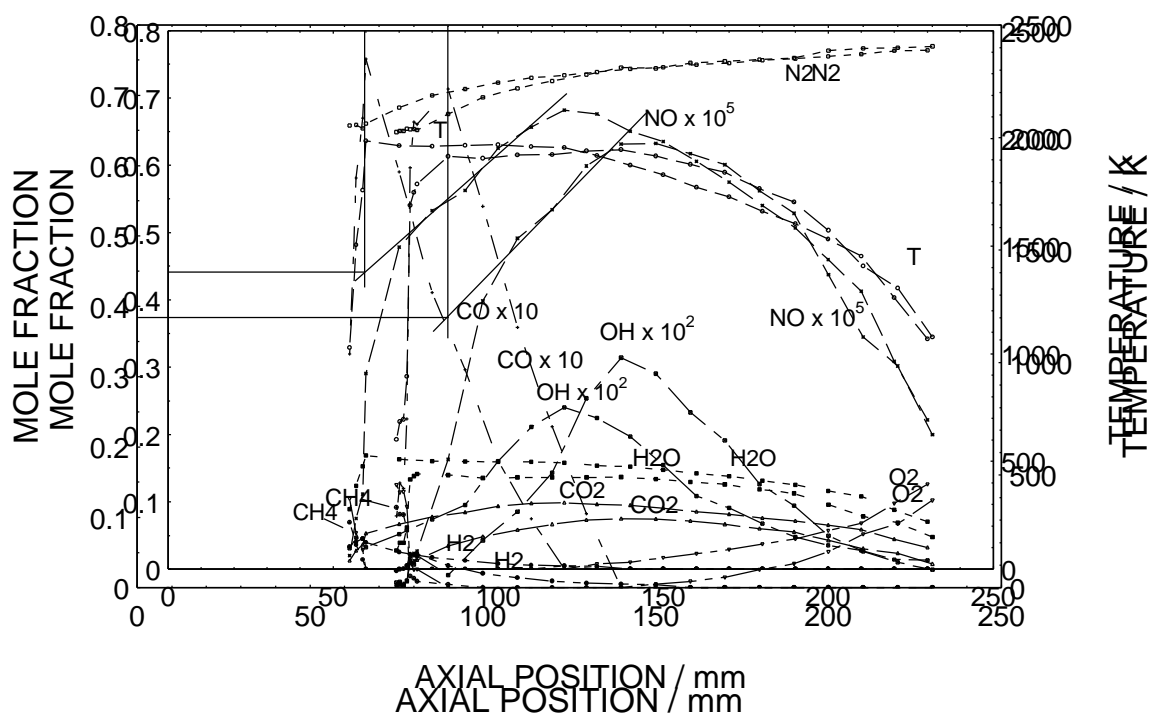


Figure 4.8: Axial profiles along the centerline of flame B. Performing an analysis similar to that on flame A above, we estimate the prompt NO for this equivalence ratio to be about 4 ppm.

the peak temperature is relatively independent of the equivalence ratio and remains at about 2000 K.

Figure 4.9 shows the axial profile of flame C. The temperature peaks at about 1900 K, this is about 140 K hotter than predicted by adiabatic equilibrium for reactants with an initial temperature of 300 K. Again, the super-adiabatic temperatures reflect the preheating of the cool unburnt fuel-air as it rises up through the coaxial outer flame. At this highly fuel-rich condition, the distinction between the inner and outer flame zones was not as visually apparent, and this is reflected in the smoother temperature profile at the inner flame zone. Performing a similar analysis on the NO curve as described above, we see that the prompt NO for this case is approximately 38 ppm. Note that the uncertainty in the prompt NO estimate is greater for this case due to the absence of a sharp rise in the NO. The peak NO value has decreased to 63

ppm. Subtracting the prompt NO from the maximum NO, we estimate the thermal NO to be 25 ppm. This value is similar to the previous two flames. Again, we see that the amount of NO formed from the prompt mechanism decreases with increasing equivalence ratio, while the amount of NO produced from the thermal mechanism stays constant at about 24 ppm and is independent of the stoichiometry. Closer inspection of the NO profile in Fig. 4.9 shows that the NO formed in the premixed portion of the flame, is much lower than the previous cases (~ 20 ppm at the vertical line). The decrease in NO from the prompt mechanism with increasing equivalence ratios (for $\phi > 1.4$) is likely the result of the reduced amounts of the available CH-radicals required for the Fenimore-prompt mechanism. This is also evident from our 1-dimensional flame calculations which show that the maximum CH-radical concentrations change from 3.7 ppm at $\phi = 1.38$, to only 0.11 ppm for the $\phi = 1.70$ case.

4.4 Conclusions

Using a combination of Raman-Rayleigh scattering and LIF in a methane-air Bunsen flame, we have simultaneously measured the temperature, OH, NO, and the major species: N_2 , O_2 , H_2 , H_2O , CO_2 , CO , CH_4 . We obtained both radial and axial profiles for various equivalence ratios ranging from 1.38 to 1.70. In addition to obtaining an accurate and detailed mapping of temperature and species in a Bunsen flame, we also found that as the equivalence ratio was increased from 1.38 to 1.70, the peak NO value decreased from 79 ppm to 63 ppm. Estimates of the prompt NO contribution were performed by extrapolating and intersecting the linear portion of the NO profiles with the location of the inner flame front. This simple procedure provided estimates of the prompt NO in Bunsen flames as a function of equivalence ratio. We found that the NO reduction resulting from an increase in the equivalence ratio was proportional to the

reduction in the amounts of NO formed through the prompt mechanism. We also find that a using 1-dimensional premixed laminar flame model incorporating finite rate chemistry, satisfactorily predicts properties such as the temperature, CO and OH concentrations at the inner flame zone interface.

We also found that the axial flame temperatures were typically 100 K to 150 K higher than that predicted by adiabatic equilibrium for reactants with an initial temperature of 300 K. We attribute this to the preheating of the unburnt fuel-air mixture as it travels upwards into the conical flame zone surrounding it. Due to this preheating, the maximum centerline temperatures (approximately 2000 K) in a Bunsen flame were rather insensitive to the stoichiometry. Since the peak flame temperatures were insensitive to an increased equivalence ratio, and assuming that the overall NO pollutant emissions are proportional to the axially measured values; we thus conclude that the NO emissions from devices using Bunsen flames can be substantially lowered without sacrificing efficiency, simply by reducing the amount of premixed air in existing burners.

Chapter 5

Two-Photon Laser Induced Fluorescence

Measurements of CO in Bunsen Flames

5.0 Chapter Overview

Simultaneous two-photon laser induced fluorescence (TPLIF) and laser Raman scattering measurements of CO in a CH₄-air Bunsen flame were obtained. These preliminary measurements provided data for the evaluation of the linearity and feasibility of TPLIF as a diagnostic technique. The measurements indicate that TPLIF shows promise as a spatially resolved and sensitive diagnostic technique. By using large laser irradiances ($I = 4 \times 10^8 \text{ Wcm}^{-2}$), the TPLIF signal was found to behave linearly with laser energy, we attribute the linear behavior to the increased effects of photo-ionization. The high rates of photo-ionization also reduce the effects of collisional quenching on the TPLIF signal, an important advantage for truly quantitative measurements. We were able to achieve a single-shot detection sensitivity of 0.1% mole fraction at flame temperatures, this is significantly better than the sensitivities achieved using Raman scattering, but is considerably less than the sensitivities normally associated with

single-photon LIF techniques. We attribute this to the decreased signal levels resulting from the high photo-ionization rates which were required for linear TPLIF.

5.1 Introduction

5.1.1 Motivation

Chapter 2 described computer tomography techniques that when used in conjunction line-of-sight (l-o-s) absorption enable the high-level CO (percent mole fraction) detection in Bunsen flames, the measurement the low-level CO (sub-percent) in the lean flame zones require a technique with improved sensitivity. Chapter 3 showed that using l-o-s absorption in conjunction with modulation techniques enabled detection sensitivities of 40 ppm at flame temperatures over a pathlength of 4-cm. As a natural extension of the LIF measurements of NO described in Chapter 4, the application of LIF to the measurement of CO described in this Chapter is aimed at the following: (1) improving the detection sensitivity that the laser Raman scattering technique lacks, and (2) providing the spatial resolution that the line-of-sight (l-o-s) absorption technique lacks.

The experimental apparatus described in Chapter 4 provided a unique opportunity to apply the simultaneous measurement of CO using the TPLIF technique and laser Raman scattering. Since the majority of the hardware required for the excitation of the CO molecule was identical to that used for the NO molecule (with the exception of the laser dyes and the collection optics filters). A goal of this preliminary study is to determine the feasibility of TPLIF as a diagnostic technique for low levels of CO in flames.

5.1.2 TPLIF as a Flame Diagnostic Technique

The use of TPLIF for the detection of CO, although not a new, has not been performed simultaneously in flames with a secondary diagnostic technique such as Raman scattering for comparison and verification. The two-photon absorption of the CO $B^1\Sigma^+ \rightarrow X^1\Sigma^+ (0,0)$ ($B-X$) transition ($\lambda = 230.1\text{-nm}$) is of interest due its accessibility with current dye laser systems using nonlinear frequency-doubling and mixing techniques. The principle concern with using a two-photon absorption process, however, is its inherent nonlinear behavior with laser energy; thus a second simultaneous measurement of the CO using Raman scattering provides a basis for comparison. In addition, the Raman measurements provide a measurement of the temperature and collider gas mixture information should the electronic quenching of the CO TPLIF signal be required for quantitative data interpretation.

The measurement of CO in flames using TPLIF was first reported by Sullivan and Crosley (1982), who used two-photons at 290-nm to excite the $A^1\Pi (v' = 3)$ state and estimated the detection limit at 0.5% mole fraction. Using the $B-X$ transition, Aldén *et al.* (1984), reported *qualitative* measurements of CO above a Bunsen flame using the TPLIF method, and estimated their detection limit at 0.2 ppm in an ambient temperature cell. More recently, Seitzman (1991), who examined the planar-imaging of CO in flames using TPLIF, argues that for large laser irradiances, the CO TPLIF signal behaves linearly with the laser energy due to the effects of multi-photon ionization. His claim is further supported by the fluorescence and photo-ionization studies of Loge *et al.* (1983) and Tjossem and Smyth (1989), who report that the CO TPLIF signal is a function of I^n , where I is the laser irradiance (W/cm^2), and n varies between 1 and 2.

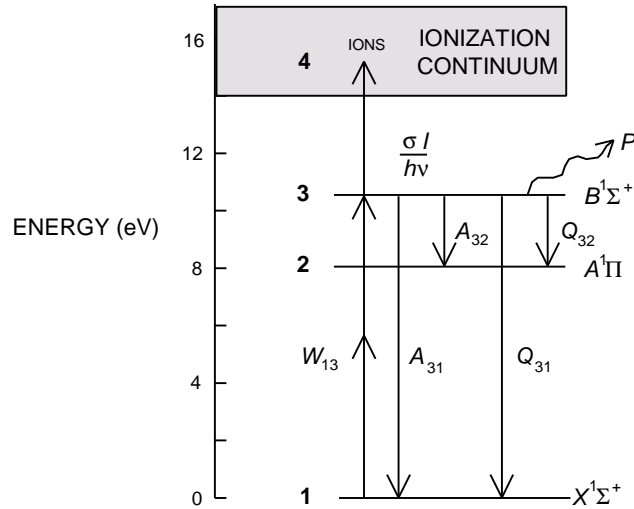


Figure 5.1: Schematic diagram of the electronic states of CO showing the different energy transfer paths. A third photon ($\lambda = 230.1$ nm) is sufficient to ionize the CO molecule (I.P. ≈ 14 eV).

A further benefit of having high rates of photo-ionization is the decreased effects of collisional electronic quenching on the TPLIF signal (Westblom *et al.*, 1990).

5.2 Experimental Approach

5.2.1 Electronic Excitation of CO

The absorption of two-photons in the ultraviolet (UV) by the CO $B-X$ band and its re-emission as a fluorescence signal in $B-A$ band (Ångström system) at visible wavelengths can be seen through a schematic diagram of the energy levels of the different electronic states of CO.

Figure 5.1 shows the electronic energy level diagram for the states of interest. Two photons ($\lambda = 230.1$ -nm) excite the CO molecules in the X state (level 1) to the B state (level 3) at a rate W_{13} (two-photon absorption rate). Assuming negligible non-stimulated upward processes, from level 3, the molecule has the following de-excitation routes: (1) radiative decay back to level 1 at a rate given by A_{31} (Einstein coefficient), (2) radiative decay (the detected fluorescence in the visible) to

the A state, denoted by level 2 at a rate given by A_{32} , (3) collisional quenching to either level 1 given by the quench rate Q_{31} or to level 2, given by Q_{32} , (4) predissociation losses given by the rate P , and (5) photo-ionization losses at a rate $SI/h\nu$ to the ionization continuum, level 4, caused by the absorption of a third photon. The fluorescence emission represented by A_{32} consists of several distinct peaks in the wavelength range from 415- to 725-nm.

5.2.2 Linear TPLIF Model

From Fig. 5.1, following the procedure outlined by Tjossem and Smyth (1989), and by Seitzman (1991), the rate of change of the population of molecules in level 3 can be written as

$$\frac{dN_3}{dt} = N_1 W_{13} - N_3 (Q + A + P) - N_3 \frac{\sigma I}{h\nu}, \quad (5.1)$$

where W_{13} is the two-photon absorption rate, and Q , A , and P are the *total* collisional quenching, radiative decay, and predissociation rates (s^{-1}), respectively. The last term $\sigma I/h\nu$ is the ionization rate to level 4, where σ is the ionization cross-section (cm^2), and h is Planck's constant and ν is the transition frequency. At the peak of the fluorescence signal, $dN_3/dt = 0$ and we can rearrange Eq. (5.1) to show

$$N_3 = \frac{N_1 W_{13}}{(Q + A + P + \sigma I / h\nu)}. \quad (5.2)$$

If the laser irradiance is high such that the ionization rate $\sigma I/h\nu$ is much greater than $(Q + A + P)$, that is,

$$\frac{\sigma I}{h\nu} \gg Q + A + P. \quad (5.3)$$

Then the upper state population can be approximated as

$$N_3 = \frac{N_1 W_{13}}{\sigma I / h\nu}. \quad (5.4)$$

The laser stimulated absorption rate W_{13} is given by

$$W_{13} = \frac{\alpha I^2}{h\nu} , \quad (5.5)$$

where α is the two-photon absorption coefficient ($\text{cm}^4 \text{W}^{-1}$). Substituting Eq. (5.5) into Eq. (5.4), results in the following expression:

$$N_3 = \frac{N_1 \alpha I}{\sigma} . \quad (5.6)$$

Equation (5.6) shows that the populations of level 1 and 3 are linearly related with laser irradiance for large values of I . The fluorescence signal can now be treated using the standard linear fluorescence methodologies described in Chapter 4 with the benefit of an absence of a dependence on the overall collisional quenching rate Q . This is very advantageous compared to the LIF of OH and NO which required the measurement of all the major species in order to perform collisional quenching corrections. Westblom *et al.* (1990) reported that the CO TPLIF signal was rather insensitive to the choice of collisional colliders and pressures for high laser irradiances. For smaller irradiances where the condition given by Eq. (5.3) does not hold, the power dependence n in I^n will be vary between 1 and 2 (Tjossem and Smith, 1989). A lower fluorescence yield, however, is a disadvantage of operating in a high photo-ionization regime; correspondingly, the detection sensitivity of linear TPLIF will be less than that of single-photon LIF (such as that of OH and NO).

Strictly speaking, the treatment described above is applied to only a single rovibronic transition. In practice, many transitions are simultaneously excited, thus, terms like the stimulated absorption rate W_{13} should include the spectral overlap integral of the laser and absorption lineshapes. This requires knowledge of the laser and the CO absorption lineshapes which would then be summed over all the possible states. This is accounted for by calibrating the TPLIF signal in a flame with conditions similar to those encountered in the measurement, similar to the calibration process used in Chapter 4. For linearly polarized excitation (used in these measurements), the Q-branch in the $B-X$ system dominates the spectrum and the O- and S-branches are absent since the $B-X$ transition has no change in the projection of the total electronic orbital angular momentum ($\Delta\Omega = 0$) (Seitzman, 1991). The rotational lines in the Q-branch are

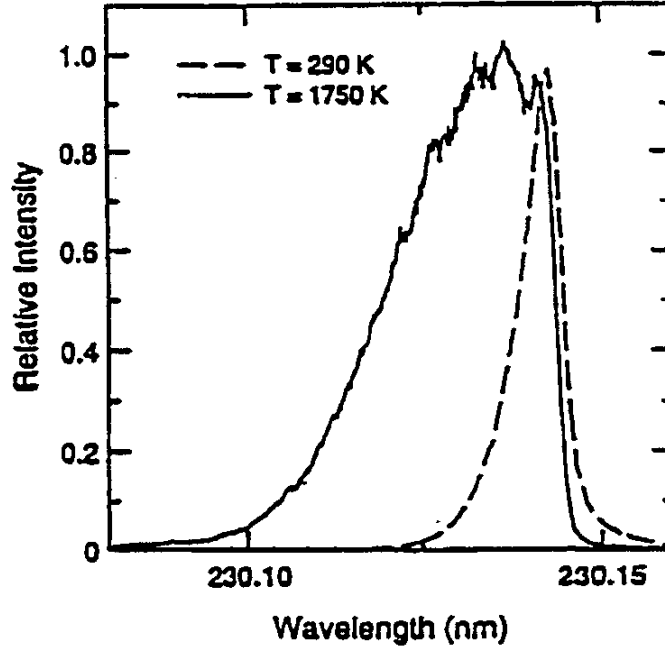


Figure 5.2: Excitation scans of the $B-X$ band at ambient and flame temperatures. The fluorescence from the $B-A$ (0,1) band, centered near 483.5-nm is plotted versus the laser excitation wavelength .

so closely spaced (due to the similar rotational constants between the two states) that the excitation spectrum of the Q-branch is essentially a sloping continuum; this can be seen in the excitation spectrum shown in Fig. 5.2. The shape of the band broadens considerably at higher temperatures due to the Boltzmann distribution of states. The excitation scan of the *B-X* band was measured at ambient temperatures (290 K) and at flame temperatures (1750 K). For the measurements in the flame, we adjust the excitation wavelength to with a spectral region that was insensitive to changes in temperature over the range of temperatures encountered in the flames measured. The laser linewidth is about 1.2 cm^{-1} and the width of the *B-X* band (at flame temperatures) is about 9.4 cm^{-1} (FWHM); thus we can treat the CO essentially as a broadband absorber. The CO TPLIF signal is then assumed to be independent of the effects of the temperature dependent rotational distribution. The vibrational population of the ground state, however, varies slightly with temperature and is accounted for using a Boltzmann vibrational distribution.

5.2.4 Calibration of TPLIF measurements

The CO TPLIF measurements were calibrated above a non-premixed calibration burner described in Chapter 4. A CH₄-air flame operating at an equivalence ratio of 1.38 was used for the calibration with adiabatic equilibrium values ($X_{CO} = 0.0751$, $T = 1995$ K). The measured CO TPLIF signal was converted to quantitative values using the following expression, adapted from Eq. (4.2),

$$N = \frac{\epsilon N}{\epsilon S_F} \frac{F_B(T_{CAL})}{F_B(T)} S_F, \quad (5.6)$$

where N is the number density in (cm⁻³), S_F is the fluorescence signal normalized by the laser irradiance, $F_B(T)$ is the vibrational Boltzmann fraction at temperature T , and the subscript CAL refers to the calibration conditions. The vibrational Boltzmann fraction is given by $F_B(T) = 1 - \exp(-h\nu_e/kT)$, where ν_e is the fundamental vibrational frequency of the CO ground-state.

5.3 Experimental

The experimental apparatus is the same as that described in Chapter 4 with the following modifications. The dye used in the NO laser was changed from rhodamine-590 to a mixture of rhodamine-590 and Kiton red in methanol in order to shift the peak of the dye laser curve to the red. The dye laser was tuned to

approximately 587-nm (50 mJ/pulse, 10 ns), this wavelength was then frequency-doubled and mixed with the residual 1064-nm Nd:YAG radiation. Approximately 1 mJ of UV energy at 230.1 nm was obtained which was subsequently attenuated to 700 $\mu\text{J/pulse}$ and focused to a 150- μm spot ($I = 4 \times 10^8 \text{ Wcm}^{-2}$) at the probe volume for operation in the photo-ionization dominated regime. Recall that laser energies of only tens of $\mu\text{J/pulse}$ was required for the linear single-photon LIF of OH and NO. The collection optics were modified by substituting the color glass filters in front of the detection PMT with an interference filter centered at 484-nm with a 10-nm bandwidth, which transmits only the fluorescence from the $B-A(0,1)$ band near 483.5-nm. Although more signal could be collected using a broadband scheme similar to that used by the NO setup, we found significant amounts of interference from the emissions of C_2 that are present in fuel-rich hydrocarbon flames when using broadband detection. Thus we opted for the reduction of the C_2 interference at the expense of signal strength. Similar interferences were also reported by Aldén *et al.* (1984).

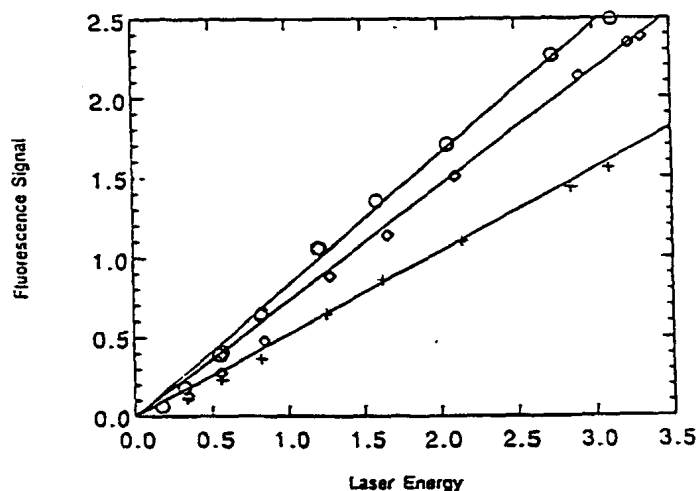


Figure 5.3: Linearity test of the CO TPLIF signal for cold CO (circles and crosses) and CO at flame temperatures (diamonds). The maximum laser energy was approximately 1 mJ/pulse.

5.4 Results

5.4.1 Linearity Tests

Figure 5.3 shows the linearity test of the CO TPLIF signal. The CO was provided by a various sources, two cold mixtures of percent levels of CO in N₂, and a fuel-rich CH₄-air calibration flame. The laser power delivered to the probe volume was varied by placing various combinations of neutral density filters in the UV beam. The CO TPLIF signal is quite linear over the range of the laser powers and becomes nonlinear at the lower irradiances. Based on the measurements in fuel-lean calibration flames, we estimate the minimum single-shot detection limit to be 1000 ppm (0.1% mole fraction) at flame temperatures. This is more sensitive than Raman scattering, but, as expected, is less sensitive than the single-photon LIF of OH and NO. With a sufficient amount of time averaging, the detection sensitivities can be improved to the 100 ppm level. For these measurements, however, we were interested in verifying the linear behavior of the TPLIF signal at percent CO concentrations rather than obtaining a high degree of detection sensitivity which may have been improved through a more optimized experimental apparatus (both collection optics and instrumentation).

5.4.2 Bunsen Flame Measurements

Figure 5.4 shows the radial profile measurements for flame B (see Table 4.1) operating at an equivalence ratio of 1.52. The excellent agreement between the Raman and the TPLIF measurements which indicates that the TPLIF was operating in a linear photo-ionization dominated regime. The good agreement also reflects the success of the calibration procedure and the validity of treating the CO *B-X* transition as spectrally broad and insensitive to variations in

temperature. The measurements disagree more at the inner flame zone. This is probably due to the effects of a spatial resolution mismatch between the Raman and TPLIF probe volumes; the TPLIF probe volume was about 150- μm in diameter and the Raman beam was about 800- μm in diameter. As expected, this effect is more pronounced at locations of steep CO concentration gradients. At the outer flame zone, Fig. 5.4 also shows the extended sensitivity that the TPLIF technique has over Raman scattering. The TPLIF measurement points curve smoothly towards zero as the concentration drops below the percent levels; the Raman measurements on the other hand, have an abrupt cutoff when the concentration is below 0.5% (an artifact of the Raman data reduction process).

Recall that in Chapter 2, the temperature profile in the double-cone region of a Bunsen flame (Fig. 2.6) was measured using l-o-s diode laser absorption in conjunction with computer

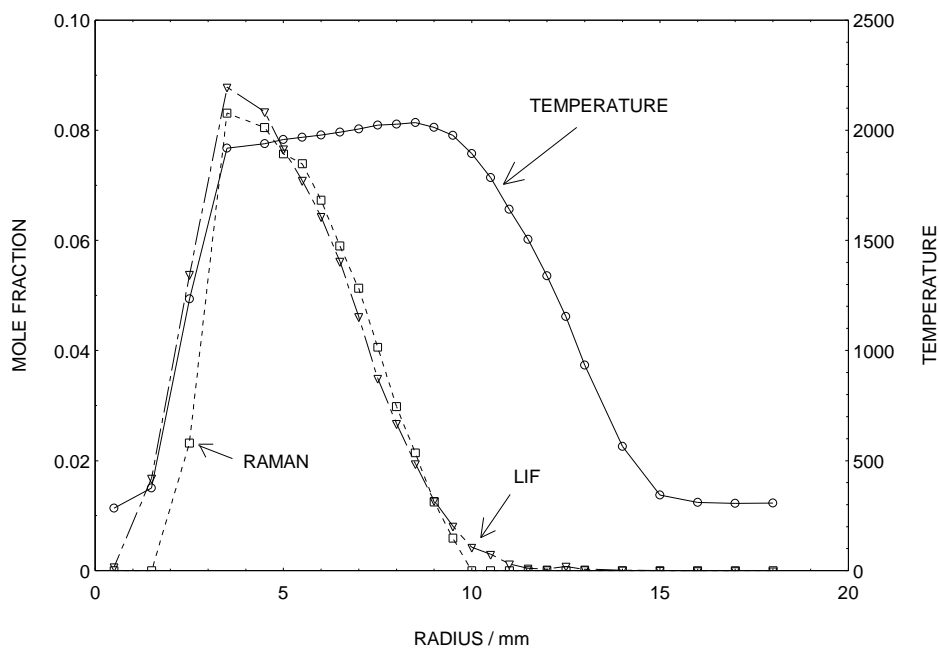


Figure 5.4: Radial profile of Bunsen flame B (see Table 4.1) at an axial location of 21 mm. The circles represent the temperature, the triangles represent the TPLIF measurements, and the squares are the Raman measurements.

tomographic (CT) reconstruction techniques. We had suspected that the temperature profile was distorted as a result of the CT reconstruction process. Now that the temperature and concentration profiles in the double-cone region of similar Bunsen flames have been measured by alternative techniques, we can see that the CT reconstruction process distorts the temperature profile by introducing an overshoot of the temperature in the inner-flame. Although the flame used in Chapter 2 is not identical to the flame in the present Chapter, they are quite similar in terms of equivalence ratios and dimensions of the inner and outer flame heights. We estimate that the temperature overshoot is on the order of 200 K. The peak value of CO concentration shown in Fig. 2.6 is also substantially less than that shown in Fig. 5.4. These comparisons indicate that great care has to be used with CT reconstruction techniques if an accurate measurement is desired. The CT results may be improved with the use of a finer sampling spacing and/or a more optimized filter function.

5.5 Conclusions

In this preliminary study, the simultaneous TPLIF and Raman measurements of CO in a CH₄-air Bunsen flames, indicate that TPLIF shows promise as a spatially resolved and sensitive diagnostic technique. By using large laser irradiances ($I = 4 \times 10^8 \text{ Wcm}^{-2}$), the TPLIF signal was found to behave linearly with laser energy, we attribute the linear behavior to the increased effects of photo-ionization. The photo-ionization also reduces the effects of collisional quenching on the TPLIF signal, an important advantage for truly quantitative measurements. Due to the closely spaced rotational structure of the CO Q-branch in the *B-X* band, CO acts essentially as a broadband absorber for laser linewidths smaller than the absorption bandwidth. Thus quantitative measurements were obtained through calibrating the TPLIF signal in a flame

with a minimum amount of data reduction; namely, convolving the laser lineshape with the many overlapping rovibronic transitions that were simultaneously excited was unnecessary. Our measurements indicate a single-shot detection sensitivity of 0.1% mole fraction at flame temperatures, this is significantly better than the sensitivities achieved using Raman scattering, but is considerably less than the sensitivities normally associated with single-photon LIF techniques. We attribute this to the decreased signal levels resulting from the high photo-ionization rates which were required for linear TPLIF. However, we feel that improved sensitivities are possible by optimizing the collection optics and instrumentation or by time averaging the single-shot measurements for steady-state measurements.

References

- Aldén, M., Wallin, S., and Wendt, W. (1984), *Applied Physics B*, **33**, 205-208.
- Arndt, R. (1965), *Applied Optics*, **36**: 8, 2522.
- Bachmeier, F., Eberius, K. H., and Just, Th. (1973), *Combust. Sci. Technol.*, **7**, 77.
- Barlow, R. S., Dibble, R. W., Chen, J. Y., and Lucht, R. P. (1990), *Combust. Flame*, **82**, 235.
- Barlow and Carter (1994), *Combust. Flame*, **97**: 261-280.
- Baulch, D.L., and Drysdale, D.D. (1974), *Combust. Flame*, **23**, 215-225.
- Born, M. and Wolf, E. (1975), "Principles of Optics", Pergamon Press, 191-196.
- Bracewell. R. N. (1978), "The Fourier Transform and its Applications", McGraw-Hill, New York.
- Bouanich, J. P. and Brodbeck, C. (1973), *J. Quant. Spectros. Rad. Trans.*, **13**, 1-7.
- Bowman, C. T. (1992), *Twenty-fourth Symposium (International) on Combustion/The Combustion Institute*, Pittsburgh, PA., 859-878.
- Bowman, C. T. and Seery, D. V. (1972), "Emissions from Continuous Combustion Systems", Plenum Press, New York, p. 123.

Carter, C. D. and Barlow, R. S. (1992), Presented at the Western States Section/The Combustion Institute - Fall Meeting at Berkeley, CA, Paper No. WSS/CI 92-47.

Carter, C. D. and Barlow, R. S. (1994), *Optics Letters*, Vol. 19, No. 4, 299-301.

Cassidy, D.T., and Reid, J., *Applied Optics* (1982), **21**: 7, 1185-1190.

Ch'en, S. Y. and Takeo, M. (1957), *Rev. Mod. Phys.*, **29**: 1, 20-73.

Colket, M. B., Chiapetta, L., Guile, R. N., Zabielski, M. F., and Seery, D. J. (1982), *Comb. Flame*, 44: 3-14.

Correa, S. M. (1992), *Journal of Propulsion and Power*, **8**: 6, 1144-1151.

Crosley, D. R. (1989), *J. Chem. Physics*, **93**, 6273.

Dasch, C. J. (1992), *Applied Optics*, **31**: 8, 1146-1152.

Dibble, R. W. (1975), "Laser Probing of Excited CO Products from Shock Wave Initiated Oxidation of Carbon Disulfide", Thesis, The Dept. of Chem. Engr., Univ. of Wisconsin, Madison, WI.

Dibble, R. W., Masri, A. R., Bilger, R. W. (1987), *Combust. Flame.*, **67**, 189-206.

Drake, M. C. and Blint, R. J. (1991), *Combust. Sci. and Tech.*, **75**, 261.

Drake, M. C., Ratcliffe, J. W., Blint, R. J., Carter, C. D., and Laurendeau, N. M. (1990), *Twenty-third Symposium (International) on Combustion/The Combustion Institute*, Pittsburgh, PA, p. 387.

Drake, M. C. and Ratcliffe, J. W. (1993), *J. Chem. Phys.*, **98** (5), 3850-3865.

Drayson, S. R. (1976), *J. Quant. Spectros. Rad. Trans.*, **16**, 611-614.

Eberius, K. H. and Just, Th. (1973), Atmospheric Pollution by Jet Engines, *AGARD Conf. Proc.*, No. 125.

Emmerman, P. J., Goulard, R., Santorro, R. J., and Semerjian, H. G. (1990), *Journal of Energy*, **4**: 2, 70-77.

Faust, W. L., Goldberg, L. S., Craig, B. B., and Weiss, R. G. (1981), *Chemical Physics Letters*, **83**, 265.

Fenimore, C. P. (1972), *Combust. Flame*, **19**, 289.

Galatry, L. (1961), *Physics Review*, **122**, 1218.

Glassman, I. (1987), *Combustion*, Academic Press Inc., Orlando, FL., p. 331.

Hayhurst, A.N., and Kittelson, D.B. (1977), *Comb. and Flame*, 28: 301-317.

Heard, D. E., Jeffries, and Crosley, D. R (1991), *Chemical Physics Letters*, Vol. 178, No. 5,6, 533-537.

Heard, D. E., Jeffries, J. B., Smith, G. P., and Crosley, D. R. (1992), *Combust. Flame*, **88**, 137-148.

Hirano, A., Ricoul, F., and Tsujishita, M. (1993), *Jpn. J. Appl. Phys.*, Vol. 32,

3300-3307.

- Howard, J. B., Williams, G. C., and Fine, D. H. (1973), *The Fourteenth Symposium (International) on Combustion*, The Combustion Institute, Pittsburgh, 975-985.
- Hughey, B. J. and Santavicca, D. A. (1982), *Combust. Sci. Tech.*, **29**, 167-190.
- Hunt, N., Foster, S.C., Johns, J.W.C., and McKellar, A.R.W. (1984), *High Resolution Spectroscopy of 16 Bands of OCS in the 1975-2140 cm⁻¹ Region for Diode Laser Calibration*, Hertzberg Institute of Astrophysics, Ottawa, Ontario, Canada K1A 0R6.
- Kee, R. J., Dixon-Lewis, G., Warnatz, J., Coltrin, M. E., and Miller, J. A. (1986), Sandia Report SAND86-8246, Sandia National Laboratories, Livermore, CA.
- Kee, R. J., Grcar, J. F., Smooke, M. D., and Miller, J. A. (1985), Sandia Report SAND85-8240, Sandia National Laboratories, Livermore, CA.
- Kee, R. J., Rupley, F. M., and Miller, J. A. (1989), Sandia Report SAND89-8009B, Sandia National Laboratories, Livermore, CA.
- Kwoh, J. S., Reed, I. S., and Truong, T. K. (1977), *IEEE Transactions on Nuclear Science*, NS-24, 1190.
- Loge, G. W., Tiee, J. J., and Wampler, F. B. (1983), *J. Chem. Phys.*, **79**: 1, 196-202.
- Lovett, L. J. and Abuaf, N. (1992), International gas turbine and aeroengine congress and exposition, ASME Conference, Cologne, Germany, Paper # 92-GT-120.

Lutz, A.E. (1992), “*Kinetic computations of NO_x emissions from reformed fuel mixtures in lean-premixed gas turbines*”, Presented at The Western States Section / The Combustion Institute.

Lyon, R.K., Hardy, J.E., and Von Holt, W. (1985), *Combustion and Flame*, 61: 79- 86.

Malte, P. C., and Kramlich, J. C. (1980), *Comb. Sci. and Tech.*, 22: 263-269.

Miller, J. A., and Bowman, C. T. (1989), *Prog. Energy Comb. Sci.*, **15**: 287-338.

Miller, J. H., Ahvazi, B., and Abraham, E. (1991), “*Tuneable Diode Laser Measurements of CO Concentration and Temperature in a Laminar Methane-Air Diffusion Flame*”, The Dept. of Chem., Geo. Wash. Univ., Washington, DC.

Mitchell, A. G. C. and Zemansky, M. W. (1971), “*Resonance Radiation and Excited Atoms, 2nd Edition*”, Cambridge Press, 158-183.

Nguyen, Q. V., Dibble, R. W., Hofmann, D., and Kampmann, S., *Ber. Bunsenges. Phys. Chem.* (1993), Vol. 97, No. 12, 1634-1642.

Nguyen, Q. V., Edgar, B. L., Dibble, R. W., and Gulati, A. (1994), presented at the *Twenty-fifth Symposium on Combustion (International)/The Combustion Institute* and to appear in *Combust. Flame*.

Nicol, D., Malte, P.C., Lai, J., Marinov, N.N., Pratt, D.T. (1992), *NO_x Behavior for Lean-Premixed and Conventional Combustion in Gas Turbine Engines*, Presented at The Western States Section / The Combustion Institute.

Norton, T. S., Smyth, K. C., Miller, J. H., and Smooke, M. D. (1993), *Combust. Sci. and Tech.*, Vol. 90, 1-34.

Ouyang, X and Varghese, P. L. (1989), *Applied Optics*, **28**: 8, 1538.

Paul, P. H. (1994), *J. Quant. Spectrosc. Radiat. Transfer*, Vol. 51, No. 3., 511- 524.

Paul, P. H., Gray, J. A., Durant Jr., J. L., Thoman Jr., J. W. (1994), *AIAA Journal*, Vol. 32, No. 8, 1670-1675.

Philippe, L. C. and Hanson, R. K. (1992), AIAA 30th Aerospace Sciences Meeting and Exhibit, Paper # AIAA 92-0139.

Rakestraw, D. *et al.* (1991), private communication, Sandia National Laboratories, CRF, Livermore, CA.

Reid, J. and Labrie, D. (1981), *Applied Physics B*, **26**, 203-210.

Reisel, J. R. and Laurendeau, N. M. (1994), *Combust. Sci. and Tech.*, Vol. 98, 137-160.

Reisel, J. R., Carter, C. D., and Laurendeau, N. M. (1994), submitted to: *8th International Symposium on Transport Phenomena in Combustion*.

Santorro, R. J., Semerjian, H. G., Emmerman, P. J., and Goulard, R. (1980), AIAA 15th Thermophysics Conference, Paper # AIAA-80- 1541.

Schoenung, S. M., and Hanson, R. K. (1981), *Comb. Sci. and Tech.*, 24: 227-237.

Seitzman, J. M. (1991), “*Quantitative Applications of Fluorescence Imaging in Combustion*”, Ph.D. Thesis, Dept. of Mech. Engr., Stanford University, CA, HTGL Report No. T-275.

Shepp, L. A. and Logan, B. F. (1974), *IEEE Transactions on Nuclear Science*, NS-21, 21-43.

Silver, J. A. (1992), *Applied Optics*, **31**: 6, 707-717.

Silver, J. A. and Stanton, A. (1991), private communication, Southwest Sciences Inc., Santa Fe, NM.

Sirota, J.M., Reuter, D.C., and Mumma, M.J. (1993), *Applied Optics*, **32**: 12, 2117-2121.

Smith, L. L. (1994), “*Differential Molecular Diffusion in Reacting and Nonreacting Turbulent Jets of H₂/CO₂ Mixing with Air*”, Ph.D. Thesis, Dept. of Mech. Engr., University of California at Berkeley.

Smith, G. P. and Crosley, D. R. (1983), *Applied Optics*, **22**, 1428.

Smooke, M. D. (1992), “*Major research Topics in Combustion*”, Chapter: *Numerical Modeling of Two-Dimensional Axisymmetric Laminar Diffusion Flame*, Springer-Verlag.

Sobelman, I. I., Vainshtein, L. A., Yukov, E. A. (1981), “Excitation of Atoms and Broadening of Spectral Lines”, Springer-Verlag, Chap. 7.

Steiglitz, K (1974), “An Introduction to Discrete Systems”, J. Wiley and Sons, New York.

Sullivan, B. J. and Crosley, D. R. (1982), *Bull. Am. Phys. Soc.*, **27**, 882.

Beiting, E. (1990), AIAA 28th Aerospace Sciences Meeting, Paper # AIAA-90-0157.

Thoman Jr., J. W., Gray, J. A., Durant Jr., J. L., Paul, P. H. (1992), *J. Chem. Phys.*, **97** (11), 8156-8163.

Thorne, A. P. (1988), "Spectrophysics, 2nd Edition", Chapman and Hall, 262-264.

Thorne, L. R., Branch, M. C., Chandler, D. W., Kee, R. J., and Miller, J. A. (1986),
Twenty-first Symposium (International) on Combustion/The Combustion Institute,
 Pittsburgh, PA, 965-977.

Tjossem, P. J. H. and Smyth, K. C., *J. Chem. Phys.*, **91**: 4, 2041-2048.

Varghese, P.L., and Hanson, R.K. (1980), *J. Quant. Spectrosc. Radiat. Transfer*, **24**,
 479-489.

Varghese, P.L., and Hanson, R.K. (1981), *J. Quant. Spectrosc. Radiat. Transfer*, **26**: 4, 479-
 489.

Westblom, U., Agrup, S., Aldén, M., Hertz, H. M., and Goldsmith, J. E. M. (1990),
Applied Physics B, **50**, 487-497.

Westbrook, C. K., and Dryer, F. L. (1984), *Prog. Energy Combust. Sci.*, **10**: 1- 57.

Williams, B. A. and Fleming, J. W. (1994), *Combust. Flame*, **98**: 93-106.

Yardley, J. T. (1980), "Introduction to Molecular Energy Transfer", Academic Press, 296-
 301.

Yetter, R.A. and Dryer, F.L. (1992), *The Twenty-Fourth Symposium (International) on
 Combustion/The Combustion Institute*, 757-767.

Zeldovich, Ya. B. (1946), *Acta Physecochem USSR*, **21**, 557.

Appendix A

CO linestrength and position, Voigt function, and Galatry Function Codes

These are the FORTRAN codes used to calculate the CO linestrengths and positions using a term energy approach (Dunham Coefficients). There are also subroutines that calculate the Voigt profile and Galatry profile. These subroutines were provided by Prof. Phillip Varghese of the Dept of Mech. Engr. at the Univ. of Texas at Austin.

```

c
c --- main program to calculate the ratio of linestrengths
c --- and associated collisional widths, voigt profiles etc.
c --- recall that Beers law is given by:
c
c      I/Io = exp(-So*S(T,V,J,Br)*G(T,nu)*Pco*XL)
c      So is the fundamental linestrength - measured from Varghese and Hanson
c      the term S is the fractional linestrength calculated
c      from Quantum mechanics, the term G = 1/dopplerwidth*Voigt*consts.
c      the voigt function is calculated based on a voigt parameter
c      determined by the collisional width data from Varghese and Hanson
c      the Doppler width is a function of temperature and MW only
c
program coconc
parameter(np=41)
double precision WL
real trans(np), temp(np), pco(np)
character*20 transn, tempn
write(*,*) ' enter the vibrational level '
read(*,*) NNV
write(*,*) ' enter the rotational level '
read(*,*) NNJ
c      write(*,*) ' enter the temperature '
c      read(*,*) T
c      write(*,*) ' enter the transmission '
c      read(*,*) trans
c      write(*,*) ' enter the pathlength in cm '
c      read(*,*) xpath
c
c --- pathlength for 0.025 in. ---
c
xpath = 0.0635
write(*,*) ' enter the input file for trans '
read(*,*) transn
write(*,*) ' enter the input file for temp '
read(*,*) tempn
open(unit=1,file=transn,status='unknown',recl=200)
open(unit=2,file=tempn,status='unknown',recl=200)

```

```

        open(unit=3,file='pco.grd',status='unknown',recl=200)
c
c
c
        do 11 jj=1,np
        read(1,*) dum1, trans(jj)
        write(*,*) trans(jj)
11      continue
c
c
        write(*,*)'***** TEMP *****'
        do 12 j=1,np
        read(2,*) dum2, temp(j)
        write(*,*)temp(j)
12      continue
c
c XL is the pathlength
c -- times 2 for backpropagating beam ---
        XL = xpath*2.0
c
c -- sfund is fundamental bandstrength in cm-2 atm-1 ---
c      from varghese and hanson
c
        sfund = 283.0
c
c
c -- set NB = -1 for P or +1 for R
c
        NB = -1
        if(NB.eq.1) NBG = 1
        if(NB.eq.-1) NBG = 0
c
c --- account for variation in collisional width with J and T ---
c --- from Varghese and Hanson (A linear function in J) ---
c --- inversely prop to sqrt(T) referenced to 1850K ----
c
c
        do 222 j=1,np
        if(temp(j).eq.0) temp(j)=300.0
        dwcnum = -0.000226*float(NNJ+NBG)+0.042*sqrt(1850./temp(j))
c
        call colst(temp(j),NNV,NNJ,NB,SL,WL)
        wnum = WL
c      write(*,*)' -- 1 --'
c
c --- calc doppler width ---
c
        dopnum = (7.16e-7)*sqrt(temp(j)/28.0)*wnum
c
c --- calc voigt param ---
c
        anum = 0.83255*dwcnum/dopnum
c
c --- call voigt profile at line center ---
c
        Vnum = VOIGT(0.0,anum)
c
c --- 2*ln(sqrt(2/pi))=0.9394 ---
c
        G = 0.9394*Vnum/dopnum
c

```



```

c--- calc Pco based on Beer's law ---
c
      pco(j) = log(trans(j))/(-sfund*SL*G*XL)
c
c
222      continue
c
c --- output ---
c
      i=0
      do 335 j=21,np
      i=i+1
      write(3,*) float(i-1)/20., trans(j),temp(j),pco(j)
335      continue
      close(1)
      close(2)
      close(3)
      stop
      END
c

      SUBROUTINE COLST(T,V,J,NBRNCH,SL,WL)
C*****
C      THIS SUBROUTINE AND ASSOCIATED FUNCTIONS COMPUTE THE LINE STRENGTH
C      AND LINE POSITION OF THE CO LINE SPECIFIED. THE LINE STRENGTH IS
C      COMPUTED AS A FRACTION OF THE BAND STRENGTH AT 273.2 K.
C
C      INPUT PARAMETERS:
C          T          TEMPERATURE
C          V          VIBRATIONAL QUANTUM NUMBER OF THE LOWER STATE
C          J          ROTATIONAL QUANTUM NUMBER OF THE LOWER STATE
C          NBRNCH +1 => R BRANCH TRANSITION
C                -1 => P BRANCH TRANSITION
C      OUTPUT PARAMETERS:
C          SL          LINE STRENGTH OF THE TRANSITION AT TEMPERATURE T
C          WL          LINE POSITION IN cm-1
C*****
      INTEGER V,VP1
      DOUBLE PRECISION Y10,Y20,Y01,Y11,Y02,Y12,Y30,Y40,Y50,Y60,Y03,Y13
      1,Y21,Y31,Y22,GV,FV,F1,F2,F3,FP1,FP2,FP3,WL,GVP1
      DATA Y10,Y20,Y01,Y11,Y02,Y12/2.169813844D+03,-1.32884214D+01
C,1.93128088D+00,-.175043079D-01,-.6120712D-05,.106399D-08/
      DATA Y30,Y40,Y50,Y60,Y03,Y13,Y21,Y31,Y22/.1052536D-01
C,.56644D-04,.100327D-05,-.318476D-07,.56676D-11,-.162587D-12
C,.56767D-06,.23691D-07,-.178578D-09/
      DATA HCDK/1.438789/
      DATA WBARO/2147.36/
      HCDKT=HCDK/T
C*****
C      THE PARTITION FUNCTION Q IS COMPUTED BY SUMMING OVER ALL STATES
C      THAT ARE SIGNIFICANTLY POPULATED AT TEMPERATURES UPTO ABOUT 3000 K
C*****
      Q=0.
      DO 10 VP1=1,11
      VH=VP1-0.5
      GV=VH*(Y10+VH*(Y20+VH*(Y30+VH*(Y40+VH*(Y50+VH*Y60))))
      F1=Y01+VH*(Y11+VH*(Y21+VH*Y31))
      F2=Y02+VH*(Y12+VH*Y22)
      F3=Y03+VH*Y13
      DO 10 JJ=0,150

```

```

TVJ=GV+FV(F1,F2,F3,JJ)
Q=Q+(2*JJ+1.)*EXP(-TVJ*HCDKT)
10 CONTINUE
S1=(V+1)*273.2/(T*WBARO)
VH=V+.5
F1=Y01+VH*(Y11+VH*(Y21+VH*Y31))
F2=Y02+VH*(Y12+VH*Y22)
F3=Y03+VH*Y13
VPH=V+1.5
FP1=Y01+VPH*(Y11+VPH*(Y21+VPH*Y31))
FP2=Y02+VPH*(Y12+VPH*Y22)
FP3=Y03+VPH*Y13
GV=VH*(Y10+VH*(Y20+VH*(Y30+VH*(Y40+VH*(Y50+VH*Y60))))
GVP1=VPH*(Y10+VPH*(Y20+VPH*(Y30+VPH*(Y40+VPH*(Y50+VPH*Y60))))
JB1=J+NB RNCH
WL=GVP1-GV+FV(FP1,FP2,FP3,JB1)-FV(F1,F2,F3,J)
SK=S1*EXP(-HCDKT*SNGL(GV+FV(F1,F2,F3,J)))
BK=AMAX0(J,JB1)*WL*(1.-EXP(-HCDKT*SNGL(WL)))
SL=SK*BK/Q
RETURN
END

C
C
DOUBLE PRECISION FUNCTION FV(F1,F2,F3,J)
DOUBLE PRECISION F1,F2,F3,XJ
XJ=J*(J+1)
FV=XJ*(F1+XJ*(F2+XJ*F3))
RETURN
END

SUBROUTINE CPF(X,Y,WR,WI)
C*****
C
C THIS ROUTINE COMPUTES THE REAL (WR) AND IMAGINARY (WI) PARTS OF
C THE COMPLEX PROBABILITY FUNCTION w(z),
C
C  $w(z) = \exp(-z*z) * \operatorname{erfc}(-i*z),$ 
C
C WHERE erfc IS THE COMPLEMENTARY ERROR FUNCTION. THE COMPUTATION
C IS VALID FOR THE UPPER HALF PLANE OF  $z = x + iy$ , ie  $y > 0$ .
C
C MAXIMUM RELATIVE ERROR FOR WR IS < 2.E-6 AND FOR WI IS < 5.E-6.
C
C SUBROUTINE ADAPTED FROM:
C J. HUMLICEK, J. QUANT. SPECTROSC. RADIAT. TRANSFER 21, 309 (1979)
C
C PHILIP L. VARGHESE <820315.0112>
C
C*****
DIMENSION T(6), C(6), S(6)
DATA T/0.314240376E00,0.947788391E00,0.159768264E01,
* 0.227950708E01,0.302063703E01,0.38897249E01/
DATA C/0.101172805E01,-0.75197147E00,0.12557727E-01,
* 0.100220082E-01,-0.242068135E-03,0.500848061E-06/
DATA S/0.1393237E01,0.231152406E00,-0.155351466E00,
* 0.621836624E-02,0.919082986E-04,-0.627525958E-06/
WR=0.
WI=0.
Y1=Y+1.5
Y2=Y1*Y1
C*****

```

```

C
C      BRANCH TO REGION I OR II DEPENDING ON VALUES OF X AND Y.
C
C*****
      IF(Y.GT.0.85.OR.ABS(X).LT.(18.1*Y+1.65)) GO TO 20
C*****
C
C      CALCULATIONS FOR REGION II
C
      IF (ABS(X).LT.12.) WR=EXP(-X*X)
      Y3=Y+3.
      DO 10 I=1,6
      R=X-T(I)
      R2=R*R
      D=1./(R2+Y2)
      D1=Y1*D
      D2=R*D
      WR=WR+Y*(C(I)*(R*D2-1.5*D1)+S(I)*Y3*D2)/(R2+2.25)
      R=X+T(I)
      R2=R*R
      D=1./(R2+Y2)
      D3=Y1*D
      D4=R*D
      WR=WR+Y*(C(I)*(R*D4-1.5*D3)-S(I)*Y3*D4)/(R2+2.25)
10    WI=WI+C(I)*(D2+D4)+S(I)*(D1-D3)
      RETURN
C
C      END OF CALCULATIONS FOR REGION II
C
C*****
C
C      CALCULATIONS FOR REGION I
C
20    DO 30 I=1,6
      R=X-T(I)
      D=1./(R*R+Y2)
      D1=Y1*D
      D2=R*D
      R=X+T(I)
      D=1./(R*R+Y2)
      D3=Y1*D
      D4=R*D
      WR=WR+C(I)*(D1+D3)-S(I)*(D2-D4)
30    WI=WI+C(I)*(D2+D4)+S(I)*(D1-D3)
      RETURN
C
C      END OF CALCULATIONS FOR REGION I
C
C*****
      END
      SUBROUTINE VGTRY(X,Y,Z,G)
C*****
C
C      THIS ROUTINE COMPUTES THE STANDARDIZED GALATRY FUNCTION
C      G(x',y,z) WHERE:
C      x'(X) IS THE DISTANCE FROM THE SHIFTED LINE CENTER, x'=x-s
C      y(Y) IS THE COLLISIONAL BROADENING PARAMETER, AND
C      z(Z) IS THE COLLISIONAL NARROWING PARAMETER.
C      x', y, z ARE NORMALIZED BY THE 1/e DOPPLER HALFWIDTH
C      y CORRESPONDS TO THE VOIGT a COEFFICIENT, AND G(x,y,0) = V(x,a)
C

```

```

C      THE VOIGT FUNCTION IS THE REAL PART OF THE COMPLEX PROBABILITY *
C      FUNCTION COMPUTED BY THE EXTERNAL ROUTINE CPF. *
C *
C      PHILIP L. VARGHESE <821116.1042> *
C *
C*****
C      COMPLEX I,Q,W,DW(8),A(75),A0,ALPHA
C      DIMENSION C(8),FACT(8),DEL(8)
C      DATA I,ZOLD,RTPI/(0.,1.),0.,1.772454/
C      DATA FACT/1.,2.,6.,24.,120.,720.,5040.,40320./
C      DATA N2MAX,N3MAX/75,75/
C      IF(Z.GT.0.) GO TO 5
C*****
C
C      IF Z=0, COMPUTE VOIGT FUNCTION (REAL(CPF)).
C
C      CALL CPF(X,Y,G,WI)
C      RETURN
C
C*****
C
C      BRANCH TO REGIONS I-III OF Y,Z PLANE DEPENDING ON INPUTS.
C
C      5      CONTINUE
C            IF(Z.GT.5.) GO TO 200
C            IF(Z.LE.0.1) GO TO 90
C            IF(Y.GE.(4.*Z**0.868)) GO TO 300
C            GO TO 200
C      90      IF((Y.GE.0.5).OR.(Z.GT.0.04).OR.(X.GT.2.)) GO TO 300
C
C*****
C
C      REGION I - (0<y<0.5, 0<z<0.04, x<2) EXPANSION ABOUT THE VOIGT
C      FUNCTION.
C
C      COMPUTE THE COEFFICIENTS OF THE ASYMPTOTIC EXPANSION OF
C
C            n=N          n=N
C      exp(-1/(2*z*z))*Sigma{(-z*t)**n/n!} = 1 + Sigma{c(n)*t**n}
C            n=3          n=3
C
C
C      IF THE VALUE OF Z IS UNCHANGED SINCE THE LAST CALL THE
C      COEFFICIENTS ARE NOT RECOMPUTED.
C
C
C      100     CONTINUE
C             IF (Z.EQ.ZOLD) GO TO 15
C             ZOLD=Z
C             DO 10 J=3,8
C      10      C(J)=-(-Z)**(J-2)/(2.*FACT(J))
C             C(6)=C(6)+C(3)*C(3)/2.
C             C(7)=C(7)+C(3)*C(4)
C             C(8)=C(8)+C(3)*C(5)+C(4)*C(4)/2
C      15      CALL CPF(X,Y,WR,WI)
C             Q=CMPLX(X,Y)
C             W=CMPLX(WR,WI)
C
C
C      COMPUTE DERIVATIVES (DW) OF THE COMPLEX PROBABILITY FUNCTION (W).
C
C      DW(1)=2*(I/RTPI-Q*W)
C      DW(2)=-2*(Q*DW(1)+W)

```

```

      DO 20 J=3,8
20    DW(J)=-2*(Q*DW(J-1)+(J-1)*DW(J-2))
      C
      C      COMPUTE CORRECTION TO THE VOIGT PROFILE. IF THE ASYMPTOTIC
      C      EXPANSION DIVERGES THEN TERMINATE.
      C
      DELT=REAL(C(3)*DW(3)*I)
      DO 30 J=4,8
      DEL(J)=REAL(C(J)*DW(J)/I**J)
      IF(ABS(DEL(J)).GE.ABS(DEL(J-1))) GO TO 35
      DELT=DELT+DEL(J)
30    CONTINUE
35    G=WR+DELT
      RETURN
      C
      C*****
      C
      C      REGION II - A & B      (0<y<4z**.868, 0.1<z<5) & (all y, z>5).
      C
      C      THE NUMBER OF TERMS IN THE SUM WAS DETERMINED EMPIRICALLY.
      C
200   CONTINUE
      N2=4+(1.+3.*EXP(-1.1*Y))/Z**1.05
      IF(N2.GT.N2MAX) N2=N2MAX
      Q=CMPLX(Y,-X)
      DELL=0.5/(Z*Z)
      ALPHA=DELL*(1.+2*Z*Q)
      W=1./ALPHA
      A(1)=W*DELL/(ALPHA+1)
      W=W+A(1)
      DO 210 J=2,N2
      A(J)=A(J-1)*DELL/(ALPHA+J)
      W=W+A(J)
210   CONTINUE
      G=REAL(W)/(RTPI*Z)
      RETURN
      C
      C*****
      C
      C      REGION III - (y>1, 0.4<z<0.1) & (y>4z**.868, 0.1<z<5).
      C
      C      THE NUMBER OF TERMS IN THE CONTINUED FRACTION WAS DETERMINED
      C      EMPIRICALLY.
      C
300   CONTINUE
      N3=2+37.*EXP(-0.6*Y)
      IF(N3.GT.N3MAX) N3=N3MAX
      Q=CMPLX(Y,-X)
      A(N3)=0.5*N3/(N3*Z+Q)
      DO 310 J=N3,1,-1
      A(J)=0.5*J/(J*Z+Q+A(J+1))
310   CONTINUE
      A(1)=1./(Q+A(1))
      G=REAL(A(1))/RTPI
      RETURN
      C
      C*****
      C      END
      C      FUNCTION VOIGT(X,Y)
      C*****
      C      THIS ROUTINE COMPUTES THE VOIGT FUNCTION :Y/PI*INTEGRAL FROM

```

```

C      - TO + INFINITY OF EXP(-T*T)/(Y**2+(X-T)**2)DT
C*****
      REAL B(22),RI(15),XN(15),YN(15),D0(25),D1(25),D2(25),D3(25),
      1D4(25),HN(25),XX(3),HH(3),NBY2(19),C(21)
      LOGICAL TRU
      DATA B(1),B(2)/0.,.7093602E-7/,XN/10.,9.,2*8.,7.,6.,5.,4.,7
      1*3./,YN/3*.6,.5,2*.4,4*.3,1.,.9,.8,2*.7/,
      2H/.201/,XX/.5246476,1.65068,.7071068/,
      3HH/.2562121,.2588268E-1,.2820948/,NBY2/9.5,9.,8.5,8.,7.5,7.,6.5
      4,6.,5.5,5.,4.5,4.,3.5,3.,2.5,2.,1.5,1.,.5/,C/.7093602E-7,-.2518434
      5E-6,.8566874E-6,-.2787638E-5,.860774E-5,-.2565551E-4,.7228775E-4
      6,-.1933631E-3,.4899520E-3,-.1173267E-2,.2648762E-2,-.5623190E-2,
      7.1119601E-1,-.2084976E-1,.3621573E-1,-.5851412E-1,.8770816E-1,
      8-.121664,.15584,-.184,.2/
      DATA TRU/.FALSE./
      IF (TRU) GO TO 104
C*****
C      REGION I: COMPUTE DAWSON'S FUNCTION AT MESH POINTS.
C*****
      TRU=.TRUE.
      DO 101 I=1,15
101      RI(I)=-I/2.
      DO 103 I=1,25
      HN(I)=H*(I-.5)
      CO=4.*HN(I)*HN(I)/25.-2.
      DO 102 J=2,21
102      B(J+1)=CO*B(J)-B(J-1)+C(J)
      D0(I)=HN(I)*(B(22)-B(21))/5.
      D1(I)=1.-2.*HN(I)*D0(I)
      D2(I)=(HN(I)*D1(I)+D0(I))/RI(2)
      D3(I)=(HN(I)*D2(I)+D1(I))/RI(3)
103      D4(I)=(HN(I)*D3(I)+D2(I))/RI(4)
104      IF (X-5.) 105,112,112
105      IF (Y-1.) 110,110,106
106      IF (X.GT.1.85*(3.6-Y)) GO TO 112
C*****
C      REGION II:CONTINUED FRACTION. COMPUTE NUMBER OF TERMS NEEDED.
C*****
      IF (Y.LT.1.45) GO TO 107
      I=Y+Y
      GO TO 108
107      I=11.*Y
108      J=X+X+1.85
      MAX=XN(J)*YN(I)+.46
      MIN=MIN0(16,21-2*MAX)
C*****
C      EVALUATE CONTINUED FRACTION
C*****
      UU=Y
      VV=X
      DO 109 J=MIN,19
      U=NBY2(J)/(UU*UU+VV*VV)
      UU=Y+U*UU
109      VV=X-U*VV
      VOIGT=UU/(UU*UU+VV*VV)/1.77454
      RETURN
110      Y2=Y*Y
      IF (X+Y.GE.5.) GO TO 113
C*****
C      REGION I: COMPUTE DAWSON'S FUNCTION AT X FROM TAYLOR SERIES.
C*****

```

```

      N=X/H
      DX=X-HN(N+1)
      U=((D4(N+1)*DX+D3(N+1))*DX+D2(N+1))*DX+D1(N+1))*DX+D0(N+1)
      V=1.-2.*X*U
C*****
C      TAYLOR SERIES EXPANSION ABOUT Y=0.0
C*****
      VV=EXP(Y2-X*X)*COS(2.*X*Y)/1.128379-Y*V
      UU=-Y
      MAX=5.+(12.5-X)*.8*Y
      DO 111 I=2,MAX,2
      U=(X*V+U)/RI(I)
      V=(X*U+V)/RI(I+1)
      UU=-UU*Y2
111   VV=VV+V*UU
      VOIGT=1.128379*VV
      RETURN
112   Y2=Y*Y
      IF (Y.LT.11-.6875*X) GO TO 113
C*****
C      REGION IIIB: 2-POINT GAUSS-HERMITE QUADRATURE.
C*****
      U=X-XX(3)
      V=X+XX(3)
      VOIGT=Y*(HH(3)/(Y2+U*U)+HH(3)/(Y2+V*V))
      RETURN
C*****
C      REGION IIIA: 4-POINT GAUSS-HERMITE QUADRATURE.
C*****
113   U=X-XX(1)
      V=X+XX(1)
      UU=X-XX(2)
      VV=X+XX(2)
      VOIGT=Y*(HH(1)/(Y2+U*U)+HH(1)/(Y2+V*V)+HH(2)/(Y2+UU*UU)+HH(2)/
1(Y2+VV*VV))
      RETURN
      END
C
C

```

Appendix B

Tomographic reconstruction FORTRAN codes

```

c This program implements the Fourier Deconvolution Algorithm
c
c Q. Viet Nguyen Aug.1992
c
c
c      PROGRAM Fourier
c      parameter(ni=100,nn=100)
c      IMPLICIT DOUBLE PRECISION (A-H,O-Z)
c      DIMENSION PHI(ni), PROJ(ni), CONV(ni),TPROJ(nn)
c              DIMENSION Z(nn,nn), ICR(nn), ReconP(ni)
c      CHARACTER*40 INFILE
c      CHARACTER*40 OUTFILE
c
c      INPUT FROM UNIT 1
c
c      OUTPUT TO UNIT 3
c
c      write(*,106)
106  FORMAT(' INPUT NUMBER OF ANGLES, GRID POINTS: ')
c      read(*,*) NANG,NX
c      NANG = 10
c      NX = 100
c
c1  CONTINUE
c      write(*,100)
100  FORMAT(' NAME OF INPUT FILE: ')
c      read(*,*) INFILE
c      write(*,102)
c102 FORMAT(' NAME OF OUTPUT FILE: ')
c      read(*,103) OUTFILE
c103 FORMAT(A40)
c      OPEN (UNIT=1,FILE=infile,STATUS='UNKNOWN')
c      OPEN (UNIT=3,FILE='tomo.out',STATUS='UNKNOWN',recl=1200)
c      open(5,file='cross.out',status='unknown')
c
c      INPUT MEASUREMENTS, FIND MINIMUM
c
c      PROMIN = 1.
c      DO 3 K=1,nx
c      READ(1,*) DUM, TPROJ(K)
c      IF (TPROJ(K).LT.PROMIN) PROMIN=TPROJ(K)
3      CONTINUE
c
c      SEARCH FOR HALF-MINIMUM CROSSINGS
c
c      NC = 1

```



```

      IFLAG = 0
      HALF = (PROMIN+1.)/2.
      DO 4 K=1,nn-1
      IF (TPROJ(K).GT.HALF.AND.TPROJ(K+1).LT.HALF) IFLAG=1
      IF (TPROJ(K).LT.HALF.AND.TPROJ(K+1).GT.HALF) IFLAG=1
      IF(IFLAG.NE.1) GO TO 4
      ICR(NC) = K
      NC = NC+1
      IFLAG = 0
4      CONTINUE
      write(*,110) (ICR(K), K=1,NC-1)
110    FORMAT('  CROSSINGS AT: ',5I4)
      C
      IF (NC.GT.3) GO TO 2
      C
      MCENT = (ICR(1)+ICR(2))/2.
      IZER = 1
      DO 6 K=1,ICR(1)
      PROD = (TPROJ(K)-1.)*(TPROJ(K+1)-1.)
      IF(PROD.LE.0.) IZER = K
6      CONTINUE
      C
      MR = MCENT - IZER
      write(*,*) ' CENTER, RADIUS:',MCENT,MR
      C
      write(*,*) ' AUTOMATIC DATA-RANGE SELECTION? (1 = YES)'
      read(*,*) IAUTO
      c      IAUTO = 1
      IF (IAUTO.NE.1) GO TO 2
      C
      GO TO 8
      C
2      write(*,104)
104    FORMAT(' INPUT INDEX FOR CENTERLINE: ')
      read(*,*) MCENT
      C
      write(*,105)
105    FORMAT(' INPUT NUMBER OF POINTS ON RADIUS: ')
      read(*,*) MR
      C
8      M = 2* MR + 1
      MMIN = MCENT - MR
      MMAX = MCENT + MR
      LENGTH = M - 1
      C
      C      WRITE(3,302) LENGTH, NX, NANG
302    FORMAT(3I6)
      C
      NY = NX
      C
      C      AVERAGE MEASUREMENTS BETWEEN TWO SIDES, TAKE LOGARITHM, AND RENUMBER
      C
      I = 1
      DO 5 K=MMIN,MCENT
      PROJ(I) = -DLOG((TPROJ(K)+TPROJ(MMAX+1-I))/2.)
      PROJ(M+1-I) = PROJ(I)
      I = I+1
5      CONTINUE
      C
      XPOS = .99
      YPOS = .99

```

```

C      DO 7 IDM=1,NX
      DO 7 JDM=1,NY
7      Z(IDM,JDM)=0.
      PI = 2. * ASIN(1.0)
      N = NANG
      A = 2.0/dfloat(M)
      PIN = PI/dfloat(N)
      C2 = -1./(2.*PI*A*dfloat(N))
      DELTA = 2.*XPOS/dfloat(NX)
C
      PHI(1) = 2./(PI*A*dfloat(N))
      DO 10 K=1,M-1
10     PHI(K+1) = C2/(dfloat(K)*dfloat(K)-.25)
      CONTINUE
C
      DO 20 J=1,N
      THETAJ = (J-1)*PIN
      COSTHTAJ = COS(THETAJ)
      SINTHTAJ = SIN(THETAJ)
      COSDELOA = COSTHTAJ*DELTA/A
C
      IF (J.GT.1) GO TO 35
C
      DO 30 KR=1,M
      CONV(KR) = 0.
      DO 40 K=1,M
      KABS = IABS(KR-K) + 1
      CONV(KR) = CONV(KR) + PROJ(K) * PHI(KABS)
40     CONTINUE
30     CONTINUE
C
35     CONTINUE
C
      DO 51 IY=1,NY
      Y1=-YPOS+2.*YPOS*Dfloat(IY)/Dfloat(NY)
      R=(-XPOS*COSTHTAJ+SINTHTAJ*Y1+1.)/A-COSDELOA
      DO 50 I=1,NX
      R=R+COSDELOA
      L=R
      IF(L.LE.0.OR.L.GE.M) GO TO 50
      Z(I,IY)=Z(I,IY)+(L+1.-R)*CONV(L)+(R-L)*CONV(L+1)
c      write(*,*) I,IY,Z(I,IY)
50     CONTINUE
51     CONTINUE
20     CONTINUE
c
c --- smoothing ---
c -- 1/16 weighting on adjacent 8 nodes, 1/2 weighting on center node --
c
      do 2000 jj=2,nx-1
      do 1000 ii=2,nx-1
      z(ii,jj) = (z(ii+1,jj+1)+z(ii+1,jj)+z(ii,jj+1)+
& z(ii-1,jj+1)+z(ii-1,jj)+z(ii-1,jj-1)+z(ii,jj-1)+z(ii+1,jj-1))
& *0.0625+0.5*z(ii,jj)
1000    continue
2000    continue
      do 3000 jj=1,nx
      do 4000 ii=1,nx
      z(ii,jj) = dexp(-z(ii,jj))
      if(z(ii,jj).gt.1.0) z(ii,jj) = 1.00

```

```

4000  continue
3000  continue
c
      DO 60 J=1,NY
      WRITE(3,301) (Z(I,J),I=1,NX)
301   FORMAT(100(E11.3,1x))
60    CONTINUE
c
c --- integrate along paths to compare with original data ---
c
      do 3100 j=1,m
      sum2 = 0.0
      do 3200 i=1,m
      sum2 = sum2 - dlog(z(i,j))
3200  continue
      reconP(j) = dexp(-sum2)
3100  continue
      do 3300 i=1,m
      write(5,*) i, TProj(i),reconP(i)
3300  continue
c
      CLOSE(UNIT=1)
      CLOSE(UNIT=3)
      close(5)
c
c   GO TO 1
      STOP
      END

      program rat
c
c --- this program divides the log of two n by n fields ---
c   to calculate the Boltzmann temperature
c   Q. Viet Nguyen Aug. 1992
c
      parameter(n=53)
      double precision z1(n,n), z2(n,n), ratio(n,n)
      character*20 fname1, fname2
      write(*,*) ' enter the numerator field filename '
      read(*,*) fname1
      write(*,*) ' enter the denominator field filename '
      read(*,*) fname2
      open(1,file=fname1,status='old',recl=1200)
      open(2,file=fname2,status='old',recl=1200)
      open(3,file='ratio.grd',status='unknown',recl=1200)
c
c
      do 100 j=1,n
      read(1,*)(z1(i,j),i=1,n)
      read(2,*)(z2(i,j),i=1,n)
100   continue
c
c --- divide, check for division by zero ---
c
      do 200 j=1,n
      do 300 i=1,n
      if(dlog(z2(i,j)).eq.0) then
      ratio(i,j) = 0.0
      else
      ratio(i,j) = dlog(z1(i,j))/dlog(z2(i,j))

```

```

endif
300 continue
200 continue
c
c --- filter function ---
c
      do 500 j=2,n-1
      do 600 i=2,n-1
        ratio(i,j) = (ratio(i,j)+ratio(i+1,j+1)+ratio(i,j+1)+
& ratio(i,j-1)+ratio(i-1,j)+ratio(i-1,j-1)+ratio(i-1,j)+
& ratio(i-1,j+1)+ratio(i,j+1))/9.00
600 continue
500 continue
c
c --- output ----
c
      do 400 j=1+8,n-8
      write(3,333)(ratio(i,j),i=1+8,n-8)
400 continue
333 format(41(f10.4,1x))
      close(1)
      close(2)
      close(3)
      stop
      end

program temp
c
c --- this program calculates the temperature field based on the
c --- ratio field of the log of the transmissions for a vibrotational
c --- transition. This works by table lookup.
c
      parameter(np=41,nt=50)
      implicit real*8 (a-h,o-z)
      real*8 rat1(np,np),trat(nt),rat(nt),T(np,np)
      real*8 rattemp(nt),trattemp(nt)
      character*20 fname1, fname1, fnameout
      write(*,*) ' enter name of ratio field '
      read(*,*) fname1
      write(*,*) ' enter name of temp vs. ratio data '
      read(*,*) fname1
      write(*,*) ' enter name of output temp field '
      read(*,*) fnameout
c
      open(1,file=fname1,status='old',recl=450)
      open(2,file=fname1,status='old')
      open(3,file=fnameout,status='unknown',recl=450)
c
      do 100 j=1,np
      read(1,*)(rat1(i,j),i=1,np)
100 continue
c
c
c      do 110 j=1,np
c      write(*,*) rat1(20,j)
c110 continue
c
      do 200 i=1,nt

```

```

        read(2,*) trat(i), dummy1, dummy2, rat(i)
200    continue
c
c --- if data is not monotonically increasing, reorder ---
c
        if (rat(2).lt.rat(1)) then
            do 250 i=1,nt
                rattemp(i) = rat(i)
                trattemp(i) = trat(i)
250    continue
                k = nt+1
                do 270 i=1,nt
                    k = k-1
                    rat(i) = rattemp(k)
                    trat(i) = trattemp(k)
                    write(*,*) rat(i),trat(i)
270    continue
                endif
                rmax = rat(nt)
                rmin = rat(1)
c                write(*,*) ' rmin = ',rmin
c                write(*,*) ' rmax = ',rmax
c
c
                do 300 j=1,np
                    write(*,*) ' J = ',j
                    do 400 i=1,np
c                        write(*,*) ' I = ',i
c
c --- if ratio is out of range set T to 0 ----
c
                        if(rat1(i,j).gt.rmax.or.rat1(i,j).lt.rmin) then
                            T(i,j) = 0.0
                        else
                            T(i,j) = xinterp(rat1(i,j),rat,trat)
                        endif
c                        write(*,*) T(i,j)
400    continue
300    continue
c
c
c                write(*,*) ' writing output file'
c
                do 1000 j=1,np
                    write(3,1100)(T(i,j),i=1,np)
1000    continue
1100    format(41(f10.1,1x))
c
                close(1)
                close(2)
                close(3)
                stop
                end
c
c --- linear interpolation function ---
c
        double precision function xinterp(xd,x,y)
        implicit real*8 (a-h,o-z)
        dimension x(50),y(50)
        n = 50

```

```
do 200 i=2,n-1
  if(x(i).gt.xd) goto 210
200 continue
  i = n
210 continue
  i = i-1
  xinterp = y(i)+(xd-x(i))*(y(i+1)-y(i))/(x(i+1)-x(i))
  return
end
```

Appendix C

Modulation Spectroscopy Simulation Codes

These are the FORTRAN codes used to simulate the 2f modulation spectroscopy process. The program generates a time series simulating the modulated laser light as it passes through an absorption medium. The time series is then processed with an FFT algorithm. The coefficients of the FFT output are the Fourier components of the time series. These coefficients are proportional to the 1f, 2f, 3f, etc... harmonics of the modulation signal. The input file contains the parameters such as modulation frequency, temperature, concentration etc.

This is the input file for the 2f6 modulation simulation program.

```
300.0,      1.00,    100.0,    10.0
 0.035,    25.0,      8.0,    0.10,    0.00
 50.0,      1.0
    0,      16,     -1
2077.30,    2078.00
```

```
temp (K), press (atm), conc (ppm), pathlength (cm)
modulation (cm-1), voigt param (n.d.), slope, int, turb (fract.)
mod freq (kHz), turb freq (kHz)
lower vib level, lower rot q. no., branch P=-1 R=+1
laser freq scan start (cm-1), scan end (cm-1)
```

```
c
c -- This program numerically simulates the absorption process of
c -- wavelength modulated laser light passing through an absorbing medium.
c -- Provisions for variable laser power, turbulence, and multiple
c -- absorption lines are included.
c
c -- The results are the fourier coefficients of interest vs laser
c -- linecenter frequency in wavenumbers. The calculations are
c -- performed using a FFT from Numerical Recipes by Press et al.
c
c -- A VOIGT absorption profile is assumed.
c
c -- linestrengths are calculated using Subroutine COLST
c -- courtesy of Phil Varghese
c
c --- by Quang-Viet Nguyen, July 30 1992, revised 8-15-92
c --- file is 2f6.for
c
c      program modulate
c
c
c -- n = number of discrete sampling points, a power of 2 only
```

```

c -- ni = number of output points in laser freq. space
c -- isign = +1 for forward fft (do not change)
c
c     parameter (n=512,ni=100,isign=1)
c
c
c     real w(n),gco(n),fj(n),fk(n),m,cf(ni)
c     real lco,wo(ni),gg(n)
c     double precision wco
c     open(unit=2,file='2f6.inp',status='old')
c     open(unit=3,file='2f2.dat',status='unknown')
c
c
c -- input parameters --
c
c     read(2,*) temp,press,cco,lco
c     read(2,*) m,aa,slope,b,aturb
c     read(2,*) omega,fturb
c     read(2,*) nv,jrot,nbranch
c     read(2,*) wstart,wend
c
c -- initial calculations --
c
c     mco = 28.0
c
c -- call COLST to calc. line strength and position using full
c -- stat. mech./spectroscopy theory
c
c     call colst(temp,nv,jrot,nbranch,sl,wco)
c
c -- linestrength is 283 cm-2 atm-1 at 273 K from Varghese and Hanson (1981)
c     sco = 283.0*sl
c -- calculate doppler width
c     dwco = 7.162e-7*sqrt(temp/mco)*sngl(wco)
c -- optical depth of CO (cm-1)
c     absco = cco*1.0e-6*press*sco*lco
c
c     pi = 4.0*atan(1.0)
c
c --- start laser freq increment ---
c
c --- print header ---
c
c     write(3,*)'# dwco = ',dwco,' T = ',temp,' P = ',press
c     write(3,*)'# voigt = ',aa,' absco = ',absco,' conc = ',cco
c     write(3,*)'# nbranch = ',nbranch,' jrot = ',jrot,' pos = ',wco
c
c     do 100 i=1,ni
c
c -- increment freq step
c
c     wo(i) = wstart + float(i-1)/float(ni)*(wend-wstart)
c
c     do 200 j=1,n
c
c --- increment time step and do 1 second total ---
c
c     t = float(j-1)/float(n-1)*1.0
c
c     w(j) = wo(i) + m * sin(2.0*omega*pi* t)
c

```



```

c --- calc lineshapes using Voigt Function
c
      xx = abs(w(j)-sngl(wco))*1.6651/dwco
      vv = VOIGT(xx,aa)
      gco(j) = 0.939437*vv/dwco
      gg(j) = exp(-absco*gco(j))
c
c --- convolve laser baseline and voigt profile
c --- also add a sinusoidal turbulence effect
c
      turb = 1.0-(aturb-aturb*sin(fturb*2.0*pi*t))
      fj(j) = (b+slope)*w(j)*gg(j)*turb
c
200  continue
c
c ---- call fast fourier transform ---
c
      nin = n/2
      call realft(fj,nin,isign)
c
c --- calc and normalize desired fourier coefs of interest ---
c
      np = int(omega)
      xnorm = float(n-1)
c
      f0 = real(fj(1))/(xnorm*w(1))
      f0 = (b+slope)*wo(i)*gg(1)/wo(1)
      f1 = real(fj(np*2+1))/xnorm
      f2 = -real(fj(np*4+1))/xnorm
c
c --- output data ---
c
      write(3,333) wo(i),f0,f1,f2
100  continue
c
333  format(f9.3,2x,e12.5,2x,e12.5,2x,e12.5)
      close(unit=2)
      close(unit=3)
      stop
      end
c
c --- from NUMERICAL RECIPES Book ----
c
      SUBROUTINE REALFT(DATA,N,ISIGN)
      REAL*8 WR,WI,WPR,WPI,WTEMP,THETA
      DIMENSION DATA(*)
      THETA=6.28318530717959D0/2.0D0/DBLE(N)
      C1=0.5
      IF (ISIGN.EQ.1) THEN
        C2=-0.5
        CALL FOUR1(DATA,N,+1)
      ELSE
        C2=0.5
        THETA=-THETA
      ENDIF
      WPR=-2.0D0*DSIN(0.5D0*THETA)**2
      WPI=DSIN(THETA)
      WR=1.0D0+WPR
      WI=WPI
      N2P3=2*N+3
      DO 11 I=2,N/2+1
        I1=2*I-1

```

```

      I2=I1+1
      I3=N2P3-I2
      I4=I3+1
      WRS=SNGL(WR)
      WIS=SNGL(WI)
      H1R=C1*(DATA(I1)+DATA(I3))
      H1I=C1*(DATA(I2)-DATA(I4))
      H2R=-C2*(DATA(I2)+DATA(I4))
      H2I=C2*(DATA(I1)-DATA(I3))
      DATA(I1)=H1R+WRS*H2R-WIS*H2I
      DATA(I2)=H1I+WRS*H2I+WIS*H2R
      DATA(I3)=H1R-WRS*H2R+WIS*H2I
      DATA(I4)=-H1I+WRS*H2I+WIS*H2R
      WTEMP=WR
      WR=WR*WPR-WI*WPI+WR
      WI=WI*WPR+WTEMP*WPI+WI
11  CONTINUE
      IF (ISIGN.EQ.1) THEN
        H1R=DATA(1)
        DATA(1)=H1R+DATA(2)
        DATA(2)=H1R-DATA(2)
      ELSE
        H1R=DATA(1)
        DATA(1)=C1*(H1R+DATA(2))
        DATA(2)=C1*(H1R-DATA(2))
        CALL FOUR1(DATA,N,-1)
      ENDIF
      RETURN
      END
C
C -----
C
      SUBROUTINE FOUR1(DATA,NN,ISIGN)
      REAL*8 WR,WI,WPR,WPI,WTEMP,THETA
      DIMENSION DATA(*)
      N=2*NN
      J=1
      DO 11 I=1,N,2
        IF(J.GT.I)THEN
          TEMPR=DATA(J)
          TEMPI=DATA(J+1)
          DATA(J)=DATA(I)
          DATA(J+1)=DATA(I+1)
          DATA(I)=TEMPR
          DATA(I+1)=TEMPI
        ENDIF
        M=N/2
1      IF ((M.GE.2).AND.(J.GT.M)) THEN
          J=J-M
          M=M/2
          GO TO 1
        ENDIF
        J=J+M
11     CONTINUE
      MMAX=2
2      IF (N.GT.MMAX) THEN
        ISTEP=2*MMAX
        THETA=6.28318530717959D0/(ISIGN*MMAX)
        WPR=-2.D0*DSIN(0.5D0*THETA)**2
        WPI=DSIN(THETA)
        WR=1.D0

```

```

      WI=0.D0
      DO 13 M=1,MMAX,2
        DO 12 I=M,N,ISTEP
          J=I+MMAX
          TEMPR=SNGL(WR)*DATA(J)-SNGL(WI)*DATA(J+1)
          TEMPI=SNGL(WR)*DATA(J+1)+SNGL(WI)*DATA(J)
          DATA(J)=DATA(I)-TEMPR
          DATA(J+1)=DATA(I+1)-TEMPI
          DATA(I)=DATA(I)+TEMPR
          DATA(I+1)=DATA(I+1)+TEMPI
12      CONTINUE
        WTEMP=WR
        WR=WR*WPR-WI*WPI+WR
        WI=WI*WPR+WTEMP*WPI+WI
13      CONTINUE
        MMAX=ISTEP
      GO TO 2
    ENDIF
  RETURN
END
c

```

This program uses a non-linear least squares fitting program to fit measured 2f data to a theoretical 2f spectrum
it requires subroutines from Appendix A

```

c ----- MAIN Program to call fitting simulator ----
c ----- version 1 June 16 1993 -----
c ----- q.v. nguyen
c
c
c
c      program fit
c      parameter(npam=14,ndata=5)
c      dimension lista(npam), a(npam)
c      dimension xdata(ndata),ydata(ndata),sigdata(ndata)
c      dimension covar(npam,npam),alpha(npam,npam)
c
c      open(1,file='fit.inp',status='unknown')
c      open(2,file='fit.dat',status='unknown')
c      open(3,file='mod.dat',status='unknown')
c
c --- input parameters from input file ---
c --- if parameter has a 1 preceeding then it is an adjustable parameter
c --- if preceeded by 0 then it is not adjustable and is fixed
c
c      ii = 0
c      do 10 i=1,npam
c        read(1,*) iflag, a(i)
c        if(iflag.eq.1) then
c          ii = ii + 1
c
c
c --- load array lista with parameters to be varied ----
c
c      lista(ii) = i
c      endif
10    continue
c      read(1,*) tol
c

```

```

c --- store number of parameters to be fitted ---
c
c     mfit = ii
c
c --- load data to be fitted ----
c
c     do 12 i=1,ndata
c       read(3,*) xdata(i), ydata(i), sigdata(i)
12    continue
c
c --- initialize Levinberg-Marquardt non-linear least squares algorithm
c
c     alamda = -1.0
c
c --- call algorithm ---
c
c     write(*,*) 'starting'
c     nca = mfit
c     chiold = 10.0
900    call MRQMIN(xdata,ydata,sigdata,ndata,a,nparam,lista
c      &          ,mfit,covar,alpha,nca,chisq,alamda)
c
c --- check for convergence ----
c
c     diff = abs(chisq-chiold)
c     if (diff.le.tol) then
c
c --- convergence ---
c
c     write(*,*) ' Success ! '
c     goto 999
c
c     else
c
c --- try again ----
c
c     jj = jj + 1
c     write(*,*) ' try again ', jj
c     chiold = chisq
c     goto 900
c
c     endif
c
c ---- success!
c ---- call MRQMIN one last time with alamda = 0 to return
c ---- covariance and curvature matrix
c
999    alamda = 0.0
c     call MRQMIN(xdata,ydata,sigdata,ndata,a,nparam,lista
c      &          ,mfit,covar,alpha,nca,chisq,alamda)
c
c
c --- output data ---
c
c     do 200 i=1,nparam
c       write(2,*) a(i)
200    continue
c
c     close(1)
c     close(2)
c     close(3)

```

```

        stop
        end
c
c
c
c --- subroutine to evaluate fit and derivatives ---
c
c --- lista is an array which orders the first mfit elements
c --- of the parameter array as the variable params, the
c --- elements in array a(i) following mfit are held stationary
c
        subroutine funcs(x,a,y,dyda,nparam,lista,mfit)
        dimension lista(nparam)
        real a(nparam), dyda(nparam)
c        write(*,*) 'call funcs'
c
c --- calculate y ---
c
        call mods(x,a,yout)
        y = yout
c
c --- calculate derivatives ---
c --- only first mfit parameters need derivatives ---
c
c
        do 100 j=1,mfit
c
c --- take left value as central value minus a fraction ---
c --- set fraction at 1%
c
        fract = 0.01
        aleft = a(lista(j))*(1.0-fract)
c
c -- save original parameter --
c
        aold = a(lista(j))
        a(lista(j)) = aleft
        call mods(x,a,yout)
c
c --- reset with original ---
c
        a(lista(j)) = aold
        yleft = yout
c
c --- right value as central value plus a fraction ---
c
        aright = a(lista(j))*(1.0+fract)
        a(lista(j)) = aright
        call mods(x,a,yout)
        a(lista(j)) = aold
        yright = yout
c
c --- compute central value ---
c
        call mods(x,a,yout)
        ycenter = yout
c
c ---- take central difference ----
c
        deltaa = aright - aleft
        dyda(lista(j)) = (0.25*yleft+0.5*ycenter+0.25*yright)/deltaa

```

```

100    continue
c
c
c      RETURN
c      END
c
c
c
c
c ---- actual evaluation of 2f signal using fft ---
c
c
c      subroutine mods(x,a,y)
c      parameter (n=128,isign=1,nparam=14)
c
c      double precision WL1
c      real fj(n), plaser(n),a(nparam)
c      dimension lista(nparam)
c
c ---- load list of variables into physical names ---
c
c      pcol = a(1)
c      scale = a(2)
c      w1 = a(3)
c      T1 = a(4)
c      amod = a(5)
c      V1 = a(6)
c      V2 = a(7)
c      vmod = a(8)
c      NNV = a(9)
c      NNJ = a(10)
c      NB = a(11)
c      XL1 = a(12)
c      P1 = a(13)
c      width = a(14)
c
c ---- constants ---
c
c      Sfund = 283.0 ! Varghese and hanson
c      pi = 4.0*atan(1.0)
c
c
c      if(NB.eq.1) NBG = 1
c      if(NB.eq.-1) NBG = 0
c
c ---- account for variation in collisional width with J and T ---
c ---- from Varghese and Hanson (A linear function in J) ---
c ---- width is proportional to pressure in atm -----
c
c      dwcnum1 = -0.000226*float(NNJ+NBG)+0.042*sqrt(1850/T1)
c
c ---- calc line position and strength ---
c
c      call colst(T1,NNV,NNJ,NB,SL1,WL1)
c      wnum1 = WL1
c
c ---- calc doppler width ---
c
c      dopnum1 = 7.16e-7*sqrt(T1/28.0)*wnum1
c

```

```

c ---  calc voigt parameters  ---
c
      anum1 = 0.83255*dwcn1/dopnum1*P1
c
c --- calc laser power - a linear variation ---
c
      xleft = w1-0.5*width
      slope = (v2-v1)/width
      vlaser = (x-xleft)*slope + v1
c
c --- calculate time series ----
c
      do 200 j=1,n
        time = float(j-1)/float(n)
        xmod = sin(2.0*pi*time)
        wj = amod * xmod + x - w1
c
c --- call voigt profile at x and param --
c
        x1 = abs(1.6651*wj/dopnum1)
        Vnum1 = VOIGT(x1,anum1)
c
c --- Lineshapes calc from Voigt with collisional width ---
c
        G1 = 0.9394*Vnum1/dopnum1
c
c --- add laser power modulation ---
c
        plaser(j) = vlaser + xmod*vmod
c
c --- now use Beer's Law ---
c
        fj1 = -sfund*SL1*G1*XL1*(Pcol*1e-6)
c
        fj(j) = plaser(j)*exp(fj1)
c
c --- return loop for time modulation ---
c
200      continue
c
c ---- call fast fourier transform ---
c ---- the time series is then converted to frequency domain ----
c
      nin = n/2
      call realft(fj,nin,isign)
c
c --- calc and normalize desired fourier coefs of interest ---
c --- the 5th term is the real part of the 2nd harmonic of the fourier
c --- coef. and is equal to the 2f signal resulting from the lock-in
c
c
      xnrm = 1.0/float(n)
      y = -fj(5)*xnrm*scale
c
c
      RETURN
      END

```

Appendix D

Raman Data Reduction Procedure

The Raman signals were calibrated with an extensive set of flames operating over a wide range of equivalence ratios with various fuels. The following calibration cases were used to cover the range of molecules and temperatures of interest. In all, over 100 different conditions were used to calibrate the response of the Raman system. Thus the Raman measurements are completely empirically determined.

1. Cold air (both wet and dry) provided the calibration factors for: cold N_2 , cold O_2 , cold H_2O and the crosstalk of cold N_2 onto CO (denoted by $\text{N}_2 \rightarrow \text{CO}$), and cold $\text{O}_2 \rightarrow \text{CO}_2$.
2. Cold H_2 in air provided factors for cold H_2 and cold $\text{H}_2 \rightarrow \text{CO}_2$.
3. Cold CO in air provided the factors for cold CO.
4. The lean H_2 -air flames provided hot $\text{N}_2 \rightarrow \text{CO}$.
5. The rich H_2 -air flames provided hot N_2 , hot H_2 , hot H_2O , hot $\text{H}_2 \rightarrow \text{CO}_2$, and hot $\text{H}_2 \rightarrow \text{CO}$.
6. The various H_2 -CO-air flames provided hot CO_2 , hot $\text{CO}_2 \rightarrow \text{O}_2$, and hot CO.
7. The cold CH_4 -air provided cold CH_4 , $\text{CH}_4 \rightarrow \text{O}_2$, $\text{CH}_4 \rightarrow \text{CO}_2$.

8. The CH₄-air flames then provide a separate redundant check of the above calibrations.

The Raman data point consists of a vector of 11 values (N₂, O₂, H₂, H₂O, CO₂, CO, CH₄, F₁, F₂, F₃, E) where F_X refers to the fluorescence interference monitoring channels, and E is the laser power. Only the F₂ fluorescence channel is used, thus after the Raman data is normalized by the laser energy E at each point, the data point S_i is given by the vector

$$S_i = \begin{pmatrix} N_2 \\ O_2 \\ H_2 \\ H_2O \\ CO_2 \\ CO \\ CH_4 \\ F_2 \end{pmatrix} \quad (D.1)$$

The raman scattered signal is a function of the laser energy E , the calibration constants $k_{ij}(T)$ which are temperature dependent, and the number density N_j . The Raman signal can thus be described by

$$S_i = E \sum_j k_{ij}(T) N_j, \quad (D.2)$$

where, $k_{ij}(T)$ is the temperature dependent calibration constants which are determined by plotting the Raman response normalized by the number density N_j for each channel i as a function of temperature. The behavior of the Raman response is a function of all factors including: the Boltzmann distribution, the spectral lineshape of both the laser and the molecules being probed, the instrumental function, the collection efficiency, the spectral overlap or crosstalk, etc.

Table D.1 : Calibration constants for Raman data reduction.

i	j	Kij	Curve	Const	Linear	Quad	Cubic	a	b	c
1	1	N2	Quad	7.698E-02	2.282E-05	-7.982E-09	0.000E+00	0.000	0.000	0.000
2	2	O2	Linear	1.087E-01	1.159E-05	0.000E+00	0.000E+00	0.000	0.000	0.000
3	3	H2	Linear	8.576E-01	-2.321E-04	0.000E+00	0.000E+00	0.000	0.000	0.000
4	4	H2O	Cubic	1.250E-01	1.098E-03	-7.033E-07	1.207E-10	0.000	0.000	0.000
5	5	CO2	Linear	1.649E+00	-2.860E-04	0.000E+00	0.000E+00	0.000	0.000	0.000
6	6	CO	Linear	5.502E-01	1.275E-05	0.000E+00	0.000E+00	0.000	0.000	0.000
5	3	H2-->CO2	Linear	3.308E-02	3.221E-05	0.000E+00	0.000E+00	0.000	0.000	0.000
5	2	O2-->CO2	linear*(1+a* exp(b*(x-c)))	-6.282E-03	4.582E-05	0.000E+00	0.000E+00	0.095	0.0043	1500
2	3	H2-->O2	Linear	-5.512E-04	1.837E-06	0.000E+00	0.000E+00	0.000	0.000	0.000
2	5	CO2-->O2	Linear	4.121E-02	-6.450E-06	0.000E+00	0.000E+00	0.000	0.000	0.000
6	1	N2-->CO	Linear	6.098E-04	9.355E-06	0.000E+00	0.000E+00	0.000	0.000	0.000
6	3	H2-->CO	Linear	-4.557E-02	4.557E-05	0.000E+00	0.000E+00	0.000	0.000	0.000
7	7	CH4	Constant	2.625E-01	0.000E+00	0.000E+00	0.000E+00	0.000	0.000	0.000
2	7	CH4-->O2	Constant	1.541E-02	0.000E+00	0.000E+00	0.000E+00	0.000	0.000	0.000
5	7	CH4-->CO2	Constant	2.151E-02	0.000E+00	0.000E+00	0.000E+00	0.000	0.000	0.000
6	8	F615-->CO	Constant	1.970E+00	0.000E+00	0.000E+00	0.000E+00	0.000	0.000	0.000

After determining what analytical form of a fitting function best describes each of the Raman responses, a matrix of calibration constants is determined. The temperature dependent calibration constants k_{ij} used for reducing the Raman data are given in Table D.1.

The calculation of a number density in the actual experiment is accomplished by solving Eq. (D.2) for N_j . This results in the following expression

$$N_i = \frac{1}{E} \dot{\mathbf{a}}_j k_{ij}^{-1}(T) S_i \quad . \quad (\text{D.3})$$

Thus by inverting the matrix k_{ij} and multiplying it with the normalized vector S_i , the number densities N_j are obtained. A guessed temperature has to be used to calculate an initial value of k_{ij} which is then iterated upon. Once the number densities are calculated using Eq. (D.3), the temperature can be calculated using the perfect gas law. Since we have an additional measurement of Rayleigh scattering, the Raman measurements are used to determine the overall Rayleigh scattering cross section given by a mole fraction weighted average. The temperature is then calculated using the overall Rayleigh scattering cross section and Rayleigh scattering signal. This new temperature is then used to calculate a new k_{ij} . Typically, 4 to 5 iterations are required for convergence. The Raman data reduction was performed using a spreadsheet program (Quattro Pro for Windows Version 5.0) which provided a tremendous ability to visualize the calibrations in real-time. The spreadsheet facilitated the answering of many ‘what if?’ questions, which in the end, provide an accurate calibration of the Raman system. In the past, the calibrations and calculations were performed using FORTRAN codes which were rather tedious and unflexible. A more detailed description of the Raman calibration procedure can be found in Smith (1994).

Appendix E

OH and NO LIF Data Reduction Codes

These are the FORTRAN codes used to reduce the LIF data into quantitative values. The program RNO1.FOR calculates the overall collisional electronic quenching corrections for OH and NO by various colliders found in combustion products. The results of the Raman data reduction provide the input necessary for performing the quenching corrections. This program also has routines that calculate the Boltzmann fractions for OH and NO. There is also a subroutine that convolves the laser and absorption lineshapes. Most of these subroutines were graciously provided by Drs. Cam D. Carter, Phil Paul, and Robert Barlow.

Included are the input files that initialize the calibration parameters for the OH and NO calculations. Following the FORTRAN codes is an example of the output file that RNO1.FOR generates (the reduced data which is then plotted).

These were the typical input startup files required for RNO1.FOR

```
!Calibration File for OH dayfile 60011 CH4-Air Hencken Burner running at phi =
0.948 Air = 59.8 slm CH4 = 5.954
13 8.540E-02      !CO2
10 1.260E-02      !O2
8 0.000E-03       !CO
11 7.168E-01      !N2
14 1.799E-01      !H2O
9 5.300E-03       !H2
6 0.000E-04       !H
7 0.000E-04       !O
7.5              !jexct = NR - 1/2 for ispin = 2
2                !ispin
2180.4           !T_REF (rayleigh temp)
250              !OH_SIGNAL
2.962E-03        !OH_EQUIL      ! mole fraction of OH in cal flame
```

```
!Calibration File for NO dayfile 60025 CH4-Air McKenna Burner running at phi =
0.887 N2 = 11.55 O2 = 4.00 CH4 = 1.447
4.2600E-02      !O2      raman
2.9430E-05      !O       equil
1.0950E-03      !OH      from measurement of dayfile 60025
```

```

3.0970E-06  !H      equil
1.7830E-01  !H2O    raman
6.9580E-01  !N2     raman
8.3200E-02  !CO2    raman
1.0220E-04  !CO     from equil
18.5        !jexct   Q_1(18) transition
1          !ispin
1790.0      !T_REF    rayleigh-raman 1821
1028        !NO_SIGNAL (difference from dope vs no dope NO)
30.4E-06    !NO_DOPED INTO FLAME = 30.4 ppm

```

This is the main program RNO1.FOR

```

c $$$$$$$$$$ BEGIN MAIN PROGRAM $$$$$$$$$$$$$$
c
c
c ----- program to convert OH and NO data from TDF measurements -----
c           taken in april of 1994, for Bunsen Flames
c
c           Quang-Viet Nguyen
c           November 13, 1994
c           version 2.1
c
c
c           PROGRAM RNO1
c
c
c ---- define variables for OH section ----
c
c           real x,p,sigma,grate_oh,jexct_oh,ram_dat(18,100),xcal_oh(12)
c           real sig_oh,tref_oh,x_oh_ref,q_oh_ref,fb_oh_ref,press
c           real q_meas,oh_meas(100),temp,oh_ref,ppm_oh(100),nd_oh(100)
c
c
c --- define variables for NO section ----
c
c           real x_no_cal(8),q_no_meas,x_no_q(8),fb_no_meas
c           real jexct_no,tref_no,no_sig_ref,no_x_ref,fb_no_ref
c           real k,q_no_ref,no_ref,ppm_no(100),no_meas(100)
c           real nd_no(100)
c
c
c --- integer definitions ----
c
c           integer ispec,iflag,ical,itype(12),ispin
c
c
c --- character definitions -----
c
c           character*8 minp
c           character*20 dayfile(100)
c           character*12 filein

```

```

data press/1.00/

c
c --- enter name of file to process -----
c

      write(*,*) ' enter name of file to process : '
      read(*,*) filein
      write(*,*) ' enter the number of data points in file (<100) : '
      read(*,*) npoints

c
c ---- input data file to be processed (from Raman reduction) -----
c

      open(3,file=filein,status='old')
      read(3,*)
      do 100 j=1,npoints
        read(3,*) dayfile(j),(ram_dat(i,j),i=1,18)
100    continue

      close(3)

c
c ---- input calibration file for OH ---
c

      open(1,file='caloh.inp',status='old')

      ical = 8

      read(1,*)

c
      do 155 k=1,ical
        read(1,*) itype(k), xcal_oh(k)
155    continue

      read(1,*) jexct_oh
      read(1,*) ispin
      read(1,*) tref_oh
      read(1,*) sig_oh          !OH-signal/OH-laser*1000
      read(1,*) x_oh_ref

      close(1)

c
c --- input calibration file for NO -----
c

      open(7,file='calno.inp',status='old')

      read(7,*)

      do 10 i=1,8
        read(7,*) x_no_cal(i)
10    continue

      read(7,*) jexct_no
      read(7,*) ispin_no

```

```

      read(7,*) tref_no
      read(7,*) no_sig_ref          ! NO-signal/NO-laser*1000
      read(7,*) no_x_ref            ! NO concentration from calib.

      close(7)

c
c --- open output data files ----
c

      open(2,file='test.out',status='unknown',recl=210)
      open(4,file='rno2.out',status='unknown',recl=210)

c
c --- write data file headers for test.out - for debugging purposes ---
c

      write(2,*) '; data for input file ',filein
      write(2,444)
      write(4,*) '; data for input file ',filein
      write(4,445)

444   format(';dayfile, T, N2, O2, H2, H2O, CO2, CO, CH4, OH, NO')
445   format(';L, T, N2, O2, H2, H2O, CO2, COx10, CH4, OHx100,NOx10000')

c
c ---- calculate quench rate of reference condition for OH ----
c

      q_oh_ref = 0.0

      do 400 k=1,ical
          call qoh(minp,itype(k),xcal_oh(k),tref_oh,press,
&              sigma,qrate_oh,iflag)
          if(iflag.eq.4) goto 1111
          q_oh_ref = q_oh_ref + qrate_oh
400   continue

      write(2,*) 'q_oh_ref = ',q_oh_ref

c
c ---- calculate the Boltzmann fraction of the ref condition for OH ----
c

      call fboh(tref_oh,jexct_oh,ispin,fb)
      fb_oh_ref = fb

      write(2,*) 'fb_oh_ref = ',fb_oh_ref

c
c -- calc number density of OH in reference --
c

      oh_ref = x_oh_ref * 40.622 * 300.0 / tref_oh

      write(2,*) ' oh_ref_nd (cm-3) = ', oh_ref*2.69E19/40.622

c
c -- calc number density in NO reference ---

```

```

c
    no_ref = no_x_ref * 40.622 * 300.0 / tref_no
    write(2,*) ' no_ref_nd (cm-3) = ',no_ref*2.69E19/40.622

c
c ---- calculate Calibration Boltzmann Fraction for NO ref flame ----
c
    call fb_no(tref_no,ispin_no,jexct_no,fb_no_ref)
    write(2,*) 'fb_no_ref = ',fb_no_ref

c
c ---- calculate Quench rate for NO in ref flame -----
c
    call quench_no(x_no_cal,tref_no,press,q_no_ref)
    write(2,*) 'q_no_ref = ', q_no_ref

c
c ---- calculate the spectral overlap integral for laser and absorption ---
c
    freq = 44267.4          ! 225.9 nm in cm-1
    dtune = 0.0             ! detuning from line center in cm-1
    dlas = 0.60             ! laser linewidth in cm-1
    t = tref_no
    call ovrlap(t, freq, dtune, dlas, cp)
    cp_ref = cp

c
c --- loop for all j points in data set ----
c
    p = press
    do 1000 j = 1, npoints

c
c --- write data point number to screen ----
c
    write(*,*) ' processing data point ',j
    temp = ram_dat(1,j)
    qsum_oh = 0.0

c N2
    ispec = 11
    x = ram_dat(2,j)
    call qoh(minp,ispec,x,temp,p,sigma,qrate_oh,iflag)
    if(iflag.eq.4) goto 1111
    qsum_oh = qsum_oh + qrate_oh

c O2
    ispec = 10

```



```

x = ram_dat(3,j)
call qoh(minp,ispec,x,temp,p,sigma,qrate_oh,iflag)
    if(iflag.eq.4) goto 1111
    qsum_oh = qsum_oh + qrate_oh

c H2

ispec = 9
x = ram_dat(4,j)
call qoh(minp,ispec,x,temp,p,sigma,qrate_oh,iflag)
    if(iflag.eq.4) goto 1111
    qsum_oh = qsum_oh + qrate_oh

c H2O

ispec = 14
x = ram_dat(5,j)
call qoh(minp,ispec,x,temp,p,sigma,qrate_oh,iflag)
    if(iflag.eq.4) goto 1111
    qsum_oh = qsum_oh + qrate_oh

c CO2

ispec = 13
x = ram_dat(6,j)
call qoh(minp,ispec,x,temp,p,sigma,qrate_oh,iflag)
    if(iflag.eq.4) goto 1111
    qsum_oh = qsum_oh + qrate_oh

c CO

ispec = 8
x = ram_dat(7,j)
call qoh(minp,ispec,x,temp,p,sigma,qrate_oh,iflag)
    if(iflag.eq.4) goto 1111
    qsum_oh = qsum_oh + qrate_oh

c CH4

ispec = 30
x = ram_dat(8,j)
call qoh(minp,ispec,x,temp,p,sigma,qrate_oh,iflag)
    if(iflag.eq.4) goto 1111
    qsum_oh = qsum_oh + qrate_oh
    q_meas = qsum_oh

c
c ---- calculate Boltzmann fraction for OH -----
c

    call fboh(temp,jexct_oh,ispin,fb)
    fb_oh_meas = fb

c
c ---- calc quenching ratio for OH ----
c

    qratio_oh = q_meas/q_oh_ref

c

```

```

c --- calc Boltzmann ratio for OH ---
c
      fbratio_oh = fb_oh_ref/fb_oh_meas

c
c --- calc OH signal/ OH ref signal -----
c
c --- check to see if OH laser is on ----
c
c      also
c
c --- check to see if any OH exists ie., has to be hot ----
c
      if(temp.gt.450.0) then
          sigratio_oh = ram_dat(11,j)/sig_oh
      else
          sigratio_oh = 0.0
      endif

c
c ---- calculate OH in measurement in moles/meter^3 ----
c
      oh_meas(j) = sigratio_oh * fbratio_oh * qratio_oh * oh_ref

c
c --- calculate OH mole fraction ----
c
      ppm_oh(j) = oh_meas(j) / 40.622 * temp / 300.0

c
c --- number dens of OH in molecules/cm^3 -----
c
      nd_oh(j) = oh_meas(j) / 40.622 * 2.69E19

c
c ---- now calculate NO in measurement using OH obtained above ---
c
c --- calculate Boltzmann fraction for NO at temp ---
c
      call fb_no(temp,spin_no,jexct_no,fb_no_meas)

c
c      now load data from ram_dat(i,j) into x_no_q(i) for the
c      quencher array that needs to be loaded into the NO quench subroutine
c
      x_no_q(1) = ram_dat(3,j)      ! O2

c
c --- estimate H and O atom population from equilibrium
c
c --- the effect of H and O atom on the resultant NO was minimal,
c      since there was no effect on the NO when the H and O molefractions
c      on the no calibration flame file was set to zero.

```

```

c      We can neglect the effect of O and H atom quenching in the Bunsen
c      flames.
c
      x_no_q(2) = 0.0                ! set O = 0 for now
      x_no_q(3) = ppm_oh(j)          ! OH from above
      x_no_q(4) = 0.0                ! set H = 0 for now
      x_no_q(5) = ram_dat(5,j)       ! H2O
      x_no_q(6) = ram_dat(2,j)       ! N2
      x_no_q(7) = ram_dat(6,j)       ! CO2
      x_no_q(8) = ram_dat(7,j)       ! CO

c --- note CH4 doesn't quench NO so it is not included ---
      call quench_no(x_no_q,temp,press,q_no_meas)

c
c --- calc Boltzmann ratio for NO ----
c
      fbratio_no = fb_no_ref / fb_no_meas

c
c --- calc Quench Ratio for NO ---
c
      qratio_no = q_no_meas / q_no_ref

c
c --- calc Signal Ratio for NO ---
c
      sigratio_no = no_ref / no_sig_ref

c
c --- calc overlap integral ----
c
      call ovrlap(temp, freq, dtune, dlas, cp)
      cp_meas = cp

c
c --- calc Number density of NO in measurement (moles/meter^3) ---
c
      no_meas(j) = ram_dat(14,j) * sigratio_no * fbratio_no *
&                qratio_no * cp_ref / cp_meas

c
c --- calculate number density of NO in (molecule/cm-3) ---
c
      nd_no(j) = no_meas(j) * 2.69E19 / 40.622

c
c --- calculate mole fraction of NO in flame ----
c
      ppm_no(j) = no_meas(j) / 40.622 * temp / 300.0

c

```

```

c ---- display results of OH and NO number density ----
c
      write(2,202) dayfile(j),(ram_dat(i,j),i=1,8),nd_oh(j)
      &      ,nd_no(j),ram_dat(18,j)

c --- expand OH scale by factor of 100 for plotting purposes ---
c --- expand NO scale by factor of 10000 for plotting purposes ---
c --- expand CO scale by factor of 10 for plotting purposes ---

      write(4,203) ram_dat(18,j),(ram_dat(i,j),i=1,6),
      & ram_dat(7,j)*10.0,ram_dat(8,j),
      & ppm_oh(j)*100.0,ppm_no(j)*10000.0

202  format(a20,f7.1,1x,10(1pe9.3,1x))
203  format(f6.1,1x,f7.1,1x,9(1pe9.3,1x))

1000 continue

      close(2)
      close(4)

      write(*,*) ' Output written to file rno1.out and test.out '

      stop

c
c ---- notify in case of error with quench ----
c

1111 write(*,*) ' ERROR with Quench Code ispec=',ispec

      stop

      END

c
c $$$$$$$$$$ END OF MAIN PROGRAM $$$$$$$$$$
c

c ----- subroutines follow -----
c
c These routines were provided by Cam Carter, SRL, Inc. Dayton OH.
c and Phil H. Paul, Sandia National Laboratories.
c
c $$$$$$$$$$ Calculate OH Boltzmann Fraction $$$$$$$$$$
c
      SUBROUTINE fboh(T,jexct,ispin,fb)

c*****
c
c Purpose: calculate the Boltzmann fraction for the J-th state
c          of the OH X(v=0) state
c Inputs:  jexct  the J quantum number:
c          a) for ispin=1, J = N + 1/2
c          b) for ispin=2, J = N - 1/2
c          ispin  the spin state (1 or 2)
c          t      the temperature (K)
c

```

```

c      Enter the constants
c*****

      REAL j1, j2, jexct

      data Bv/18.531/,Dv/1.9287E-3/,Yv/-7.4966/,we/3735.2/,wexe/82.2/

c      Plank      , speed of light,      Boltzmann

      g = 6.626196e-27 * 2.9979250e+10 / 1.380622e-16

c*****
c      Find the rotational partition function
c*****

      qr = 0.0
      do 50 i=1,50
        j1 = float(i) + 0.5
        f1 = Bv*((j1+0.5)**2 + 1.0 -
&          0.5*(SQRT((2.0*j1+1.0)**2 + Yv*(Yv-4.0)))) -
&          Dv * (j1-0.5)**2 * (j1+0.5)**2

        if((ispin .eq. 1) .and. (jexct .eq. j1)) fexct = f1

        j2 = float(i) - 0.5
        f2 = Bv*((j2+0.5)**2 + 1.0 +
&          0.5*(SQRT((2.0*j2+1.0)**2 + Yv*(Yv-4.0)))) -
&          Dv * (j2+0.5)**2 * (j2+1.5)**2

        if((ispin .eq. 2) .and. (jexct .eq. j2)) fexct = f2

        qr = qr + (2.0*j1 + 1.0)*exp(-g*f1/t) +
&          (2.0*j2 + 1.0)*exp(-g*f2/t)
50      continue

c*****
c      Find the vibrational partition function
c*****

      qv = 0.0
      DO 100 i=1,10
        v = float(i - 1)
        Gv = we*(v + 0.5) - wexe*(v + 0.5)**2.
        qv = qv + exp(-Gv*g/t)
100      CONTINUE

c*****
c      Set the electronic partition function to '2', for the
c      lambda doubling in the ground state; this is valid for small
c      lambda doubling.
c*****

      qe = 2.0

      etot = fexct + 0.5*we - 0.25*wexe
      fb   = (2.0*jexct + 1.0) * exp(-g*etot/t)/(qe * qv * qr)

c
      RETURN
      END

c

```

```

c ***** calculate Quenching rate and Cross section *****
c
c      block data
c*****
c      This contains the data arrays describing electronic quenching of
c      the A state (v'=0) of hydroxyl (OH).
c-----
c      Parameters:
c
c      Wtprt(i) = molecular (atomic) weight of species i
c      info(i)  = information array for species i
c               = 0 when the probability 'P' is base on experimental
c                 collisional cross sections
c               = 1 when the probability 'P' equals 1 (no experimental
c                 results are available)
c               = 2 when the model gives 'P' of 0.0 (the harpooned
c                 cross section is identically zero)
c      tmax     = maximum recommended temperature for model (K)
c      tmin     = minimum recommended temperature for model (K)
c      tref     = reference temperature for calculations (K)
c      c(i,1)   = P (see paper)
c      c(i,2)   = c0
c      c(i,3)   = c1
c      c(i,4)   = c2
c      c(i,5)   = alpha
c      For the species that are nonquenchers (e.g., He), set c0,c1,c2,
c      and alpha to 1.0 (so that they are nonzero); set P to 0.0
c*****

      parameter (ndim=42)
      dimension c(ndim,5), Wtprt(ndim), info(ndim), molec(ndim)
      common /param/ nspec, molec, Wtprt, info, c, tmin, tmax, tref
      common /error/ itmax, eps
      character molec*8
      data nspec/42/, tmin/250.0/, tmax/2500.0/, tref/300.0/
c-----
c      Define parameters for the Gamma function routines; these
c      values are passed to the functions through named common 'error'
c-----
      data itmax/500/, eps/3.0e-07/

c---1--- Helium
      data molec(1) /'he'/, Wtprt(1) /4.003/, info(1)/2/
      data (c(1,j),j=1,5) /0.0, 4*1.0/

c---2--- Neon
      data molec(2) /'ne'/, Wtprt(2) /20.17/, info(2)/2/
      data (c(2,j),j=1,5) /0.0, 4*1.0/

c---3--- Argon
      data molec(3) /'ar'/, Wtprt(3) /39.95/, info(3)/2/
      data (c(3,j),j=1,5) /0.0, 4*1.0/

c---4--- Krypton
      data molec(4) /'kr'/, Wtprt(4) /83.80/, info(4)/0/
      data (c(4,j),j=1,5) /0.238,14.641,1.501,5.572,6.00/

c---5--- Xenon
      data molec(5) /'xe'/, Wtprt(5) /131.3/, info(5)/0/
      data (c(5,j),j=1,5) /0.698,18.686,1.515,4.013,6.00/

```

```

c---6--- Hydrogen (atomic)
  data molec(6) /'h'/, Wtprt(6) /1.008/, info(6)/0/
  data (c(6,j),j=1,5) /1.038,13.763,1.347,1.399,4.00/

c---7--- Oxygen (atomic)
  data molec(7) /'o'/, Wtprt(7) /16.00/, info(7)/1/
  data (c(7,j),j=1,5) /1.000,13.959,1.452,2.067,5.20/

c---8--- Carbon Monoxide
  data molec(8) /'co'/, Wtprt(8) /28.01/, info(8)/0/
  data (c(8,j),j=1,5) /0.846,14.536,1.664,6.206,4.60/

c---9--- Hydrogen (molecular)
  data molec(9) /'h2'/, Wtprt(9) /2.016/, info(9)/0/
  data (c(9,j),j=1,5) /0.330,12.848,1.360,3.079,3.50/

c--10--- Oxygen (molecular)
  data molec(10) /'o2'/, Wtprt(10) /32.00/, info(10)/0/
  data (c(10,j),j=1,5) /0.537,14.892,1.327,3.866,3.95/

c--11--- Nitrogen
c N2 revised values from SAND 94-8244 by Phil paul
c latest values for N2 -- a finite quencher
  data molec(11) /'n2'/, Wtprt(11) /28.01/, info(11)/0/
  data (c(11,j),j=1,5) /0.351,1.000,1.800,1.900,1.300/

c--12--- Nitric Oxide
  data molec(12) /'no'/, Wtprt(12) /30.01/, info(12)/0/
  data (c(12,j),j=1,5) /1.003,27.157,1.800,1.269,3.90/

c--13--- Carbon Dioxide
  data molec(13) /'co2'/, Wtprt(13) /44.01/, info(13)/0/
  data (c(13,j),j=1,5) /0.770,15.418,1.391,8.205,3.22/

c--14--- Water vapor
  data molec(14) /'h2o'/, Wtprt(14) /18.015/, info(14)/0/
  data (c(14,j),j=1,5) /1.120,15.955,2.251,4.302,3.12/

c--15--- Nitrous Oxide
  data molec(15) /'n2o'/, Wtprt(15) /44.01/, info(15)/0/
  data (c(15,j),j=1,5) /1.026,16.490,1.677,6.815,4.60/

c--16--- Amonia
  data molec(16) /'nh3'/, Wtprt(16) /17.03/, info(16)/0/
  data (c(16,j),j=1,5) /1.285,30.244,2.632,1.320,3.90/

c--17--- Carbon tetra-flouride
  data molec(17) /'cf4'/, Wtprt(17) /88.00/, info(17)/2/
  data (c(17,j),j=1,5) /0.0, 4*1.0/

c--18--- Carbon tetra-chloride
  data molec(18) /'ccl4'/, Wtprt(18) /153.8/, info(18)/0/
  data (c(18,j),j=1,5) /1.973,26.676,0.820,3.760,2.400/

c--19--- Sulfur Hexafluoride
  data molec(19) /'sf6'/, Wtprt(19) /146.1/, info(19)/2/
  data (c(19,j),j=1,5) /0.0, 4*1.0/

c--20--- Hydrogen Fluoride
  data molec(20) /'hf'/, Wtprt(20) /20.01/, info(20)/1/
  data (c(20,j),j=1,5) /1.000,12.140,2.010,13.226,3.210/

```

```

c--21--- Hydrogen Chloride
      data molec(21) /'hcl'/, Wtprt(21) /36.46/, info(21)/0/
      data (c(21,j),j=1,5) /0.858,16.347,1.771,8.558,3.210/

c--22--- Hydrogen Bromide
      data molec(22) /'hbr'/, Wtprt(22) /80.91/, info(22)/1/
      data (c(22,j),j=1,5) /1.000,19.651,1.680,6.044,3.210/

c--23--- Bromine (molecular)
      data molec(23) /'br2'/, Wtprt(23) /159.8/, info(23)/1/
      data (c(23,j),j=1,5) /1.000,26.547,1.710,3.704,4.600/

c--24---
      data molec(24) /'cf3h'/, Wtprt(24) /70.01/, info(24)/0/
      data (c(24,j),j=1,5) /0.342,21.632,2.171,2.279,3.215/

c--25---
      data molec(25) /'cf3br'/, Wtprt(25) /148.9/, info(25)/1/
      data (c(25,j),j=1,5) /1.000,18.169,1.622,7.528,4.300/

c--26---
      data molec(26) /'ch3br'/, Wtprt(26) /94.94/, info(26)/1/
      data (c(26,j),j=1,5) /1.000,26.651,2.076,1.999,3.150/

c--27---
      data molec(27) /'cf2cl2'/, Wtprt(27) /120.9/, info(27)/0/
      data (c(27,j),j=1,5) /1.388,21.995,1.572,4.590,4.250/

c--28---
      data molec(28) /'c2clf3'/, Wtprt(28) /116.5/, info(28)/0/
      data (c(28,j),j=1,5) /3.339,29.179,0.876,1.009,4.05/

c--29---
      data molec(29) /'c2f6'/, Wtprt(29) /138.0/, info(29)/2/
      data (c(29,j),j=1,5) /0.0, 4*1.0/

c--30--- Methane
      data molec(30) /'ch4'/, Wtprt(30) /16.04/, info(30)/0/
      data (c(30,j),j=1,5) /0.826,16.561,1.109,3.591,3.050/

c--31--- Acetylene
      data molec(31) /'c2h2'/, Wtprt(31) /26.04/, info(31)/0/
      data (c(31,j),j=1,5) /1.620,20.267,1.656,3.866,4.510/

c--32--- Ethylene
      data molec(32) /'c2h4'/, Wtprt(32) /28.05/, info(32)/0/
      data (c(32,j),j=1,5) /1.809,23.769,0.833,2.706,2.205/

c--33--- Ethane
      data molec(33) /'c2h6'/, Wtprt(33) /30.07/, info(33)/0/
      data (c(33,j),j=1,5) /1.560,17.210,1.083,6.070,3.105/

c--34--- Propylene
      data molec(34) /'c3h6'/, Wtprt(34) /42.08/, info(34)/0/
      data (c(34,j),j=1,5) /1.850,32.362,1.716,1.291,4.405/

c--35--- 1-Butene
      data molec(35) /'1-c4h8'/, Wtprt(35) /56.11/, info(35)/0/
      data (c(35,j),j=1,5) /2.641,35.620,1.558,1.446,4.400/

```



```

c--36--- trans-Butene
      data molec(36) /'t-c4h8'/, Wtprt(36) /56.11/, info(36)/0/
      data (c(36,j),j=1,5) /3.066,41.694,1.397,0.816,4.400/

c--37--- iso-Butene
      data molec(37) /'i-c4h8'/, Wtprt(37) /56.11/, info(37)/0/
      data (c(37,j),j=1,5) /2.172,40.186,1.756,1.051,4.400/

c--38--- n-Butane
      data molec(38) /'n-c4h10'/, Wtprt(38) /58.12/, info(38)/0/
      data (c(38,j),j=1,5) /1.583,27.788,1.747,2.343,4.400/

c--39--- iso-Butane
      data molec(39) /'i-c4h10'/, Wtprt(39) /58.12/, info(39)/0/
      data (c(39,j),j=1,5) /1.660,28.093,1.515,2.818,4.800/

c--40--- n-Hexane
      data molec(40) /'n-c6h14'/, Wtprt(40) /86.18/, info(40)/0/
      data (c(40,j),j=1,5) /2.331,34.773,1.352,1.861,4.400/

c--41--- Methanol
      data molec(41) /'ch3oh'/, Wtprt(41) /32.04/, info(41)/1/
      data (c(41,j),j=1,5) /1.000,22.515,2.073,3.511,3.300/

c--42--- No Data (non-quenching species)
      data molec(42) /'no data'/, Wtprt(42) /1.00/, info(42)/2/
      data (c(42,j),j=1,5) /0.0,4*1.0/

c-----

```

END

SUBROUTINE qoh(minp, ispec, x, t, p, sigma, grate, iflag)

```

c*****
c      p      = pressure (atm)
c      t      = temperature (K)
c      Wt     = molecular weight for OH
c      Wtprt= molecular weight for collision partner
c      sigma= quenching cross section (Angstrom**2)
c      x      = mole fraction of collision partner
c      grate= quenching rate (1/s)
c      iflag= information flag
c              = 0 when there are no input errors; the cross section is
c                  base on experimental value(s).
c              = 1 when there are no input errors; the cross section is
c                  based solely on model results.
c              = 2 when the input temperature is outside the recommended range
c              = 3 when the cross section is based solely on the model results
c                  and the temperature is outside the recommended range
c              = 4 when no match was found for the specified species name
c      ispec= 0 search for the species given the name
c-----
c      Allocate extra storage space by using 'ndim=50'
c*****

      parameter (ndim=42)
      common /param/ nspec, molec, Wtprt, info, c, tmin, tmax, tref
      dimension Wtprt(ndim), info(ndim), c(ndim,5), molec(ndim)
      character molec*8, minp*8, mblnk*8

```

```

data Wt/17.01/, mblnk/'    '/

iflag = 0
sigma = 0.0
qrate = 0.0
c-----
c    When T is outside the recommended bounds, set the flag and continue
c-----
    if(t .lt. tmin .or. t .gt. tmax) iflag = 2

c-----
c    When the species name has been given, match it with the number
c-----
    if(ispec .eq. 0) then
        call match(minp, imch, iflag)
        if(iflag .eq. 4) then
            sigma = 0.0
            qrate = 0.0
            return
        endif
        if(info(imch) .eq. 1) iflag = iflag + 1

c-----
c    When the species identifier number has been given, proceed
c-----
        elseif(ispec .gt. 0 .and. ispec .le. nspec) then
            imch = ispec
            minp = molec(imch)
            if(info(imch) .eq. 1) iflag = iflag + 1
        else
            iflag = 4
            minp = mblnk
            sigma = 0.0
            qrate = 0.0
            return
        endif

c-----
c    Calculate the cross section (Angstrom**2) the collision rate (1/s);
c    When 'info' = 2, the modelled cross section is identically zero
c    When 'imch' = 11, the Garland and Crosley data are used (for N2)
c
c    this is commented out since we are using new fits from Phil Paul's
c    new OH paper
c-----
        if(info(imch) .eq. 2) then
            sigma = 0.0
            qrate = 0.0
            iflag = 1
            return
        elseif(imch .eq. 11) then                ! N2
            tt=t/1000.
            sigma = 0.15 + 0.58*exp(-tt) + 3.50*exp(-2.*tt)
            return
        else
            sigma = xsectn(imch,t)
        endif

        call cscon0(qrate, sigma, x, t, p, Wtptrt(imch), Wt)

c*****

```

```

c      End of routine goh
c*****

      return
      end

      SUBROUTINE match(minp, imch, iflag)
c*****
c      Match the input species name with one from the data base
c*****

      parameter (ndim=42)
      common /param/ nspec, molec, Wtprt, info, c, tmin, tmax, tref
      dimension Wtprt(ndim), info(ndim), c(ndim,5), molec(ndim)
      character molec*8, minp*8

      imch = 0
      do 200 i=1,nspec
         if(minp .eq. molec(i)) then
            imch = i
            return
         endif
      200 continue
c-----
c      No match was found, set iflag
c-----
      iflag = 4
      return
      end

c
c ***** CALC SIGMA *****
c
      FUNCTION xsectn(i,t)
      parameter (ndim=42)
      common /param/ nspec, molec, Wtprt, info, c, tmin, tmax, tref
      dimension Wtprt(ndim), info(ndim), c(ndim,5), molec(ndim)
      character molec*8

      a = 2.0/c(i,5)
      hc = c(i,4)*(tref/t)
      xsectn = c(i,1)*c(i,2)*((1.0+hc)*exp(-hc) +
&                c(i,3)*(hc**a) * gamma(2.0-a,hc) )

      return
      end

c %%%%%%%%%%% CALCULATE NO BOLTZMANN FRACTION %%%%%%%%%%%

      SUBROUTINE fb_no(t, ispin_no, jexct_no, fb)

c*****
c
c      Purpose:  To calculate the Boltzmann fraction given:
c                t      = temperature (K)
c                ispin_no = spin split level (i=1 or 2)
c                jexct_no = the excited quantum state
c      We have used the following approximation for the rotational
c      partition function:
c                qr = (exp(-0.5*g*A/t) + exp(0.5*g*A/t)) * t/(g*Bv)
c      By comparing this approximation to the "exact" value

```

```

c      (determined by summing the values, with each value equal to
c      (2j + 1) exp(-g*f/t).
c      To recover this exact value from this routine, simply sum
c      the f-values (to j-values of 100.5 to 200.5) for both spin
c      split states. The sum for ispin_no = 1 (i=1/2) begins at j=1/2,
c      while the that form ispin_no = 2 (i=3/2) begins at j=3/2.
c      We have determined that the approximation is reasonably accurate
c      from 250 K to 2500 K. Some of this inaccuracy is removed, since
c      we reference the individual measurements to the calibration
c      measurement.
c*****

      REAL jexct_no, jhat, mu
      data Bv/1.69619/,A/123.0372/,Dv/5.326E-6/,C/-1.1871E-3/,
&      we/1904.405/,wexe/14.1870/
c      data amu/1.6605e-24/,pi/3.1415927/,k/1.380622e-16/,g/1.438833/
      data g/1.438833/

c*****
c      Find the energy of the rotational state. The energy datum
c      (i.e., the energy above 0) equals
c      Evib(v=0)
c      where Evib is the energy of the v=0 state. Note that this
c      datum is arbitrary (only relative energies are relevant).
c*****

      mu = Dv/Bv
      jhat = (jexct_no + 0.5)**2.0
      if(ispin_no .eq. 1) then
        Yv = (A + C*(jexct_no - 0.5)**2)/Bv
        alpha = ((Yv - 2.0)/2.0)**2.0 +
&      (jhat - 1.0)*(1.0 + 2.0*mu*(2.0*jhat - Yv) +
&      (mu**2.0)*((2.0*jhat - 1.0)**2.0 - 1.0))
        fexct = Bv*(jhat - 1.0) - Dv*(jhat**2.0 - jhat + 1.0) -
&      Bv*(alpha**0.5)
      elseif(ispin_no .eq. 2) then
        Yv = (A - C*(jexct_no - 0.5)**2)/Bv
        alpha = ((Yv - 2.0)/2.0)**2.0 +
&      (jhat - 1.0)*(1.0 + 2.0*mu*(2.0*jhat - Yv) +
&      (mu**2.0)*((2.0*jhat - 1.0)**2.0 - 1.0))
        fexct = Bv*(jhat - 1.0) - Dv*(jhat**2.0 - jhat + 1.0) +
&      Bv*(alpha**0.5)
      endif

c*****
c      Calculate the rotational partition function
c*****

      Ae1 = (0.5*Bv - A)/2.0
      Ae2 = (A - 3.5*Bv)/2.0
      qr = (exp(-g*Ae1/t) + exp(-g*Ae2/t)) * t/(g*Bv)

c*****
c      Find the vibrational partition function:
c      sum to the 20th vibrational state
c*****

      qv = 0.0
      DO 100 i=1,20
        v = float(i - 1)
        Gv = we*(v + 0.5) - wexe*(v + 0.5)**2.0

```



```

&      iOH /3/,
&      iH  /4/
&      iH2O/5/,
&      iN2 /6/,
&      iCO2/7/,
&      iCO /8/

      zeta = 300.0/t

C*****
C      Calculate the rate of quenching for each species:
C      These cross sections were updated 5/17/94
C      O2
C*****

      sigma = 25.1
      call cscon0(qO2, sigma, x(iO2), t, p, 32.0, Wt)

C*****
C      H2O
C*****

      eta = 0.15*zeta + 2.95*(zeta**2.0)
      sigma = 28.2*( (1.0+eta)*exp(-eta) +
&                  3.39*(eta**b)*gamma(a,eta))
      call cscon0(qH2O, sigma, x(iH2O), t, p, 18.0, Wt)

C*****
C      N2
C*****

      if(t .le. 1800.0) then
        sigma = 0.88*exp(-4.8*zeta) + 3.1*exp(-16.0*zeta)
      else
        sigma = 0.88*exp(-4.9*zeta) + 48.0*exp(-32.0*zeta)
      endif
      call cscon0(qN2, sigma, x(iN2), t, p, 28.0, Wt)

C*****
C      O
C*****

      sigma = 32.0
      call cscon0(qO, sigma, x(iO), t, p, 16.0, Wt)

C*****
C      OH
C*****

      sigma = 85.0                ! was 134.0
      call cscon0(qOH, sigma, x(iOH), t, p, 17.0, Wt)

C*****
C      H
C*****

      sigma = 12.0
      call cscon0(qH, sigma, x(iH), t, p, 1.008, Wt)

C*****
C      CO2

```

```

C*****

      eta = 3.24*zeta + 0.18*(zeta**2.0)
      sigma = 54.2*( (1.0+eta)*exp(-eta) +
&      0.95*(eta**b)*gamma(a,eta))
      call cscon0(qCO2, sigma, x(iCO2), t, p, 44.0, Wt)

C*****
C      CO
C*****

      sigma = 5.9 + 5.3*exp(-7.0*zeta) + 22.1*exp(-14.0*zeta)
      call cscon0(qCO, sigma, x(iCO), t, p, 28.0, Wt)

C*****
C      Sum the quenching rates and add to the radiative decay rate
C      (note: H2, He, Ar, CH4 do not quench NO)
C*****

      qsum = qO2 + qH2O + qN2 + qO + qOH + qH + qCO2 + qCO + Afl

      return
      END

C $$$$$$$$$$$$ CALC GAMMA FUNCTIONS $$$$$$$$$$$$$$$$

C      Routines for computing the incomplete gamma function ...
C      See "Numerical Recipes: The Art of Scientific Computing" by
C      Press et al. for a more complete description of the calculation
C      of the incomplete gamma function
C*****

      FUNCTION gammp(a,x)
      if((x .lt. 0.0) .or. (a .le. 0.0)) pause
      if(x .lt. a+1.0) then
         call gser(gamser,a,x,gln)
         gammp = gamser
      else
         call gcf(gammcf,a,x,gln)
         gammp = gammcf
      endif
      return
      END

C*****
C      Compute the product of the gamma and incomplete gamma functions
C*****

      FUNCTION gamma(a,x)
      if(x .lt. a+1.0) then
         call gser(gamser,a,x,gln)
         gamma = exp(gln) * gamser
      else
         call gcf(gammcf,a,x,gln)
         gamma = exp(gln) * gammcf
      endif
      return
      END

```

```

C*****
C      Compute the incomplete gamma function ... for x < a+1
C      <<series representation>>
C*****

```

```

      SUBROUTINE gser(gamser,a,x,gln)
      common /error/ itmax, eps
      gln = gammln(a)
      if(x .le. 0.0) then
        if(x .lt. 0.0) pause
        gamser = 0.0
        return
      endif
      ap = a
      sum = 1.0/a
      del = sum
      do 100 n=1, itmax
        ap = ap + 1.0
        del = del*x/ap
        sum = sum + del
        if(abs(del) .lt. abs(sum)*eps) then
          gamser = sum*exp(-x+a*log(x) - gln)
          return
        endif
100    continue
      pause 'a too large, itmax too small'
      return
      END

```

```

C*****
C      Compute the incomplete gamma function ... for x >= a+1
C      <<continued fraction representation>>
C*****

```

```

      SUBROUTINE gcf(gammcf,a,x,gln)
      common /error/ itmax, eps
      gln = gammln(a)
      gold = 0.0
      a0 = 1.0
      a1 = x
      b0 = 0.0
      b1 = 1.0
      fac = 1.0
      do 100 n=1, itmax
        an = float(n)
        ana = an - a
        a0 = (a1 + a0*ana)*fac
        b0 = (b1 + b0*ana)*fac
        anf = an*fac
        a1 = x*a0 + anf*a1
        b1 = x*b0 + anf*b1
        fac = 1.0/a1
        g = b1*fac
        if(abs((g-gold)/g) .lt. eps) then
          gammcf = 1.0 - g*exp(-x + a*log(x) - gln)
          return
        endif
        gold = g
100    continue
      pause 'a too large, itmax too small'

```



```

        return
        END

C*****
C      Compute the gamma function ... gammln = ln(gamma)
C*****

      FUNCTION gammln(xx)
      real*8 cof(6), stp, half, one, fpf, x, tmp, ser
      data cof/76.18009173D0, -86.50532033D0, 24.01409822D0,
&          -1.231739516D0, 0.120858003D-2, -0.536382D-5/
      data stp/2.50662827465D0/
      data half, one, fpf/0.5D0, 1.0D0, 5.5D0/
      x = xx - one
      tmp = x + fpf
      tmp = (x + half)*dlog(tmp) - tmp
      ser = one
      do 100 j=1,6
          x = x + one
          ser = ser + cof(j)/x
100    continue
      gammln = tmp + log(stp*ser)
      return
      END

C*****
C      End of incomplete gamma function routines
C*****

      SUBROUTINE cscon0(z, sigma, x, t, p, Wt1, Wt2)

C*****
C      The subroutine converts collision cross sections (cm**2) to
C      collision rates (sec**-1).
C
C      Subroutine parameters:
C      z      is the number of quenching collisions per unit time
C              that a particular molecule undergoes
C
C              z = rho * sigma * vbar
C
C      rho    is the number density (molecules/cm**3) of the collision
C              partner and is calculated from the ideal gas law
C      sigma  is the collision cross section (A**2)
C      vbar   is the relative velocity (cm/sec) between the two molecules,
C
C              vbar = (8*k*t/pi*mu)**.5
C
C      mu     is the reduced mass (gm) of the two colliding species,
C              Wt1 and Wt2 (atomic units)
C
C              mu = amu * (Wt1 * Wt2)/(Wt1 + Wt2)
C
C      amu    atomic mass units, the number of grams per atomic unit
C      k      is the Boltzmann constant (erg/molecule-kelvins)
C      t      is the temperature (kelvins) of the gas
C      p      is the pressure (atm)
C      x      is the mole fraction of the collision partner
C*****

      real k, mu

```

```

data k/1.3806e-16/,pi/3.14159/,amu/1.6605e-24/,rhat/1.2187e-2/

C*****
C  Calculate the reduced mass
C*****

mu = amu * (Wt1 * Wt2)/(Wt1 + Wt2)

C*****
C  Calculate the collision rate, z
C  (convert the cross section from square Angstroms to square cm)
C*****

rho = x * rhat * p/(t * amu)
vbar = ((8.0*k*t)/(pi*mu))**0.5
z = rho * (sigma * 1.0e-16) * vbar

C*****
C  End of subroutine CSCON
C*****

return
END

C
C $$$$$$$$$$ calculate the laser-absorption overlap integral $$$$$$$$$$
C

SUBROUTINE overlap(t, freq, dtune, dlas, cp)

C*****
C  This routine calculates the convolution of the laser profile
C  with the absorption profile. This convolution is performed
C  efficiently by realizing that the convolution of a Gaussian
C  (laser) profile with the Voigt (absorption) profile is also a
C  Voigt profile. As written, the laser linewidth is the FWHM
C  value. The collisional linewidth is determined from the
C  relation determined by Chang et al. for N2. The collisional
C  shift has not been included.
C
C  Parameters:
C  t      = gas temperature (K)
C  freq   = transition frequency (cm**-1)
C  dtune  = laser detuning from line center (cm**-1)
C  dlas   = Gaussian laser linewidth (FWHM, cm**-1)
C  ddop   = Doppler linewidth (cm**-1)
C  dcol   = collisional linewidth (cm**-1)
C  alpha  = nondimensional laser linewidth
C  a      = nondimensional broadening parameter
C  del    = nondimensional laser detuning
C  anorm  = nondimensional width from convolution of Doppler and
C          laser lines
C  cp     = convolution of laser and Voigt (transition) lines
C
C  Note: if laser cannot be approximated by a simple Gaussian
C        function, use multiple Gaussian functions.
C*****

ddop = 1.3075e-7 * freq * (t)**0.5
dcol = 0.585 * (295.0/t)**0.75
a     = 0.83255 * (dcol/ddop)
del   = 1.66511 * (dtune/ddop)

```

```

alpha = dlas/ddop
anorm = sqrt(1.0 + alpha**2)
cp = (alpha/anorm) * v(del/anorm, a/anorm)

return
end

function v(xin,y)
C*****
c    This the Voigt function, as approximated by Hummer.
c    Comparisons with the exact solution (by integration) confirm
c    that the error of this approximation is less than 2 ppm
C*****
    implicit real (a-h,o-z)
    dimension t(6), c(6), s(6)
    data (t(j),j=1,6) /0.314240376e00,0.947788391e00,0.159768264e01,
&      0.227950708e01,0.302063703e01,0.388972490e01/
    data (c(j),j=1,6) /0.101172805e01,-0.75197147e00,0.12557727e-01,
&      0.100220082e-01,-0.242068135e-03,0.500848061e-06/
    data (s(j),j=1,6) /0.13932370e01,0.231152406e00,-0.155351466e00,
&      0.621836624e-02,0.919082986e-04,-0.627525958e-06/

    x = abs(xin)
    vsum = 0.0e00
    y1 = y + 1.5e00
    y2 = y1*y1
    if((y .gt. 0.85) .or. (x .lt. (18.1*y + 1.65))) then
        do 40 i=1,6
            r = x - t(i)
            d = 1.0e00/(r*r + y2)
            d1 = y1 * d
            d2 = r * d
            r = x + t(i)
            d = 1.0e00/(r*r + y2)
            d3 = y1 * d
            d4 = r * d
            vsum = vsum + c(i)*(d1+d3) - s(i)*(d2-d4)
40      continue
    else
        if(x .lt. 12.0) vsum = exp(-x*x)
        y3 = y + 3.0e00
        do 80 i=1,6
            r = x - t(i)
            r2 = r*r
            d = 1.0e00/(r2 + y2)
            d1 = y1*d
            d2 = r*d
            vsum = vsum + y*(c(i)*(r*d2 - 1.5*d1) + s(i)*y3*d2)/(r2+2.25)
            r = x + t(i)
            r2 = r*r
            d = 1.0e00/(r2 + y2)
            d3 = y1*d
            d4 = r*d
            vsum = vsum + y*(c(i)*(r*d4 - 1.5*d3) - s(i)*y3*d4)/(r2+2.25)
80      continue
    endif
    v = vsum
    RETURN
    END

```

Typical Output file of RN01.FOR

; data for input file vbflzt-v.dat

;L, T, N2, O2, H2, H2O, CO2, COx10, CH4, OHx100,NOx10000

210.0	1375.5	7.669E-01	8.560E-02	0.000E+00	9.730E-02	5.020E-02	0.000E+00	0.000E+00	1.611E-02	4.008E-01
200.0	1493.5	7.639E-01	6.590E-02	0.000E+00	1.100E-01	6.010E-02	0.000E+00	0.000E+00	2.830E-02	4.797E-01
190.0	1555.1	7.595E-01	5.830E-02	0.000E+00	1.179E-01	6.430E-02	0.000E+00	0.000E+00	3.023E-02	5.267E-01
180.0	1610.3	7.576E-01	4.930E-02	0.000E+00	1.233E-01	6.980E-02	0.000E+00	0.000E+00	3.975E-02	5.615E-01
170.0	1664.0	7.580E-01	3.970E-02	0.000E+00	1.291E-01	7.310E-02	0.000E+00	0.000E+00	4.780E-02	5.924E-01
160.0	1726.5	7.527E-01	3.330E-02	0.000E+00	1.364E-01	7.760E-02	0.000E+00	0.000E+00	6.178E-02	6.380E-01
150.0	1771.7	7.500E-01	2.730E-02	0.000E+00	1.406E-01	8.210E-02	0.000E+00	0.000E+00	8.615E-02	6.678E-01
140.0	1811.4	7.481E-01	2.210E-02	0.000E+00	1.443E-01	8.540E-02	0.000E+00	0.000E+00	1.132E-01	6.943E-01
130.0	1872.3	7.427E-01	1.750E-02	0.000E+00	1.505E-01	8.930E-02	0.000E+00	0.000E+00	1.508E-01	7.402E-01
120.0	1926.8	7.405E-01	8.900E-03	0.000E+00	1.556E-01	9.500E-02	0.000E+00	0.000E+00	2.026E-01	7.671E-01
110.0	1972.3	7.417E-01	0.000E+00	0.000E+00	1.603E-01	9.800E-02	0.000E+00	0.000E+00	2.359E-01	7.856E-01
105.0	1976.0	7.351E-01	0.000E+00	4.400E-03	1.596E-01	9.690E-02	0.000E+00	0.000E+00	2.449E-01	7.812E-01
100.0	1989.8	7.338E-01	0.000E+00	5.100E-03	1.624E-01	9.870E-02	0.000E+00	0.000E+00	2.510E-01	7.863E-01
95.0	2006.3	7.301E-01	0.000E+00	5.400E-03	1.621E-01	9.700E-02	5.400E-02	0.000E+00	2.417E-01	7.778E-01
90.0	2003.1	7.208E-01	0.000E+00	7.500E-03	1.633E-01	9.500E-02	1.340E-01	0.000E+00	2.034E-01	7.287E-01
85.0	2019.6	7.216E-01	0.000E+00	7.600E-03	1.633E-01	9.430E-02	1.330E-01	0.000E+00	1.867E-01	7.383E-01
80.0	2018.6	7.156E-01	0.000E+00	9.100E-03	1.644E-01	9.080E-02	2.010E-01	0.000E+00	1.530E-01	7.179E-01
75.0	2013.1	7.118E-01	0.000E+00	1.050E-02	1.643E-01	8.770E-02	2.570E-01	0.000E+00	1.310E-01	6.927E-01
70.0	2014.5	7.071E-01	0.000E+00	1.250E-02	1.650E-01	8.310E-02	3.220E-01	0.000E+00	1.046E-01	6.656E-01
65.0	2021.7	7.013E-01	0.000E+00	1.530E-02	1.664E-01	7.920E-02	3.790E-01	0.000E+00	8.023E-02	6.527E-01
60.0	2020.0	6.943E-01	0.000E+00	1.910E-02	1.672E-01	7.420E-02	4.510E-01	0.000E+00	7.057E-02	6.248E-01
55.0	2023.2	6.807E-01	0.000E+00	2.670E-02	1.679E-01	6.480E-02	5.990E-01	0.000E+00	5.039E-02	5.641E-01
50.0	2037.4	6.711E-01	0.000E+00	3.090E-02	1.723E-01	6.040E-02	6.530E-01	0.000E+00	4.926E-02	5.603E-01
45.0	2050.1	6.571E-01	0.000E+00	4.160E-02	1.766E-01	5.140E-02	7.330E-01	0.000E+00	6.387E-02	4.969E-01
40.0	1660.7	6.641E-01	4.680E-02	3.710E-02	1.232E-01	3.220E-02	6.150E-01	3.510E-02	8.366E-02	2.379E-01
38.0	968.1	6.530E-01	1.230E-01	2.910E-02	6.710E-02	8.600E-03	3.610E-01	8.300E-02	6.980E-02	3.620E-02
37.0	566.2	6.582E-01	1.645E-01	1.940E-02	3.350E-02	0.000E+00	1.140E-01	1.130E-01	5.622E-02	1.029E-02
36.0	344.9	6.674E-01	1.897E-01	1.050E-02	6.200E-03	0.000E+00	0.000E+00	1.262E-01	0.000E+00	1.553E-03
35.0	328.9	6.725E-01	1.922E-01	8.800E-03	0.000E+00	0.000E+00	0.000E+00	1.265E-01	0.000E+00	1.588E-03

Appendix F

High-Resolution Oxygen Absorption Spectrum

Obtained Using an External-Cavity Continuously Tunable Diode Laser

Abstract: We have measured the electronic absorption spectrum of the oxygen (O_2) A-band:

$b^1\Sigma_g^+(v' = 0) \leftarrow X^3\Sigma_g^-(v'' = 0)$, near 760 nm in room air using a newly available external-cavity diode laser. The external-cavity diode laser permitted a continuous, single-mode scan of the P-branch of ambient oxygen using $2f$ modulation spectroscopy. The external-cavity diode laser opens up many applications limited in the past by the non-continuous tunability of standard monolithic Fabry-Perot (FP) cavity laser designs. Specifically, absorption transitions which coincide with the gain bandwidth of any available diode laser (635 nm to 1550 nm) may now be accessed without the problems and limitations imposed by mode hops inherent in the standard FP cavity designs.

Diode lasers are attractive sources of tunable light for many spectroscopic applications due to their small size, solid-state ruggedness and reliability, and cost-effectiveness. However, their use in spectroscopic applications has been plagued by the discontinuous jumps, known as mode hops, in the emission wavelength during tuning. Mode hops seriously limit the performance of diode lasers as a technique for spectroscopic gas analysis -- especially at higher pressures where collisional line-broadening effects require a wide range of continuous tunability.

Monolithic Fabry-Perot (FP) cavity diode lasers are typically tuned by modulating the injection current. The emission wavelength of a FP cavity laser is tuned via the temperature dependence of the index of refraction of the semiconductor material which changes through ohmic heating as the injection current is varied. Although monolithic FP cavity diode lasers are prone to mode-hopping, they are favored by laser manufacturers for their simplicity since they are produced by cleaving the semiconductor crystal. The cleaving process produces an alignment free laser cavity formed by the two cleaved facets of the semiconductor crystal. Mode hopping is caused by the competition between the several FP cavity modes within the laser gain bandwidth. As the optical cavity length is varied during tuning, one mode can suddenly have more power than the original mode, resulting in the discontinuous jump in wavelength. In addition, mode hops also create inaccessible gaps in the tuning curve which are typically several cm^{-1} 's wide.

Mode-hopping can be eliminated by using the diode laser semiconductor material as a gain medium in an external-cavity configuration. This is accomplished by decoupling the FP modes of the semiconductor crystal from the laser oscillator cavity using an anti-reflection coating on the output

facet. This new external-cavity oscillator geometry has been successfully demonstrated in 1991 by Harvey and Myatt¹. Although the Harvey-Myatt geometry is similar to the one proposed by Liu and Littman² for a pulsed dye laser, it differs in that an intracavity lens is used to collimate the beam, the gain medium is a semiconductor waveguide, and the laser is CW. The Harvey-Myatt geometry allows continuous tuning of the wavelength over a broad range by simultaneously varying the feedback wavelength and the cavity length. The result is a simple, passive, and continuously tunable, single-mode laser design.

As a simple experimental demonstration of the broad tunability of the Harvey-Myatt external cavity configuration, we measure the weak spin-forbidden electronic absorption spectrum of the oxygen A-band: $b^1\Sigma_g^+(v' = 0) \leftarrow X^3\Sigma_g^-(v'' = 0)$, near 760 nm. The detection of oxygen in the A-band using diode laser absorption was demonstrated by Bruce and Cassidy³ and also by Phillippe and Hanson⁴ using a standard FP diode laser to measure the absorption of several transitions. As shown by Phillippe and Hanson⁴, monolithic FP diode lasers can typically access at most, 2 adjacent absorption transitions (separated by several cm^{-1} 's) in a single continuous scan before mode hopping. The broad and continuous tunability of external-cavity diode lasers allows the measurement of many absorption transitions in a single scan, and allows the determination of the Boltzmann vibration-rotation temperature through the ratios of linestrengths as demonstrated for the CO molecule at 4.8 μm by Nguyen *et al.*⁵ We obtain the entire P-rotational branch (approximately 30 lines at ambient temperatures) in a single continuous scan from 762 to 770 nm (230 cm^{-1} 's wide).

Figure 1 shows the schematic of the experimental arrangement used to obtain the oxygen absorption spectrum. In order to shift the peak of the 780 nm (at 25 °C) semiconductor gain curve towards 760 nm, the external-cavity laser (New Focus, Model 6102) was operated at a constant temperature of 14 °C, and constant injection current of 90 mA, with a nominal output power of 6.5 mW. A beamsplitter directs a fraction of the laser output into a scanning Michelson interferometer (Burleigh Wavemeter) for wavelength determination. Mirrors direct the transmitted beam into a 22 m pathlength multipass optical absorption cell (Infrared Analysis, Model 5-22-PA-Ag). A 15 cm focal length mirror focuses the laser light emerging from the White cell into a Si photodiode-preamplifier (New Focus, Model 2001). A lock-in amplifier (Stanford Research Systems, Model SRS 530) set for

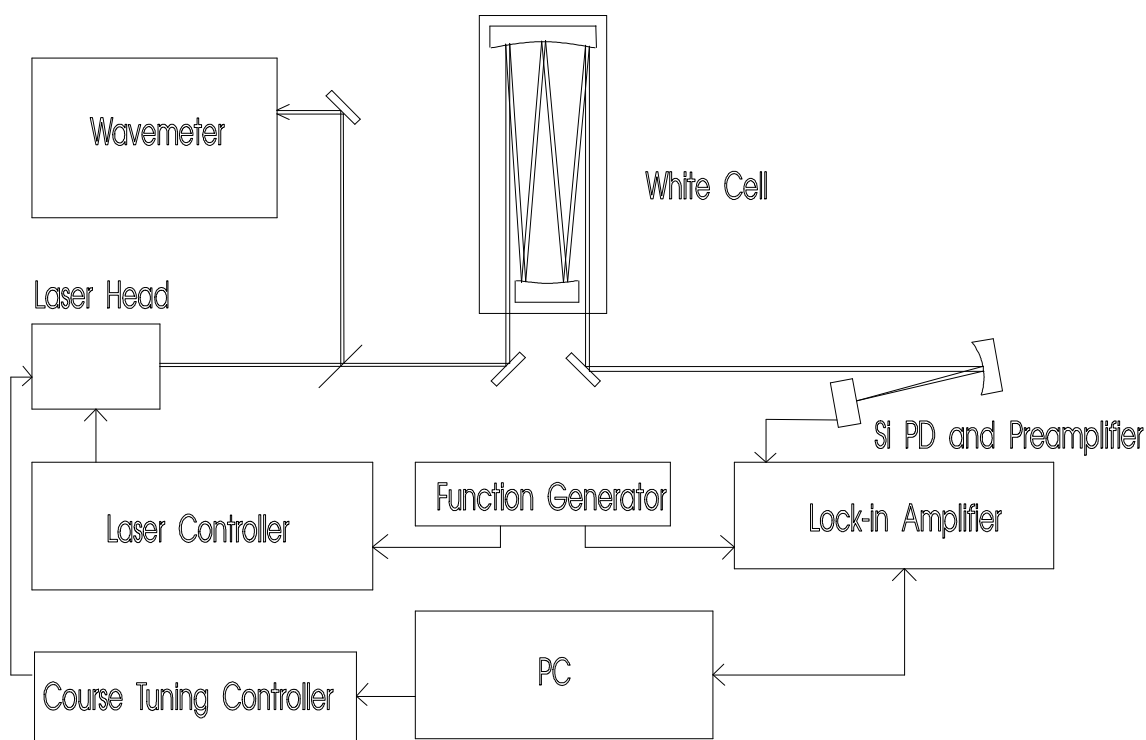


Figure 1: Schematic of optical and instrumentation set up used to obtain the oxygen absorption spectrum.

$2f$ detection processes the signal from the photodiode-preamplifier. Detection of the transmitted signal at $2f$ was chosen to increase the detection sensitivity as suggested by Silver⁶. A piezoelectric stepper motor (New Focus Picomotor) scans the wavelength of the laser via rotation of the feedback mirror in the laser cavity. A PC controls the stepper motor and interfaces the lock-in amplifier for data acquisition. As the laser wavelength is continuously scanned, a sinusoidal modulation is imposed on the laser wavelength (through a secondary piezoelectric actuator) for modulation spectroscopy.

A sine-function generator modulates the laser wavelength through the fine-frequency external input of the laser controller. The function generator is set to an amplitude of 930 mV (peak-peak) with a frequency $f = 108$ Hz -- the maximum laser modulation frequency (200 Hz) is limited by the inertia of the tuning mirror assembly since the tuning is effected by a physical motion of the mirror. Monolithic FP diode lasers, however, can be routinely tuned at up to MHz frequencies since there is no physical motion involved in the fine tuning process. As suggested by Arndt⁷, and by Reid and Labrie⁸, optimum $2f$ signals (at 216 Hz) are generated when modulation widths are of the order of the O₂ absorption width (approx. 0.05 cm^{-1} -- largely due to collisional broadening at 300 K and 1 atm).

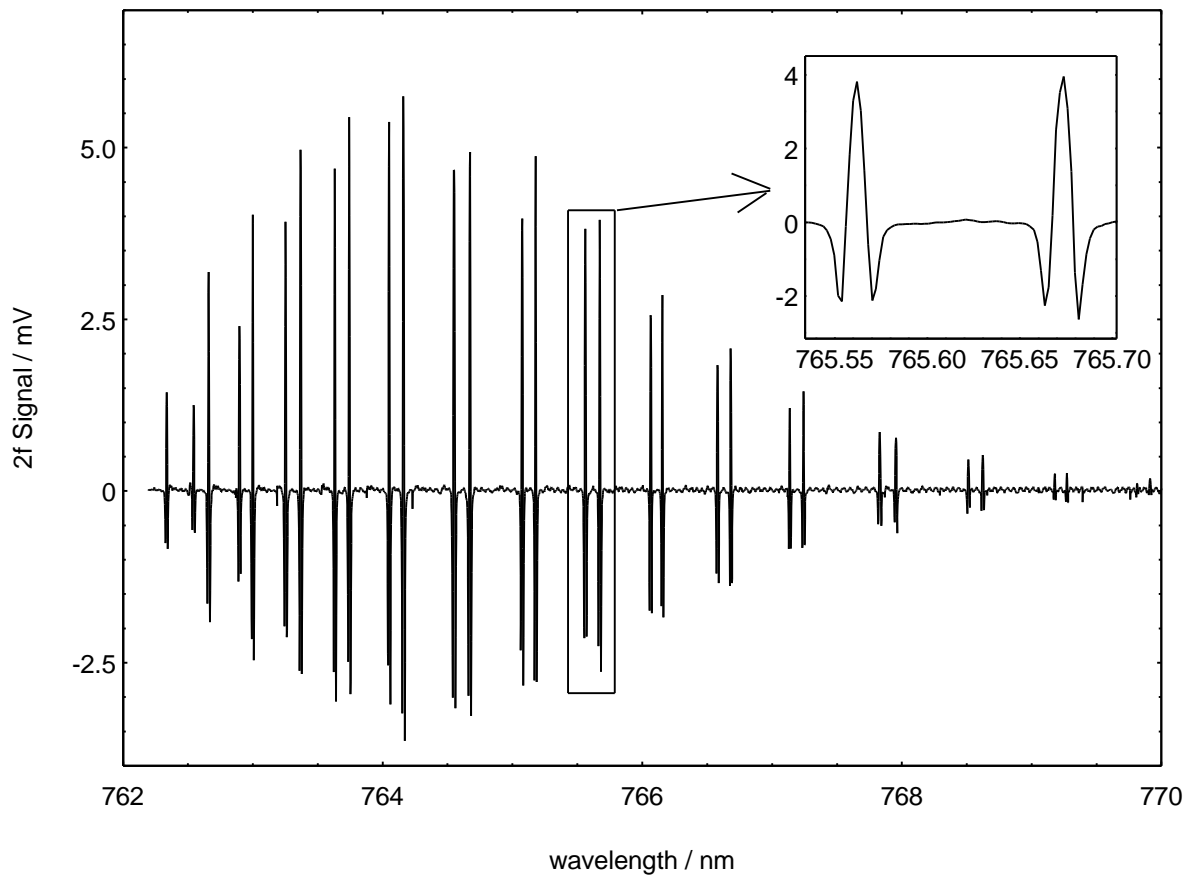


Figure 2: The $2f$ absorption spectrum of the oxygen A-band in ambient room air obtained under the following conditions: $T = 300$ K, $P = 1$ atm, $L = 22$ m.

Figure 2 shows the $2f$ absorption spectrum of oxygen in ambient air. The spectrum spans from 762 to 770 nm showing the broad tunability of the laser. The inset graph in Fig. 1 shows the detail of the spectrum when wavelength axis is expanded. Setting the time constant of the lock-in amplifier at 1 second provides a sufficient amount of signal averaging, resulting in the high S/N ratio shown. The low-noise, high resolution spectrum (8800 points) required 7.3 minutes to collect due to the relatively slow $f=108$ Hz modulation frequency. This spectrum was obtained without optimizing the optics to reduce the interference effects resulting from the generation of etalon fringes in the multipass optical cell. Techniques such as applying a secondary out-of-phase modulation as suggested by Sirota *et al.*⁹ or applying a physical dither to one of the mirrors of the optical cell as

suggested by Silver⁶, can also be used to increase the detection sensitivity. The transitions were compared with those available through the HITRAN database¹⁰ and agreed well within the uncertainty of the wavemeter ($\pm 0.005 \text{ cm}^{-1}$).

The recent commercial availability of external-cavity diode lasers has opened up many possibilities in the field of spectroscopic chemical analysis and measurement. The main advantage of the Harvey-Myatt external-cavity design is the elimination of the mode-hopping problems inherent in all standard FP diode laser designs. Thus, the available laser wavelengths are no longer limited by gaps in the tuning range due to mode hops, and a continuous scan over the entire semiconductor gain bandwidth is now possible. As an example of the ease of use and simplicity of these new external-cavity lasers, we have obtained the absorption spectrum of the entire P-branch of the oxygen A-band in ambient air using a commercially available external-cavity diode laser, a multipass absorption cell, a Si photodiode detector, and a standard lock-in amplifier.

References:

1. K. C. Harvey, and C. J. Myatt, *Optics Letters*, Vol. 16, No. 12, pp. 910-912, 1991.
2. K. Liu, and M. G. Littman, *Optics Letters*, Vol. 6, No. 3, pp. 117-118, 1981.
3. D. M. Bruce, and D. T. Cassidy, *Applied Optics*, Vol. 29, No. 9, pp. 1327-1332, 1990.
4. L. C. Phillipe, and R. K. Hanson, *30th Aerospace Sciences Meeting and Exhibit*, AIAA paper No. 92-0139, 1992.
5. Q. V. Nguyen, R. W. Dibble, D. Hofmann, and S. Kampmann, *Ber. Bunsenges. Phys. Chem.*, Vol. 7, No. 12, 1993.
6. J. A. Silver, *Applied Optics*, Vol. 31, No. 6, pp. 707-717, 1992.

7. R. Arndt, *Applied Physics*, Vol. 36, No. 8, pp.2522-2524, 1965.
8. J. Reid, and D. Labrie, *Applied Physics*, Vol. B26, pp. 203-210, 1981.
9. J. M. Sirota, D. C. Reuter, and M. J. Mumma, *Applied Optics*, Vol. 32, No.12, pp. 2117-2121, 1993.
10. L. S. Rothman, *et al.*, The HITRAN Data Base: 1986 Edition, *Applied Optics*, Vol. 26, 1987.